3D Live-cell Imaging of In Vitro Neuronal Microtissues - Using Spectral Image Scanning Microscopy

Sara Rahmati

THÈSE PRÉSENTÉE

POUR OBTENIR LE GRADE DE

DOCTEUR DE

L'UNIVERSITÉ DE BORDEAUX

ÉCOLE DOCTORALE DES SCIENCES DE LA VIE ET DE LA SANTÉ

SPÉCIALITÉ: BIOIMAGERIE

Par **Sarah RAHMATI**

3D Live-cell Imaging of *In Vitro* Neuronal Microtissues Using Spectral Image Scanning Microscopy

Sous la direction de: Dr. Vincent STUDER

Soutenue le 18 mars 2022

Membres du jury

Dr. LEVEQUE-FORT, Sandrine	Directrice de recherche, CNRS, Université Paris-Saclay	Rapportrice
Pr. HAUTEFEUILLE, Mathieu	Professeur, Université Sorbonne	Rapporteur
Dr. STUDER, Vincent	Directeur de recherche, CNRS, Université de Bordeaux	Directeur de thèse
Dr. NASSOY, Pierre	Directeur de recherche, CNRS, Université de Bordeaux	Président
Pr. DUPIN, ISABELLE	Professeure, CHU de Bordeaux	Membre invité

Institut Interdisciplinaire de NeuroScience (IINS)

CNRS UMR 5297 Université de Bordeaux

Centre Broca Nouvelle-Aquitaine

146 Rue Léo Saignat

33076 Bordeaux (France)

Abstract

To better understand complex brain interconnections, 3-dimensional cell models have proven to be more physiologically relevant than 2-dimensional culture plates. Specifically, to mimic *in vivo*-like synaptic connections and activities, a recently developed experimental model known as spheroids - 3D cell aggregations - have been used to study neuronal networks[1] [2]. However, existing models are large (>100 μm) and not amenable for live-cell 3D imaging at the single-cell resolution due to the diffraction and penetration limit of light. Here we combined a 3D *in vitro* model to investigate synaptic contacts with an imaging technique that allows monitoring dynamic events at synaptic level with high spatio-temporal and spectral resolution. In this work, neuronal spheroids are formed in hydrogel templates with standardized sizes and shapes. These hydrogel-based templates are fabricated by a patterned UV projector system, a macromonomer, and a photoinitiator through a radical polymerization process. The result is a substrate with stiffness close to physiological conditions that enable the self-aggregation of neurons. Spheroids formed in these templates showed similar organization and biochemical characteristics to those previously reported. Neurons in the spheroids were selectively and sparsely transfected with fluorescent reporters. To perform live-cell 3D imaging of the model, we developed a novel spectral image scanning microscopy technique with optical sectioning and spectral resolution capabilities. A digital micro-mirror device generates point illuminations which allow optical sectioning using a discrimination algorithm. To generate multicolor images, a prism is employed to disperse emission light along its axis and collected by a fast CMOS camera. By colocalizing, summing, and spatial filtering, spectral image scanning generates an image with a spatial resolution of 350 laterally nm and 450 nm axially. Extended time-lapse imaging (20 hours) of neurons transfected with GFP and tdtomato highlights the ability of the Spectral ISM for 3D live-cell imaging. The combination of a DMD-based Spectral ISM with hydrogel templates shows great potential for further investigations of human brain cells at the level of synapses in a 3D environment using induced pluripotent stem cells.

Keywords:

neuronal spheroids, 3D microscopy, Live-cell imaging, hydrogel templates, synaptic connectivity, iPSC, multicolor imaging, optical sectioning

Résumé

Les modèles cellulaires tridimensionnels se sont avérés plus pertinents sur le plan physiologique que les plaques de culture bidimensionnelles. Plus précisément, pour imiter les connexions et les activités synaptiques de type in vivo, un modèle expérimental récemment développé, connu sous le nom de sphéroïdes - des agrégations de cellules en 3D - a été utilisé pour étudier les réseaux neuronaux[1] [2]. Cependant, les modèles existants sont de grande taille (>100 μm) et ne se prêtent pas à l'imagerie 3D de cellules vivantes à la résolution d'une cellule unique en raison de la limite de diffraction et de pénétration de la lumière.Nous avons ici combiné un modèle 3D *in vitro* pour étudier les contacts synaptiques avec une technique d'imagerie qui permet de suivre les événements dynamiques au niveau synaptique avec une haute résolution spatio-temporelle et spectrale. Dans ce travail, les sphéroïdes neuronaux sont formés dans des modèles d'hydrogel de taille et de forme standardisées. Ces modèles à base d'hydrogel sont fabriqués à l'aide d'un système de projecteur UV à motifs, d'un macromonomère et d'un photoinitiateur par un processus de polymérisation radicalaire. Le résultat est un substrat dont la rigidité est proche des conditions physiologiques et qui permet l'auto-agrégation des neurones. Les sphéroïdes formés dans ces gabarits ont montré une organisation et des caractéristiques biochimiques similaires à celles rapportées précédemment. Les neurones dans les sphéroïdes ont été transfectés de manière sélective et éparse avec des rapporteurs fluorescents. Pour réaliser l'imagerie 3D en direct du modèle, nous avons mis au point une nouvelle technique de microscopie à balayage d'images spectrales avec des capacités de sectionnement optique et de résolution spectrale. Un dispositif numérique à micro-miroirs génère des éclairages ponctuels qui permettent de réaliser des coupes optiques à l'aide d'un algorithme de discrimination. Pour générer des images multicolores, un prisme est utilisé pour disperser la lumière d'émission le long de son axe et collectée par une caméra CMOS rapide. Par colocalisation, sommation et filtrage spatial, le balayage spectral de l'image génère une image avec une résolution spatiale de 350 nm latéralement et 450 nm axialement. L'imagerie prolongée (20 heures) de neurones transfectés avec la GFP et le tdtomato met en évidence la capacité de l'ISM spectral pour l'imagerie 3D de cellules vivantes. La combinaison d'un ISM Spectral basé sur la DMD et de modèles d'hydrogel présente un grand potentiel pour des études plus poussées des cellules du cerveau humain au niveau des synapses dans un environnement 3D utilisant des cellules souches pluripotentes induites.

Keywords:
sphéroïdes neuronaux, microscopie 3D, imagerie des cellules vivantes, modèles d'hydrogel, connectivité synaptique, imagerie multicolore, sectionnement optique

Contents

List of Figures

List of Acronyms

Chapter 1

Introduction

The human brain is by far the most complicated structure that we have yet discovered in the universe. Every movement, thought, and memory we have can be examined and studied at the level of individual neurons and may help us to understand these questions: How does our brain develop throughout our life? How does each brain cell communicate, and how is this communication modified through learning and memory formation? And finally, how does this communication undergo changes in diseases? We have not entirely answered these questions but have learned a great deal through advanced electrophysiology, microscopy, and biochemistry. In the last two decades, one of the main interests of neuroscientists has been to answer the question " How do each brain cell communicate and what are the underlying mechanisms?" The nervous system functions by transmitting signals throughout brain regions. Within a mature nervous system, cells are interconnected in highly complex Three-Dimension (3D) networks. Every connection in this entangled and dynamic system can be associated with learning and memory formation. Understanding this interconnectivity and how it tunes throughout life may provide deep insights into the pathophysiology of neuronal functions and disorders. While great efforts have been devoted toward the morphofunctional study of nervous systems, understanding of mechanisms underlying learning and memory storage remains limited. Further progress, is restricted, amongst others, by two main limitations: 1) a neuronal model that first, mimics tissue-like behavior, structure, and microenvironments, and is amenable for microscopy imaging with a high spatio-temporal resolution that captures all the activities at the synaptic level. 2) A microscopy tool

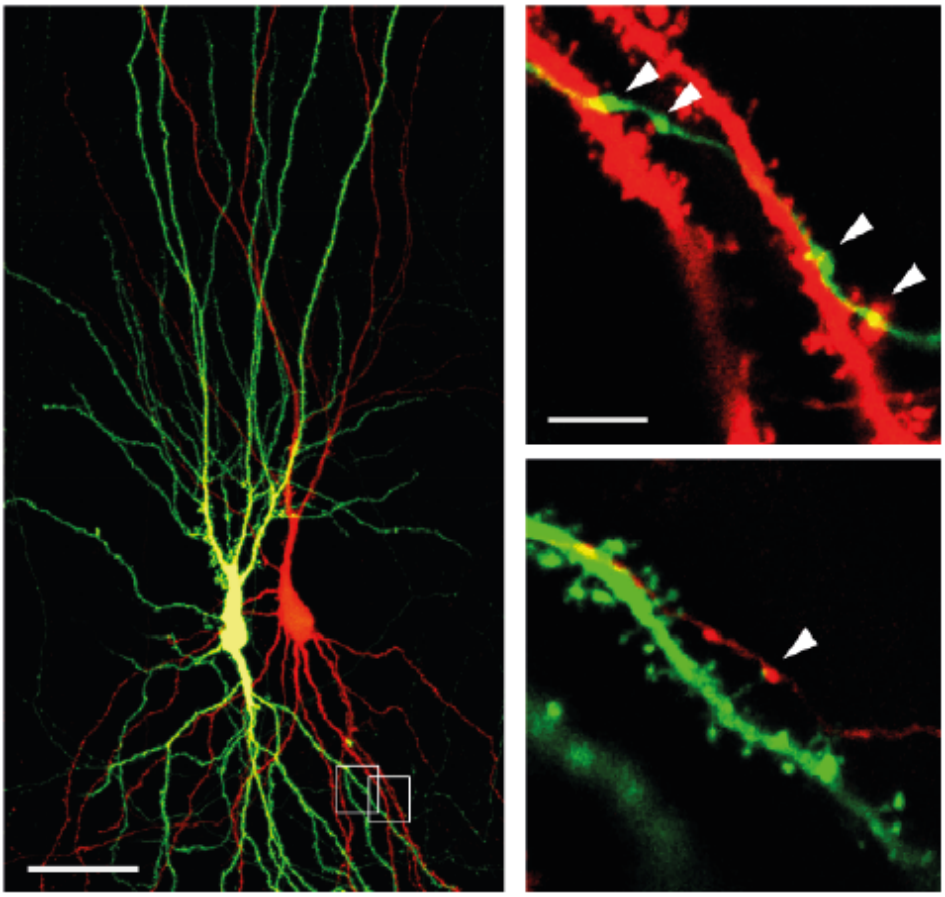

Figure 1.1: Interconnections of two neurons in CA3 region of rat organotypic hippocampal slice cultures *ex vivo* fixed after expression. Neurons transfected with GFP and tdtomato using single-cell electroporation (SCE) technique by selectively inserting the DNA plasmid into neurons in the tissue with the help of micropipettes. Images are taken by a confocal microscope adapted From [1].

that allows live-cell imaging of neuronal structures in 3D with multiple fluorophores to trace individual neurons and their contacts with distinctive colors. **Figure 1.1** is an image of two neurons transfected by single-cell electroporation (SCE) technique which allows sparse labeling of distinct neurons in a 3D environment.

SCE used in organotypic slices allows the investigation of individual neurons instead of seeing a bulk of fluorescent tissue that would arise with global transfection like that seen with viral transfection. This image illustrates one of the closest

ex vivo models that mimic the *in vivo* environment, in order to study synaptic contacts in-depth and at high resolution. However, the limitations of this remain challenging. There is no model that easily combines with an established imaging technique that allows *in vivo*-like neuronal observation with the highest possible resolution to resolve synaptic contacts and their alterations over time ranging with a temporal resolution of a few minutes to capture 5D (x,y,z, time, color) image data over several hours or days. My PhD thesis aimed to develop an *in vitro* neuronal model and an imaging technique that increases the capability of current technologies to perform 3D multicolor live imaging of neuronal contacts growing in physiological environments.

Various models have been introduced and used to understand neuronal communication including, animal models (*in vivo*), tissue culture (*ex vivo*), Two-Dimension (2D), and more recently 3D culture (*in vitro*). While *in vivo* and *ex vivo* are widely used, their high physiological relevance comes at the cost of technical challenges in observation and genetic manipulation. In addition, they are primarily Murine-based and do not fully reflect human physiology. 2D monolayer cultures, on the other hand, are commonly used across diverse cell types because they are easy to use, cost-effective, and robust. Moreover, they are easy to observe and measure under the microscope. However, 2D culture models are generally inadequate in mimicking specific physiological features due to insufficient cell-cell and cell-Extracellular Matrix (ECM) interactions. To bridge the gap of having a more physiologically relevant system and also amenable for microscopy imaging (**Figure 1.2**), cell-based 3D *in vitro* models have been extensively explored in the recent past. These findings suggest that compared to 2D cultures, 3D cultures give more complex environments and tend to be more informative and predictive of native-tissue behaviors [2] [3]. They also have the capacity to tune and become compatible with optical imaging techniques for real-time observation. Moreover, human induced Pluripotent Stem Cells (iPSC)-derived 3D cultures not only can broaden our understanding of the

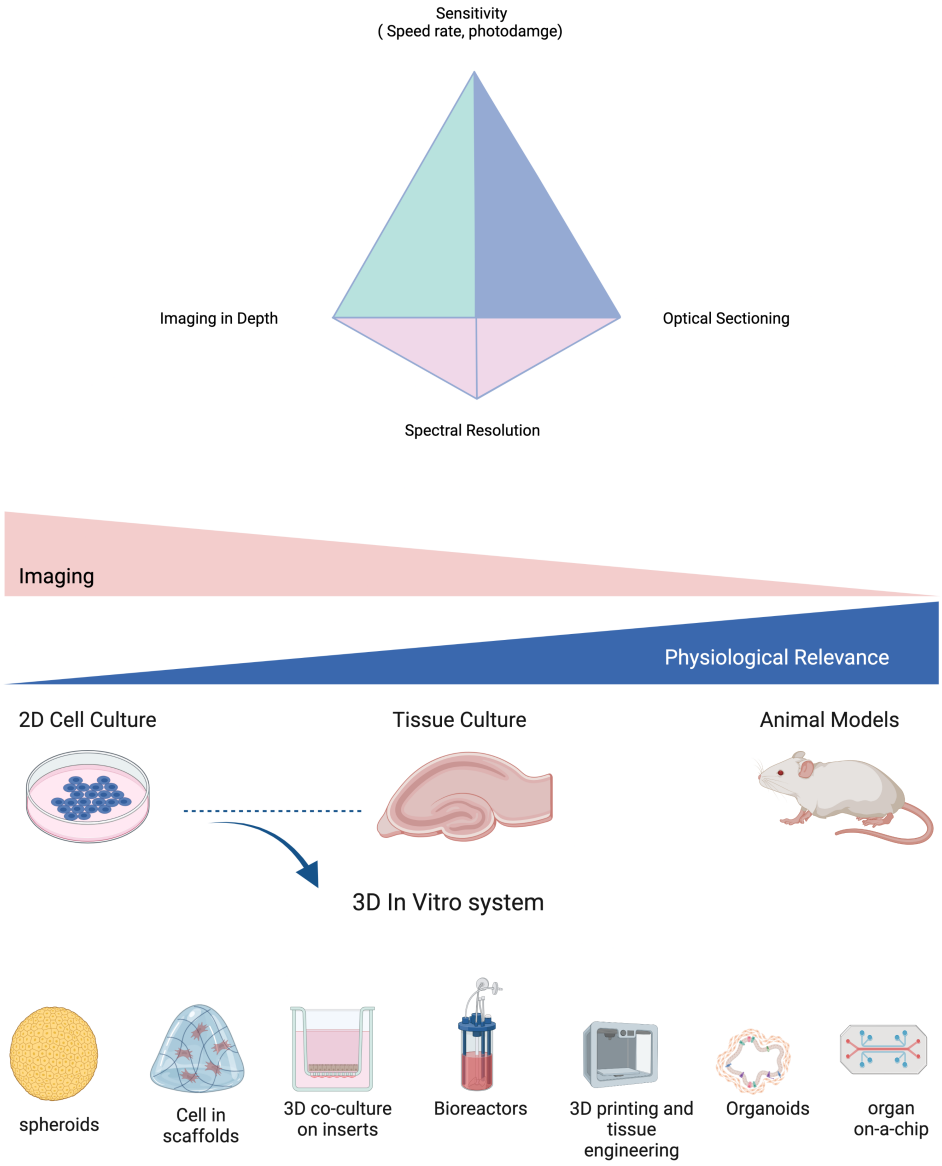

Figure 1.2: Challenges in models of the central nervous system and microscopy techniques. This triangle of compromise suggests that in optical microscopy a tradeoff exists to choose between, optical sectioning of 3D structures, image in-depth, and high sensitivity to generate images. Sparse labeling brings another challenge to the system to perform **simultaneous** multicolor imaging. From 2D to animal models highlight the limitations for imaging and observation. 3D *in vitro* models attempt to provide physiological relevance while versatility for observations in real-time.

morphofuncionality of human brains but also can shape the future of neurodegenerative medicine.

Various 3D *in vitro* systems have been developed with the ability to mimic in vivo functionality and cellular composition of Central Nervous System (CNS) [4] [3] [5] [6]. Among those, organoids [3] [7] [8] and spheroids [9] [4] are the common established models and have been generated with different protocols to bring opportunities for neuroscientists to study brain physiology and pathology in early development. Despite increased efforts to optimize these 3D structures, there are still challenges in order to deeply and dynamically access cellular features due to the physical limits in optical microscopy tools.

The discovery of genetically encoded fluorescent markers [10] coupled with fluorescent microscopy has become indispensable tools for live-cell imaging and extended our ever-growing comprehension of how our brain cells are interconnected and how these connections are tuned over time; processes that are not readily accessible with other tools (e.g. electrophysiology) except through high-resolution imaging. Conventional microscopes, however, are inherently 2D imaging tools. Specialized technologies are therefore required for generating 3D images due to the diffraction of light.

Light can be diffracted, reflected, refracted, or scattered by optical inhomogeneity in living tissues (membrane, nucleus, and other organelles). This light-matter interaction is doubly troubling; the divergence of light can be detected as a bright background, and light scattering (and absorption) reduces the intensity of light, resulting in faint beam arrays, especially in thick and opaque tissues such as seen in brain slices. The first obstacle concerning thick specimens is to remove unwanted fluorescent light from planes other than the plane of interest (in-focus plane). This capability can be achieved through physical (a pinhole in a confocal microscope), intrinsical (two-photon absorption in two-photon microscopy), and computational (spatial filtering in image scanning microscopy) optical sectioning microscopies. Another major set of challenges for 4D (live-cell 3D imaging) is the speed of acquisi-

tion and photodamage that may accompany the generation of 4D images. Reducing photodamage requires fast acquisition with minimal light exposure. The speed of acquisition depends on the sensitivity of the detector to capture the fluorescent and then the efficiency of the image processing and reconstruction.

Here have placed tremendous multidisciplinary efforts on developing microscopy techniques that perform beyond their limits (e.g., super-resolution and optical sectioning microscopy techniques). Yet, a trade-off between optical sectioning, imaging in-depth, and sensitivity must be made. Adding to the current challenges, the ability of the system to simultaneously image multiple fluorophores is crucial to readily visualize neuronal contacts sparsely and collectively so that contacts of individual neurons are visually discriminated (**Figure 1.2**-top). Altogether, the ideal neuronal model and imaging system would generate high spatio-temporal resolution 5D images (3D, real-time, simultaneous multicolor) of neuronal contacts in a physiologically relevant system in a user-friendly manner.

My Ph.D project aims to offer a combination of a 3D-engineered neuronal model compatible with a novel microscopy technique to overcome time-lapse 3D multicolor imaging of neuronal structures to reveal neuronal contacts and remodeling in a more physiological environment to recapitulate *in vivo* conditions.

Chapter 2

3D Engineered *In Vitro* Synaptic Models

Neuronal cell models (cell and tissue culture, animal, and engineered culture models) and their characteristics are introduced by two main aspects: How physiologically relevant they are for studying neuronal contacts and remodeling and how adaptable they can be for performing optical imaging in real-time. Here I state the rationale for optimizing 3D *in vitro* models by addressing the challenges in studying synaptic remodeling and interlinking. Then we categorize neuronal models for such studies and their limitations in physiological aspects, measurements, and observations. The focus will be 3D *in vitro* platforms that compromise between a more physiological system and the versatility to fabricate, observe, and manipulate. Two established central nervous systems (CNS) models, namely spheroids and organoids, are assessed with their strengths and weaknesses and why we choose one over the others. The generation of spheroids leads us to the hydrogel-based templates and chemical and physical properties of hydrogel in the scope of cell culture and hydrogel-based templates. Finally, we propose an approach to fabricating hydrogel templates and the characteristics of this 3D synaptic model of dissociated neurons.

2.1 Neurons and Synapses

Neurons are highly specialized cells that come in several shapes and sizes, depending on their functions. They all have a prominent cell body or soma, which gives rise to the neurofilaments (axons) and branch-like structures (dendrites) responsible for communication throughout the nervous system. Dendrites receive signals from neighboring axons and send them to soma. Neuronal interconnections occur at anatomically identifiable cellular regions called synapses.

The axons typically have branches at their end with tips called terminal buttons that form pre synapses. Dendritic branches form small protrusions known as spines and form the postsynaptic elements at most synapses in the brain. Synaptic transmission is recognized by two main modalities, namely, chemical and electrical synapses[11].**Figure 2.1** illustrates the coexistence of chemical and electrical synaptic transmission at the synaptic level. Chemical synapses refer to the release of a neurotransmitter from one neuron and the detection of the neurotransmitter by the neighboring neuron whereas in electrical synapses cells are directly in contact with a gap junction.

The chemical synaptic transmission process starts with an action potential that triggers the entry of calcium into the neuron. This elevation of Ca^{2+} is recognized by calcium-sensing receptors, followed by vesicle fusion of the synaptic membrane to release neurotransmitters into the synaptic cleft. Then neurotransmitter molecules diffuse across the synaptic cleft and bind to their specific postsynaptic receptors. This process plays a critical role in synapse formation and signal transduction during neuronal development and growth.[11].

Scientists have grouped synapses according to the action of the neurotransmitter release. Namely, neurotransmitters can have either excitatory effects that promote the generation of an action potential in the postsynaptic cell or have inhibitory ef-

fects that help to drive the membrane away from the action potential threshold. A balance between inhibition and excitation of synapses is essential to ensure effective communication processes in the brain and underlies spontaneous firing and/or responding to sensory inputs[12]

2.2 Synaptic Remodeling and Plasticity

For a long time, people used to believe that as human ages, the interconnection in the brain is fixed and no longer changing. It turns out that our nervous systems are constantly evolving through learning and memory formation. This evolution is due to the reversible physiological changes in synaptic transmission. Within a mature nervous system, nerve cells are extensively interconnected in an entangled and dynamic network. The ability of the brain to rewire and change these connections is called plasticity which is associated with learning and memory formation. For a memory to persist, these changes must be either stabilized or consolidated. The reversible alterations are associated with short-term memory and the persistent changes are linked to long-term memory. The Hebbian theory states[13]:

"*when two neurons are repeatedly active at the same time, some growth occurs between them such that, at a later point in time, activity in one leads to activity in the other*"

The study of plasticity and neuronal connections involves morphological and functional changes in neurons at the level of synapses. The latter is typically investigated through electrophysiology (e.g., patch-clamp) when neurons are communicating through electrical and chemical signals. Structural plasticity is studied using time-lapse imaging that shows the dynamic picture of spines and changes in their number and architecture; they can form, enlarge, shrink, and retract in response to different sensory experiences, across developmental stages, and in various learning paradigms.

Structural changes associated with learning can be induced through three ap-

proaches. One way is by studying live animals and the natural learning process. Another way is through long-term potentiation (LTP) which is a form of plasticity that can be artificially induced by electrical stimulation (e.g., patch clamp). The third approach is to investigate, *in vitro* structural plasticity during the early stage of development in neurons[14]. For instance, live-cell observation of neurons transfected for PSD-95 fluorescent protein, a major scaffold protein of postsynaptic densities, revealed that the formations, eliminations, and remodeling of this postsynaptic protein can occur on the time scale of minutes to hours[15] [16]. This suggests that long-term imaging of this event gives an insight into the morphofunctional changes over time leading to understanding better how neurons communicate in health and disease. For instance, neurite and synapse pruning have been observed in psychiatric disorders like schizophrenia spectrum disorders.[17].

The diversity and complexity of brain cell types are far beyond the diversity and complexity of the rest of the body combined. Each region of the nervous system (e.g., hippocampus, cortex, and spinal cord) has its variety of cell types and functions, challenging the quest for closely predictive neural models.

To study the highly dynamic synaptic interconnection events, diverse model systems are used; ranging from animal experimentations to *ex vivo* and *in vitro* models. The ideal system for investigating synaptic interlinking and plasticity should be 1) physiologically relevant and can recapitulate what occurs in the human brain 2) amenable for live-cell microscopy imaging with the ability to resolve the contacts in 3D 3) amenable for further genetic and experimental manipulations (e.g. optogenetics, electrophysiology). The ultimate goal is to look at connections between synapses deeply, dynamically, and as precisely as possible.

2.3 Models for Synaptic Contacts and Remodeling

The history of cell culture dates back to 1885 when a German zoologist, Wilhelm Roux, for the first time, maintained a portion of the medullary plate of a chick

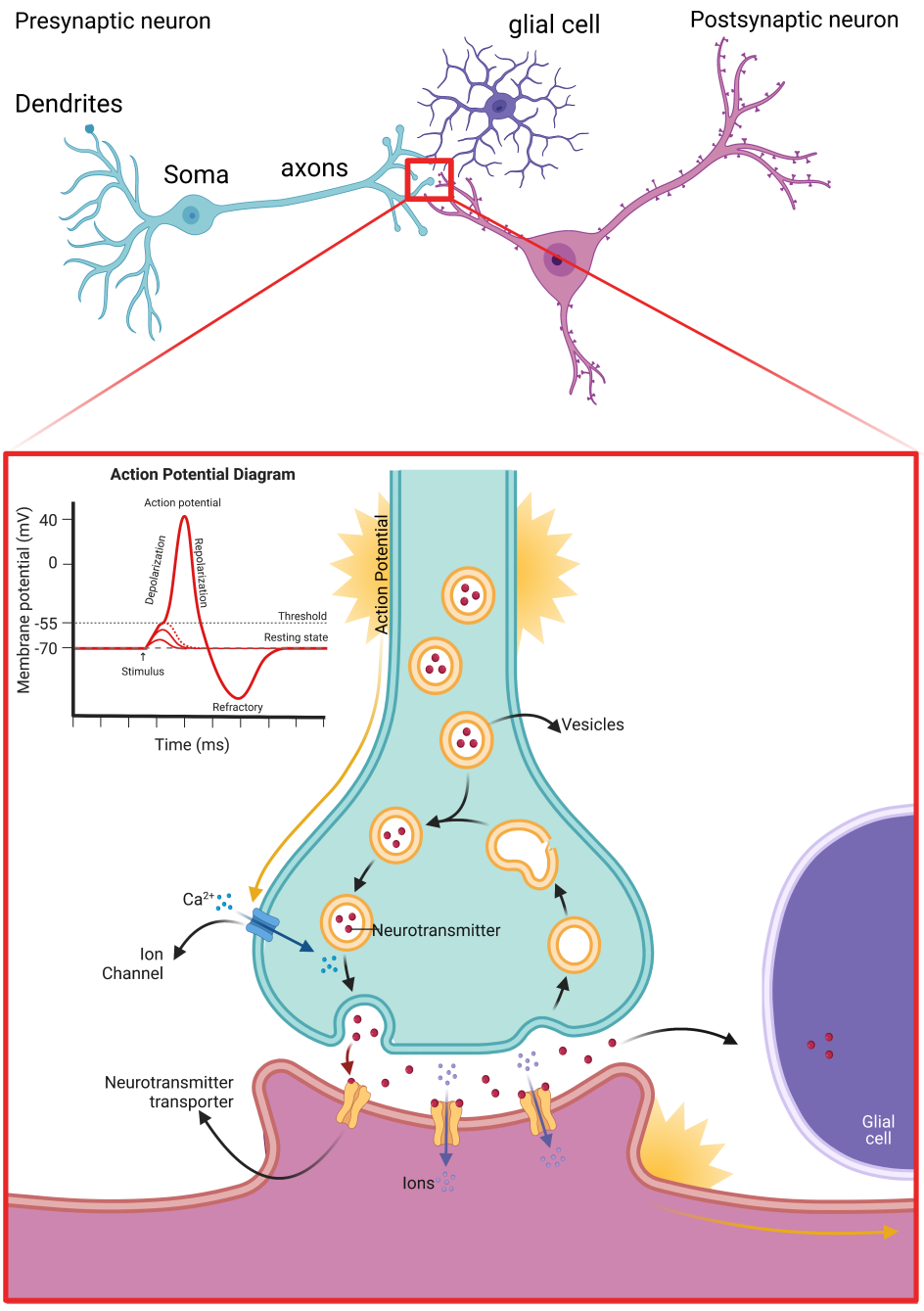

Figure 2.1: Synaptic contacts in the nervous system. Upon stimulations, a neuronal membrane is depolarized to at least the threshold of excitation (70 mV). Blue Neuron (pre-synapse): Then the action potential is fired and propagates along the axon to the axon terminal. This action potential opens calcium channels which trigger synaptic vesicle exocytosis and release of neurotransmitters into the synaptic gap. Pink Neuron (post-synapse): The neurotransmitters diffuse across the synaptic cleft and bind to receptor proteins at the postsynaptic membrane. When neurotransmitters bind to receptors, it allows ions to cross the membrane and cause the membrane potential to change within 0.1 – 2 milliseconds. Purple neuron (glial cell): regulating efficient neurotransmitter release and clearance and pruning away excess synapses.

embryo in warm saline solution for 13 days. Later in 1907, Ross Granville Harrison published an article with an attempt to isolate mammalian cells in laboratory dishes. He observed the development of fibers in nerve cells of frog embryos by placing them in a drop of frog lymph - a technique that microbiologists were widely employing to study bacteria[18]. Despite the additional work of Leighton who maintained the native tissue-like architecture by using gelatin sponges[19] and following modifications by generating cellular aggregations of embryonic cells[20], the 3D culture approach did not become popular as the simplicity of 2D culture dishes for studying cells became standard. In 1887, Petri dishes used in the Robert Koch lab[21] became the preferred method to maintain mammalian cells and have been used ever since.

2.3.1 *In Vivo* and *Ex Vivo*

Live animal experimentations are typically conducted on rodents' brains for investigations including but not limited to, basic functions, drug discovery[22] and cognitive and behavioral neuroscience[23]. *In vivo* rodent models are perhaps the closest biological models used today for research and therapeutic approaches aimed at humans. However, with regard to imaging, it is technically challenging and sometimes impossible to monitor the animal under study due to the optical limitations of in-depth penetrations and resolution. To access and monitor live animals there are different approaches such as open skull windows, thinned skulls, and micro-endoscopic probes. Besides the laborious and invasive surgeries, these approaches may compromise cellular physiology and induce immune reactions or inflammatory reactions[24] [25]. It has been shown that rodent studies, especially in drug discovery, may be a poor predictor of the human body and physiology[26] [27]. Moreover, ethical consideration concerning the use of animals in scientific experiments and medical science research has long been a topic of intense ethical debate. With the advancements in medical research and technology, the number of animals sacrificed in research has increased. Currently, the policies and regulations focus on balancing

the benefit of achieving knowledge, and the pain animals are subjected to during the experiments. These regulations include designing meaningful consequential research that may help with the replacement, refinement, and reduction of animal use in the experimentations[28]. An alternative to animal experiments is a model generated from humans and exhibits human cells to elucidate cellular physiology and anatomy. Human Stem cell technology has shown great potential in delivering more physiological relevant answers and may decrease the need for animal experimentation, if not all, in *in vitro* experimentations. This makes the *in vitro* platforms advantageous to create cellular models generated from human cells.

Alternatively from *in vivo* models, *ex vivo* has been widely adopted and has proven to be experimentally easier to manipulate[29]. Organotypic slices are brain slices of 100–400 μm thickness, which can be kept in culture for several weeks. This model is the closest to *in vivo*, as it preserves the organization, architecture, and microenvironments of the native tissue, which allows the identification and manipulation of defined neurons and synapses. However, there is a significant loss of brain function once the tissue is removed from the body[30]. Another drawback in the use of brain slices is that to maintain the slice in culture for several weeks, it is imperative to obtain tissue thickness around 350 μm which may arise challenges for imaging in depth. Moreover, the natural opaqueness of brain tissue has traditionally limited observations using microscopy techniques in live imaging. Due to the different refraction indexes (RI) of cellular components, the light traveling through the sample is absorbed and scattered. Thus, a brain slice can be efficiently imaged with a thickness limited to 150 μm using confocal microscopy (This can increase up to 1 mm using non-linear absorption techniques such as two-photon microscopy).

Modalities with single-cell resolution often require mechanical slicing into thin sections which results in tissue distortions and hinders the accurate reconstruction and quality of the 3D volumetric images. Imaging deep brain structures connectivity using light microscopy was historically only possible by histological sectioning and

more recently has been combined with tissue clearing assays[31]. Reducing optical mismatches between the cellular compartments significantly improves the optical transparency in the biological samples. This can be done in a fixed sample through various tissue optical clearing methods to homogenize the scattering throughout a sample and increase the transparency of the tissues. Therefore, live-cell imaging of tissue cultures is hampered and limited cultured tissue application mostly to fixed brain slices.

2.3.2 Extending to The Third Dimension *In Vitro*

Maintaining the cell's functionality is not only limited to keeping them fed and uncontaminated, surrounding environments impact their behaviors quite dramatically. Every organ has an ECM with unique composition and a complex 3D architecture. All the cells in native tissues interact with adjacent cells and their environments through biochemical and mechanical cues and maintain it in health, remodeling them in disease[32]. Thus, the complex surrounding cells (stromal cells) and macromolecules as well as the extracellular matrix play roles in tissue and organs' functionality and optimal cell behavior. The ECM composition and stiffness play an important role in the health of cells. For instance, metastatic cancer cells (lung, breast, and pancreas cancer) change their stiffness to mechanically adapt to ECM and are more than 70% softer than healthy cells[33]. Another example to highlight the importance of the ECM for brain cells is that the ECM of the nervous system has a distinct structure and composition, such as hyaluronic acid (the most abundant), tenascins, fibrous proteins, Reelin, integrin ligands (other components like collagen and laminin are less abundant in the brain compared to other organs) with a low elastic modulus (from 110 Pa to 1 kPa). A stiffer environment than natural (i.e., Petri dishes of 1 GPa) leads to abnormal neural cells differentiation, proliferation, and migration. Similarly, matrix porosity influences cell migration and metabolic efficiency as large pore sizes enhance nutrient and oxygen flow[34] [35].

During development and throughout life, these ECM provide cues that promote synaptic plasticity and maintain the homeostasis of neural circuitries [36] [37]. On the contrary, cells growing on the stiff 2D substrate have nonphysiological stiffness that does not fulfill the biochemical functionality of native tissues. It has been shown that many biological responses such as morphological characteristics [38], proliferation, differentiation [39] gene and protein expression [40], response to stimuli, drug metabolism [41] [42], and general cell function [43] differ significantly from those in the original organ or tissue, when using 2D stiff culture templates. Therefore, these stiff flattened 2D substrates may lack predictive values for preclinical cell-based drugs, toxicity screening assays, and morphofunctional study of cells. Despite their lack of accurate prediction, 2D cultures are amenable to all microscopy imaging techniques as well as cell-biology manipulations. While there is no substitute for the low cost and simplicity of 2D cell culture studies or the complexity provided by in vivo systems, 3D in vitro tissue modeling is to fill in the gap that exists between the 2D in vitro and in vivo approaches: to provide human-relevant information that is highly reproducible with control over observation and manipulations. On one hand, 3D cell culture models fill the gap for the lack of complexity and physiological relevance of 2D culture. On the other hand, they can be engineered to increase the versatility of manipulations and observations. The emergence of *in vitro* 3D cellular platforms along with the isolation of human-derived stem cells and hiPSCs created exciting opportunities for neuroscience communities to develop human models of CNS [44] [45].

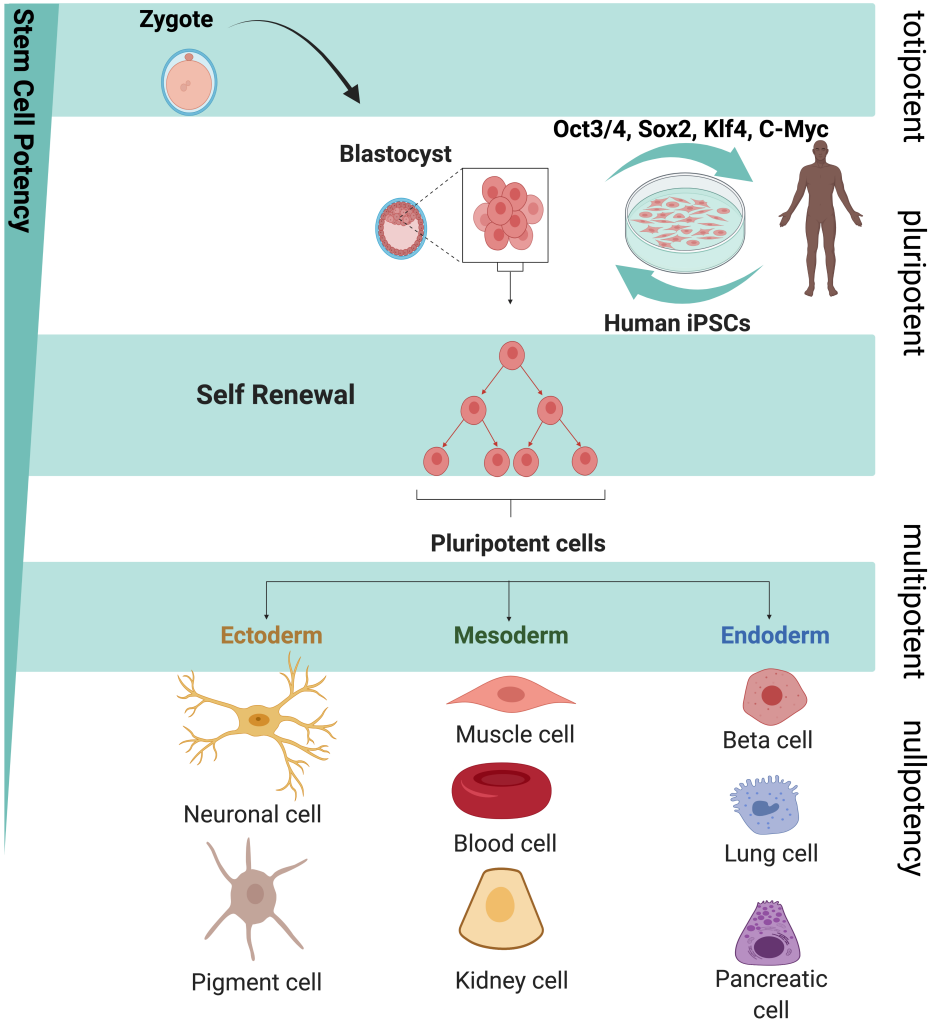

Figure 2.2: Embryonic and Induced Pluripotent Stem Cells. Human fertilization creates a diploid zygote with the ability to produce all the differentiated cells in an organism and initiates a series of cell divisions that result in a multicellular embryo. Embryonic stem cells are derived from the inner cell mass of the blastocyst and can differentiate into all cell types of the endoderm, mesoderm, and ectoderm lineages using appropriate signals. Adult (somatic) cells can be reprogrammed to an embryonic state by introducing Octamer 3/4 (Oct4), sex-determining region Y box–containing gene 2 (Sox2), Kruppel-like factor 4 (Klf4), and cellular myelocytomatosis oncogene (c-Myc).

2.3.3 Stem Cells: "Off" Mice and Men

Stem cells are unspecialized cells that have not yet specified their morphology or protein expression profile to a specific cell or tissue. They can differentiate into many cell types and carry the ability to proliferate and expand themselves through self-renewal characteristics. Stem cells can be grouped into embryonic stem cells or adult stem cells based on their potency capability; embryonic stem cells are pluripotent and can differentiate into all the cell types of an adult body. Adult stem cells found in an organ or tissue of the body can differentiate into the specific cells within the tissue niche. In 1981, Martin John Evans with Matthew Kaufman cultured mouse embryonic stem cells for the first time in the laboratory and years later were awarded the Nobel Prize in physiology and medicine together with Mario Capecchi, and Oliver Smithies[46]. A few years later, in 2012, Shinya Yamanaka and John Gurdon were co-recipients of the Nobel Prize in physiology and medicine for discovering Induced Pluripotent Stem Cells (iPSC), converting mature cells into stem cells[47]. This turning point has provided a promising approach for investigating and modeling human physiology and pathology. The iPSCs are somatic cells with the co-expression of pluripotency-related transcriptional factors. These induction factors convey pluripotency and convert them to pluripotent stem cells. The factors involved in inducing pluripotency are Oct3/4, Sox2, Klf4, and c-Myc (OSKM) and play an essential role in gene regulatory network GRN in early development. By introducing the combination of these transcription factors into somatic cells, the pluripotency, proliferation, and dormant differentiation characteristics of cells are maintained similarly in embryonic stem cells[48] [49]. This leads to the "reprogramming" of an already differentiated cell into cells with the potential to renew themselves and the ability to differentiate into cell types from all three germ layers[50] (**Figure 2.2**). Discovery of stem cells, and especially iPS cells have received widespread attention in four major fields; regenerative medicine[51], disease modeling[52] and treatment[53], and drug discovery[54]. The iPSC discovery later led to

the creation of models known as mini-brains or brain organoids, generated from human stem cells. These specialized organoids highly mimic cellular organization and morphogenesis of the brain and are used in disease models and morphofunctional studies of cells[55] [7] [56] [57].

2.4 Engineered 3D *In Vitro* Models

To study the CNS various 3D *in vitro* culture systems, such as engineering-based models[5] [6], organoids[3] [7] [8], and spheroids[58] [8] have been used and appreciated for their ability to generate neural tissue structures that can recapitulate native tissues' microenvironment and organization. These techniques offer the ability to incorporate diverse cell types and materials that promote physical and biochemical cues. Three-dimensional culture systems can be grouped into two main categories of scaffold-based and scaffold-free assays (see **Figure 2.3**). Scaffold-free 3D culture technology takes advantage of a natural self-aggregation[59] of cells into sphere-shaped cell assembly. The most common scaffold-free technique to fabricate sphere-shape aggregations is to use low adhesion plates with ultra-low attachment coating that prevents cells from adhering onto the surface, therefore, allowing the cells to aggregate and form cellular assemblies. Besides their simplicity, these techniques provide spheroids of different sizes, depending on the initial number of cells, and show relative oxygen and nutrient gradients like in tissues. Hanging drop microplates is another common technique to grow cells in a 3D scaffold-free manner. In this method, cell aggregation is promoted using surface tension and gravitational force and has been primarily used for therapeutic application and cytotoxicity studies[60]. However, due to the small volume of the medium, the risk of evaporation can potentially affect the osmolarity of the culture and the viability of the cells. Another approach to fabricating 3D culture is by using spinner culture or rotating vessels (spinner flask) in which the self-assembly occurs by stirring or rotating the culture vessel. Similarly, perfusion bioreactor technologies prevent cell adhesion by

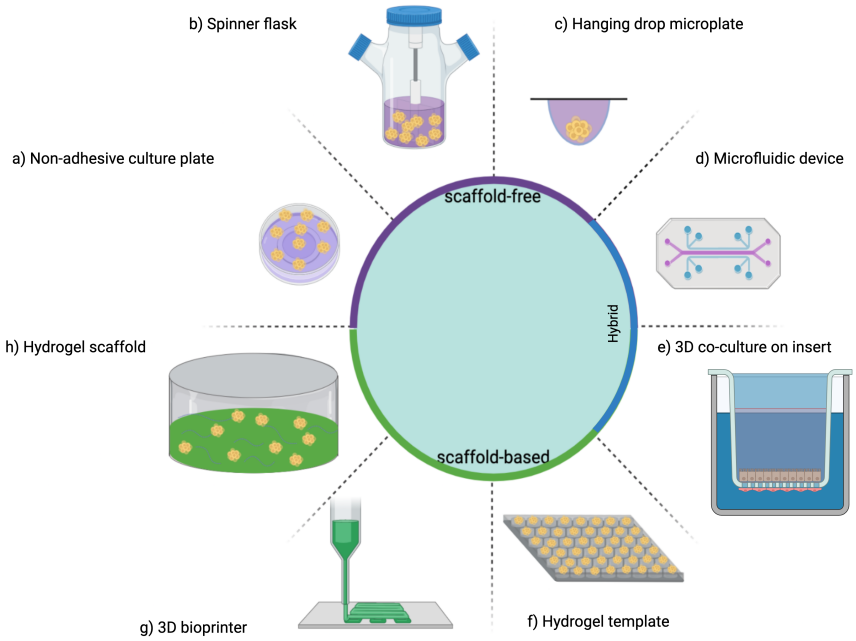

Figure 2.3: Common 3D techniques used for creating 3D cell culture a-d) Scaffold-free methods. a) suspension cultures: relies on the self-aggregation of cells in artificially low adhesion coating that promotes spheroids formation. b) Spinner flasks or bioreactors are based on continuous paddle stirring to ensure the cells are suspended and the distribution of various nutrients and oxygen. c) Hanging drop cultures use special culture plates in which cells are held by capillary forces in nanoliter-sized wells promoting cellular aggregations. d-e) Hybrid: use a matrix or a scaffold to support scaffold-free systems d) Microfluidics or Lab-on-chip is the technology of fluid manipulation in channels allowing oxygen and nutrients to flow in the culture. e) 3D co-culture insert: the insert contains one cell type whereas the well or dish contains the other cellular population. These systems include an air-liquid interface that permits cell-cell interactions of different cell types with secreted soluble factors to diffuse. f-h) scaffold-based f) hydrogel-based microwells arrays induce topological transformations of standardized cellular microstructures with size and shape of interest. g) bioprinters contain an aggregate of a few thousand cells in bio-inks. Layers are subsequently added and the bioink spheroids slowly fuse. h) hydrogel scaffold: cells are grown in the presence of sponge-like structures and growth factors mimicking the ECM.

creating a microgravity environment providing controlled delivery of nutrients and biomimetic stimuli. However, the main disadvantage of these techniques is the need for many optimizations of culture conditions to obtain uniform spheroids to enhance reproducibility [61]. Microfluidic systems, so-called Organ-on-Chips, are among techniques that optimize oxygen and nutrient flow, waste removal, pH, and temperature thanks to their diffusion process- allowing the cell to contact fresh medium in a controlled environment [62] [63]. Microfluidic systems suffer from the variability of the spheroids and low standards throughput. Moreover, designing the most efficient protocol requires rather complex pieces of equipment (external pumps, tubing, etc.). Despite the significant evidence behind the values and importance of 3D cultures, there are currently few 3D CNS tissue models for investigating neuronal contacts. However, techniques being used in other fields can be borrowed and optimized and serve as 3D *in vitro* synaptic models. Two established systems for neuronal tissue are known as spheroids (or neurosphere) and brain organoids. These two techniques for 3D aggregations of CNS cells have been explored in the recent past.

2.4.1 Brain Organoids

Organoids are organ-like multicellular 3D structures that demonstrate a high level of complexity and physiological relevance. These self-organized 3D microstructures are typically generated from Adult Stem Cells (ASC), embryonic (Embryonic Stem Cells (ESC)), or induced pluripotent stem cells (iPSC) which gives the ability to self-renew sustainable culture and give rise to cells of different organs [7] [64] [65]. In recent decades, many methods have been developed to generate and maintain these structures, helping our understanding of the functionality of human organs by using human stem cells. Organoids are typically maintained for long times, months, to even a year. To generate 3D aggregations typically the stem cells are cultured and differentiated into the cell types of interest, then they are transferred into Matrigel

droplets to promote expansion. To grow organoids beyond the limit of oxygen and nutrient diffusion experiments use agitation bioreactors (**Figure 2.4-H-top)**. Yet, the core region tends to necrotically suffer due to inadequate oxygen and nutrients, leading to cell death[66]. Organoid culture has been described and improved for a variety of other organs such as lung, intestine, prostate, and kidney[67][65]. Brain organoids exhibit fundamental features of human tissues[2][7][56][57] and were introduced by Lancaster and Knoblich (2014). They used pluripotent stem cells which gave insight into the structure of the early embryonic central nervous system (**Figure 2.4-H-bottom**) Organoids are particularly appealing and useful for disease models and patient-specific therapeutic approaches[68][55]. Despite their potential to mimic human pathophysiology, these 3D self-assemblies suffer from several shortcomings. The primary drawback includes their low throughputs and reproducibility. This is a result of their spontaneous formation of aggregations with no control over the size and shape of the structures. Furthermore, these structures lack some features essential for the physiological functions of the CNS, such as vascular perfusion, immune cells, and mechanical cues[69][70]. More importantly, with regards to imaging, organoids face the same challenges as tissue cultures[55][7]. Microscopy imaging of CNS organoids has been performed only through thin slicing of them combined with immunohistochemistry assay and revealed their potential to mimic cellular organizations and morphology of the brain. Their greater potential is yet to be explored using 3D live-cell microscopy imaging. However, this is yet to be realized as the organoids are large (>1 mm) which perpetuates light penetrations and thus the image quality of the structures.

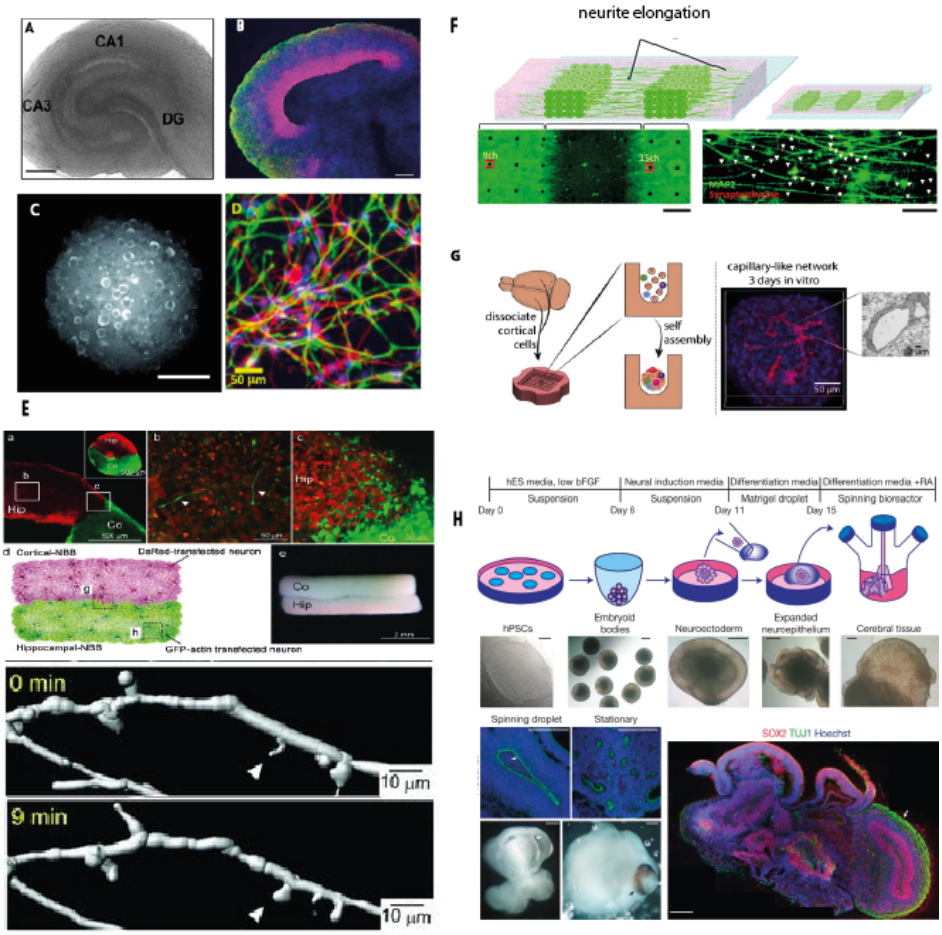

Figure 2.4: 3D *in vitro* models of CNS. A) Organotypic hippocampal slice cultures[71] B) cross-section of human organoids[2] C) Cortical spheroid[9]. D) 2D culture of human neurons[72] E) hippocampal and cortical engineered tissue generated from spheroids (Co) ad hippocampal (Hip) neurospheres are, previously formed in a PDMS micro-area, collected in a millimeter-sized PDMS mold to generate neural building showing neuronal connections. The bottom 3D time-lapse images illustrate the morphology of spine-like structures in the dendrite of GFP -actin-transfected neurons treated with IMARIS software[58]. F) (Top) Schematic of PDMS micro-areas and collagen fibers. (bottom) The 3D neuronal network formed on multielectrode arrays shows the direction-controlled neurites between two somata areas[73]. G) Cortical neurons form spheroids in agarose hydrogel arrays and grow processes[4] H) (Top) Schematic culture of organoids generated from HiPC cells followed by bright-field images of each step. (Bottom left) Sectioning and immunohistochemistry of neuroepithelial tissues in spinning and stationary suspension[2]. Scale bar = A) 500 μm, B) 10 μm C) 100μm, F) 50 μm, H) 200 μm.

2.4.2 Neuronal Spheroids

Spheroids are spherical cellular units that can be single cells or multiple cell types. They should have viable cells that allow cell-cells, cell-matrix interaction, and biomechanical properties to achieve a level of biomimicry. Spheroids are self-assembled structures formed by either spontaneous or forced assemblies in the form of spheres. Scaffold-free approaches generate spheroids by natural processes (microenvironment, ECM, growth factors, etc.) that mimic embryogenesis, morphogenesis, and organogenesis. In the scaffold-based method, cells are plated on a surface (planar, cavities, etc.) which inhibits cell adhesion and therefore, promotes forming clusters in suspension without exogenous materials. In both approaches, cells undergo spontaneous self-assembly in response to the cue they generate. While spheroids are less complex compared to organoids in mirroring tissue-like structures due to a lack of clear organization, they recapitulate better *in vivo* morphology and functionality compared to 2D cultures. Spheroids composed of brain cells are also known as neurospheres. These self-aggregations secret their own ECM and therefore create and maintain a native-like surrounding matrix[74]. The neurospheres generated by stem cells provide valuable systems for studying neurogenesis and neural development. In the recent past as the most advanced technique, microwell arrays have attracted remarkable attention. Since seeding cells is simple and each well has geometrical uniformity, a uniform-sized neurosphere is generated without any external stimulations. Dingle and colleagues created neuronal spheroids of rat neonatal cortical cells using micro-molded agarose wells. Remarkably, after 14 Day In Vitro (DIV), electrophysiology experiments showed that neurons within the spheroids were electrically active which proved that spontaneous postsynaptic currents observed in the synaptic network of neurons also reside in spheroids (**Figure 2.4- C and G**). The arrays of neurosphere can be generated by methods such as microwell arrays from

micropatterned agarose[9] and Polydimethylsiloxane (PDMS) micro-areas[58] [75] [76]. These hydrogel templates are popular ways to create arrays of spheroids because of their capability to fabricate standardized spheroids with controlled shape and size.

2.5 Hydrogel-Based Micro Arrays

Among microengineering systems[77] [78] [79] [80] [81] [82] [83], hydrogel microwells provide an excellent platform to mimic the functionality and native morphology of cells in 3D. Microwell arrays are systems that consist of multiple topological recesses of polymers with standardized shapes and sizes capable of trapping cells to form aggregations within a short period of time. These aggregations then form 3D cellular structures with uniform size and shape that can mimic *in vivo* cell-cell interactions. The substrate of these wells can be treated with a non-adhesive layer to facilitate the self-assembly of cells. This system has been used in tissue engineering, cell-matrix interaction and single cells studied[84]. Microwell arrays have been fabricated most commonly by PDMS, (Poly Ethylene Glycol (PEG), or agarose hydrogels to produce uniform-sized spheroids without external stimulations. These hydrogel-based templates can be fabricated on a large scale to produce spheroids in a high-throughput manner[85] [86]. Hydrogels are widely used in biomedical research due to their ECM-mimetic properties that exhibit physical characteristics similar to soft tissues. In general, the fabrication of microwell arrays is done through molding or stamp that involves lithographic processes. In photolithographic methods, photosensitive material, and optical radiations are used to fabricate microscale templates allowing the user to define the precise geometry and providing spatial control for microwell preparation. The procedure to design and fabricate a microwell array is shown in **Figure 2.5**. This protocol, developed by M.P Lutolf and colleagues[78], includes two main steps: 1) fabrication of PDMS micro-stamp **Figure2.5 step1** and 2) PDMS stamping to micro mold PEG hydrogels **Figure2.5 step2**. After fabrication of the PDMS micro stamp through lithography, the mixture of PEG pre-polymer and pho-

toinitiator is applied onto an acryl-functionalized substrate. Next, the PDMS stamp is placed onto the hydrogel reaction mixture and exposed to UV light by which the photocrosslinking process starts. PEG hydrogel is polymerized such that the PDMS stamp can be detached without deforming the PEG gel. The hydrogel array with the molded shapes is ready for cell seeding and further measurements. Hydrogel microwells fabrication through micro-molding enables great control over the size and dimensions of the wells but requires access to clean rooms and expensive machines. In addition, it may suffer from a low production rate due to the multistep process. Also, the stamping process imposes limitations on the softness of the final hydrogel arrays, as they may deform upon stamp removal.

2.5.1 Hydrogels

Hydrogels are crosslinked structures with a high-water content which allows retention of large amounts of water. Hydrogels are vastly used in biomedical and pharmaceutical applications mainly because of the intrinsic elasticity properties and high affinity for water that make them similar to the natural tissue scaffold [87] [88]. Parameters that influence and describe hydrogel properties including swelling, mesh size, stability, and degradation, are linked and affect one another. For example, hydrogel structures must maintain correct stiffness in order to preserve their structure and integrity for cell culture applications as high stiffness results in brittle structures which can be readily deformed. Two types of hydrogels, namely natural and synthetic, are extensively studied and used in various biomedical applications including drug delivery and tissue engineering. Generally, the rigidity of most hydrogel materials is tunable by changing polymer concentration or chain length that directly affects the network density. Natural hydrogels (e.g., collagen, fibrin, hyaluronic acid, Matrigel) are used as milieus of endogenous signals, stimulating the cell-cell and cell-matrix interaction that underlie functionality and formation of native tis-

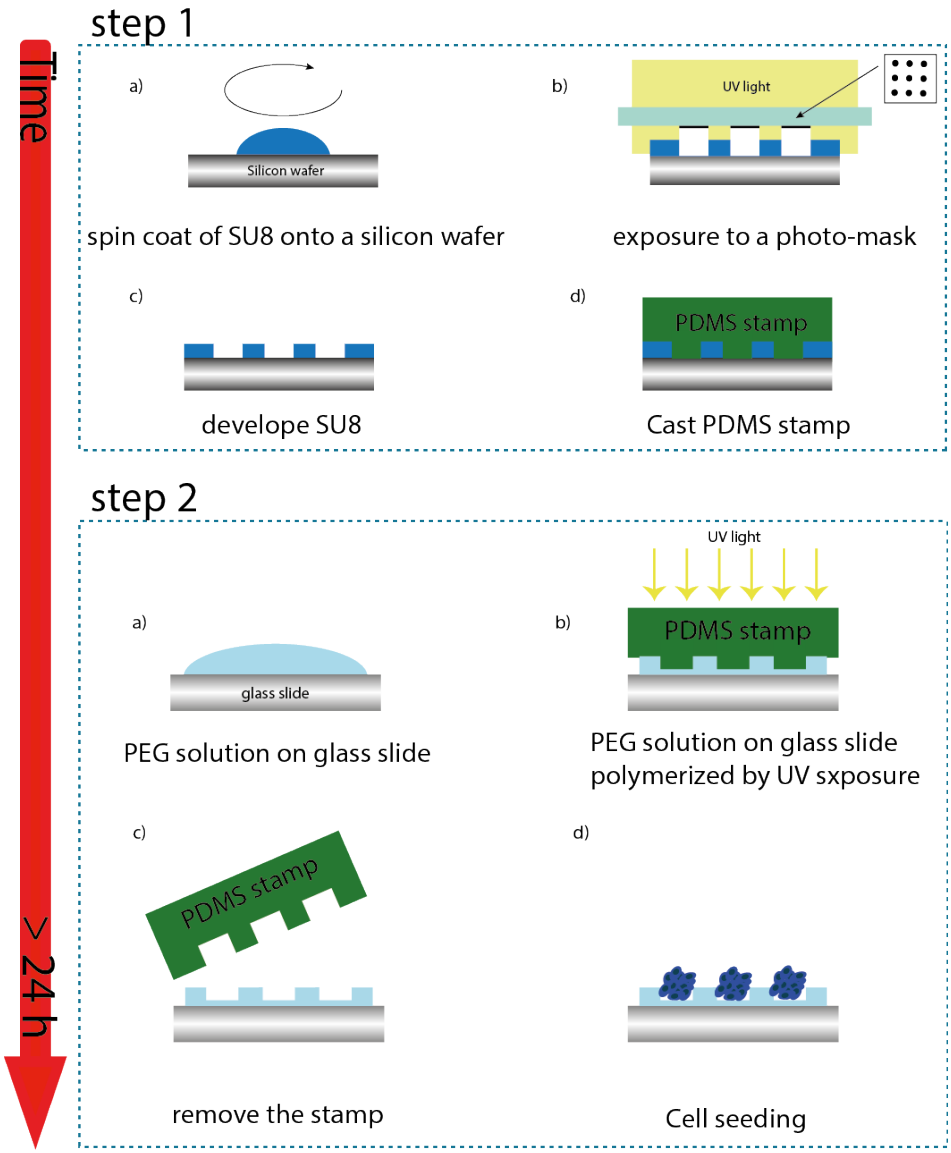

Figure 2.5: Fabrication of PEG-based microwell arrays includes step 1) Fabrication of PDMS stamp via photolithography and step 2) Micromolding of PEG microwell array using a PDMS stamp (modified scheme from[78])

sues. These features have made them appealing for scaffold-based 3D cell culture applications[89]. However, this family of hydrogels is complex, variable, and poorly established, making it challenging to precisely determine which biochemical and biomechanical cues promote cellular functions. To improve the physicochemical properties of hydrogels, scientists have combined a well-defined synthetic scaffold with physiologically relevant cues to tailor the hydrogel's chemistry, properties, and degradations to promote tissue/cell growth in a more physiologically relevant milieu. Thus, synthetic hydrogels have the advantage of the manipulation of both mechanical and biochemical. The process and method of crosslinking in hydrogels play a critical role in biochemical and mechanical properties such that hydrogels with the same constituents but a different crosslinking method and structure can exhibit various functions[90]. Based on their type of crosslinking or microstructure, hydrogels can be divided into two categories: chemical or physical nature. The physical networks are formed through changes in environmental conditions and have transient junction results from molecular entanglements and physical interactions (e.g., thermosensitive hydrogels, ionically crosslinked hydrogels, hydrogen-bonded structures) and are, therefore, reversible with relatively weak bonds, whereas chemically crosslinked networks create covalent bonds between polymer chains, resulting in stable hydrogels with permanent bonds[91]. The chemical polymerization process of hydrogels can occur through radical polymerization, chemical reactions, energy irradiations, and enzymatic crosslink[92]. Generally, chemically crosslinked gels have tunable mechanical properties and therefore are more widely used where certain swelling rates or mechanical strength are needed[93]. For instance, the elastic property of hydrogels is essential for the stability and stiffness of the networks. It also controls the conversion of mechanical information from the microenvironment into biochemical signaling, which directly has consequences for cellular behaviors like spreading, migration, and differentiation (**Figure 2.7**).

2.5.2 PEG Hydrogels

Synthetic polymers can be derived from poly (hydroxyethyl methacrylate) (Poly HydroxyEthyl MethAcrylate (PHEMA)), poly-(ethylene glycol) (PEG), and poly(vinyl alcohol) (Poly Vinyl Alcohol (PVA)). Among them, PEG hydrogels have a long history in material biomedical research and have shown great potential owing to their unique properties[95]. PEG is one of the most widely studied and used materials for its biocompatible water-soluble, and ECM-mimetic properties that make it attractive in biomedical science and drug discovery. The versatility and biocompatibility of the PEG macromer chemistry have developed numerous hydrogel systems for regenerative medicine applications[96]. The word PEG can refer to the polymer chain with a molecular weight below 20000, while polyethylene oxide (PEO) is used for larger polymer[97], showing their tunable polymer length. PEG polymers can

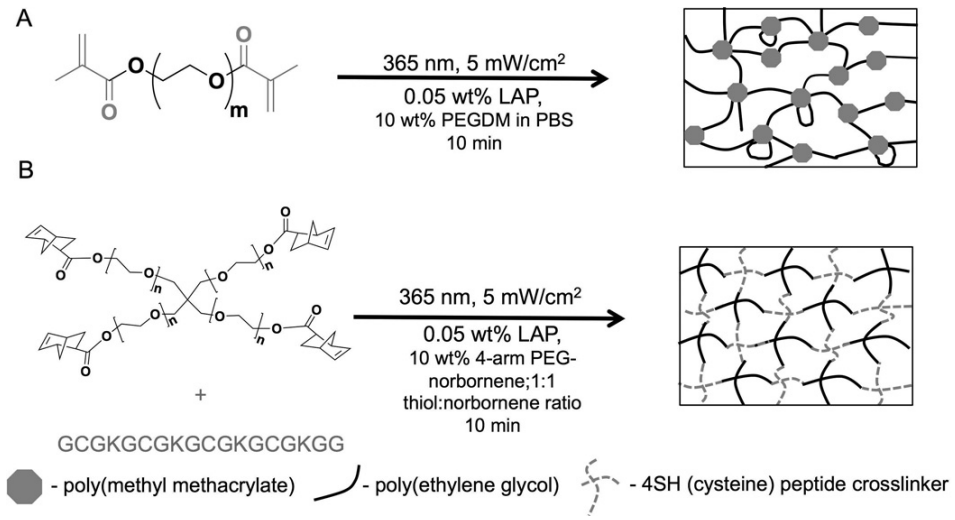

Figure 2.6: Chain- and step-growth polymerizations of PEG macromers. (A) chain-growth polymerization of poly(ethylene glycol) dimethacrylate (PEGDM) macromers and (B) step-growth polymerization of poly(ethylene glycol) tetranorbornene (4-arm PEG-norbornene) and tetrathiol peptide crosslinker[94]. The final crosslinked gels show different network chains as a result of chain-growth and step-growth polymerization.

be bonded covalently to create crosslinked networks. Their physical, mechanical, and biological properties can often be tailored by changing the molecular weight, crosslinker length, crosslinking density, level of degradation, and method of polymerization[89]. Hydrogel mesh sizes or molecular porosity measures the distance between two adjacent crosslinks in hydrogel networks and typically influences the diffusivity or nutrient flux throughout the matrix[98]. **Figure 2.7** depicts the mesh size of two different PEG molecular weights and indicates the effect of mesh size on the stiffness of the PEG networks; By increasing the molecular weight of the hydrogel, the mesh size of the networks increase, making the hydrogel stiffer and therefore decrease the rate of diffusiveness in the hydrogel[99]. The amount of water that hydrogels can take up is associated with the polymer network, hydrophilicity, and crosslink density, where the softer hydrogels show more minor swelling. The mesh size or molecular porosity measures the distance between two adjacent crosslinks in hydrogel networks that typically influence the diffusiveness or nutrient flux throughout the matrix[98].

2.5.3 Photocrosslinking of a Common Hydrogel

As mentioned before, radical polymerization can be used to fabricate covalently crosslinked hydrogel networks. In radical polymerizations, the photocrosslinking process is triggered by radicals generated from initiators which are excited/decomposed by an initiation energy source, such as photons, heat, or redox potential. Radical polymerizations are relatively fast and, in some cases, with the advantage of spatial-temporally control over the reaction kinetics[100]. Photopolymerization is among those initiation sources that permit control over polymer formation. Macromers such as PEG carrying reactive double bonds can respond to light stimuli for structural or morphological transitions. Because the cross-linking reaction can be precisely modulated by light, photopolymerization brings many exciting and unique

features including the control of precise locations at defined times and light intensity for photocrosslinking to fabricate hydrogel construct with a simple, fast, and low-cost process and more importantly *in situ* and in a minimally invasive manner[92]. The strategy behind the photocrosslinking process is based on using hydrogel pre-polymers in a liquid state that can be cured upon exposure to light of a specific wavelength, commonly Ultraviolet (UV), to create free radical molecules and then form the chemical crosslinker between polymer chains. These radials are essential for the

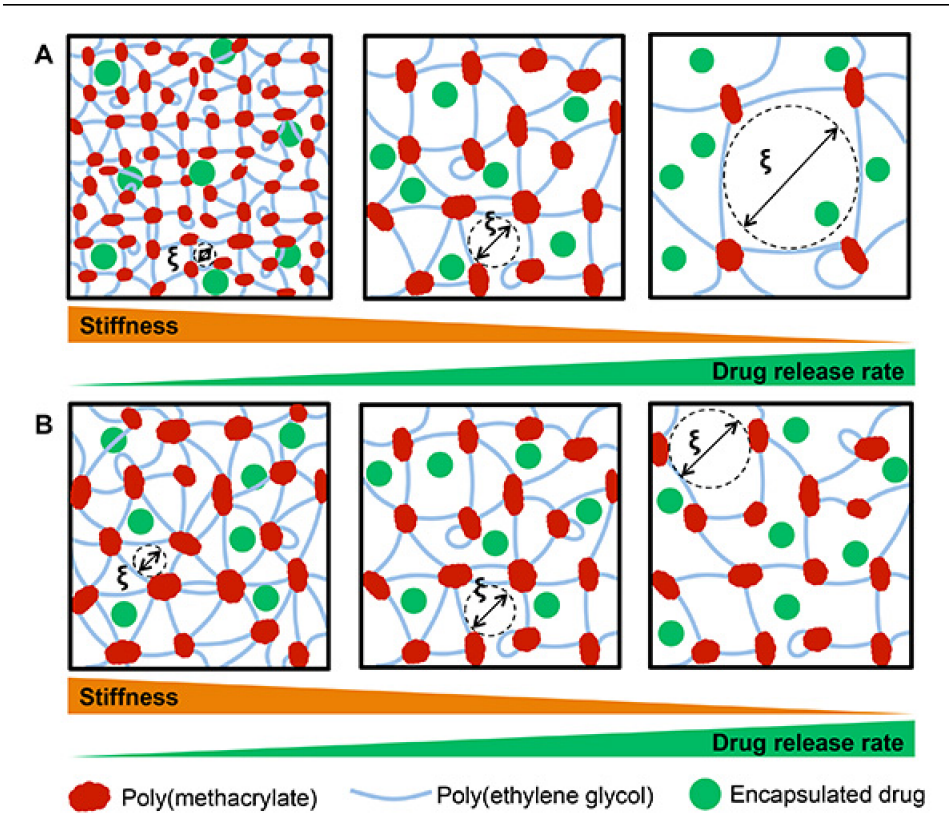

Figure 2.7: PEG molecular weight and weight percentage and stiffness of the PEG hydrogel A) PEG with higher molecular weight (left to right) weight percentage increases hydrogel mesh size, decreases stiffness, as a result, higher flow within the gel. B) PEG with a lower weight percentage of PEG (left to right) used to form hydrogels increases hydrogel mesh size, decreasing hydrogel stiffness and increasing the rate flow adapted from[99].

initiation of reactions but may negatively affect cells and cause cytotoxicity. The most commonly used photocrosslinkable hydrogel chains include poly(ethylene glycol) diacrylate (Poly Ethylene Glycol DiAcrylate (PEGDA)), gelatin methacryloyl (Gelatin MethAcryloyl (GelMA)), and methacrylate hyaluronic acid (Methacrylate Hyaluronic Acid (MeHA)) and are widely characterized in tissue engineering applications[93]. Photopolymerization can be carried out via free radical polymerization and bio-orthogonal click reactions. The former is the most common reaction used in the synthesis of hydrogels. Free-radical reactions are typically based on chain-growth polymerization mechanisms with methacrylate-functionalized hydrogel prepolymer (e.g. PEG) with rapid fabrication and tunable material properties[101]. In PEG macromolecular monomers (macromers), chain-growth polymerizations occur as radicals propagate and react with the unsaturated vinyl bonds present in the prepolymer. This reaction leads to the formation of high molecular weight kinetic chains PEG crosslinks. For instance, PEG-diacrylate (PEGDA) monomers undergo acrylate-acrylate chain-growth polymerization, promoting the establishment of chemical crosslinks between the polymer chains[94]. This reaction enables tunable mechanical, degradation, and biological properties in hydrogels. However, radical-initiated chain-growth polymerization exhibits few limitations, including relatively poor control over the photochemistry kinetic in the crosslinking process, oxygen inhibition, unreacted double bonds residuals that residual chemical crosslinkers might react negatively with biological molecules and cause cytotoxicity, and heterogeneities of polymer networks[102] [103] [92]. Bio-orthogonal click reaction, on the contrary, creates hydrogel with structurally uniform crosslinked hydrogels with minimal heterogeneity based on step-growth polymerizations[104]. For instance, Thiol-ene is known as click reactions and can be used with a variety of "ene" functional groups to trigger the addition of thiols to carbon-carbon double bonds in the hydrogel pre-polymers[94]. This reaction allows tuning hydrogels' mechanical properties and degrading rate with no risk of cytotoxicity[105]. In addition, photo click chemistry

does not promote oxygen depletion and can proceed with higher efficiency and faster kinetics when compared to free-radical polymerization[103]. However, the practical application of thiol-ene photoclick reaction is limited due to the life stability of several hours to several days in thiol-containing small molecules[93].

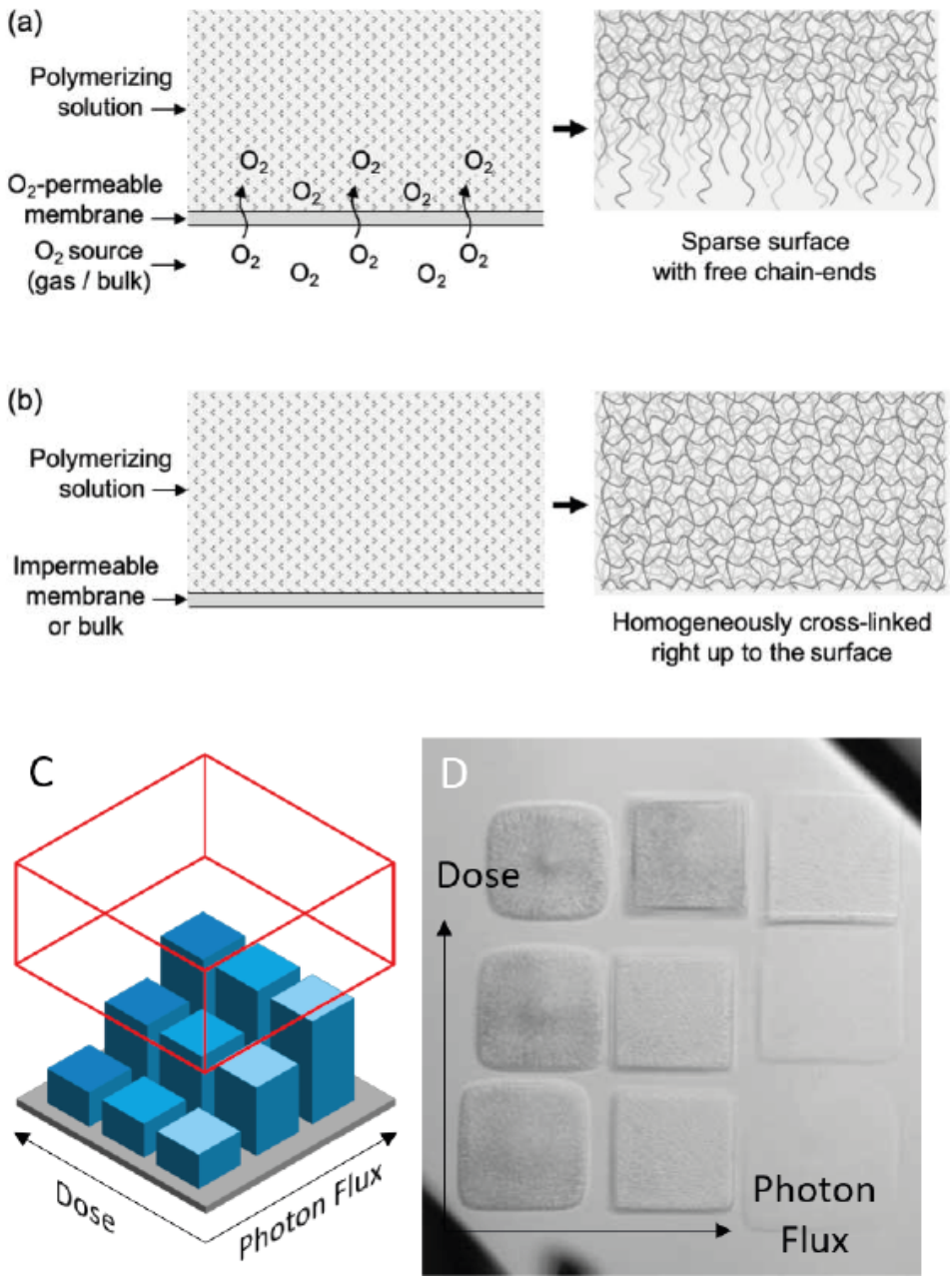

Figure 2.8: The principle of oxygen inhibition and its effect on hydrogel chains. a) Oxygen can diffuse into the polymerization solution through an O_2-permeable membrane and react with the free radicals. This creates a gradient of oxygens from the top to the bottom of the chamber. b) By inhibiting oxygen using a non-permeable boundary, free radicals polymerize the mixture solution in the presence of O_2 which results in inhomogeneously cross-linked structures [106]. C-D) The effect of photon flux and doses on the thickness of polymerization in the presence of O_2 [107].

2.5.4 Photoinitiators

Besides the macromolecular monomers (e.g., PEG) and the source of initiation (e.g., UV light), photoinitiators are required to initiate and propagate the reaction upon UV exposure. When choosing a suitable photoinitiator some features should be taken into consideration, including the efficiency of polymerization rate, water solubility, stability, absorption spectrum, molar absorptivity, and efficiency in generating free radicals, while avoiding potential cytotoxicity due to the free radicals. Currently, there exist two main categories of photoinitiators used in biomedical communities: radical and cationic. Due to their superior biocompatibility, radical photoinitiators are most used in tissue engineering applications[103]. Based on the mechanism of the free radical generation, radical photoinitiators can be further divided into type I: photo-cleavable (e.g., benzoin and acetophenone derivatives) or types II: biomolecular (e.g., camphorquinone, thioxanthone, and benzophenone). When exposed to light, type I photoinitiators absorb incident photons and decay into two primary radicals that trigger the crosslinking reactions, whereas type II photoinitiators extract the hydrogen from a co-initiator to generate secondary radicals for crosslinking process[108]. The main concern in the photopolymerization process is the presence of free radicals that may cause negative effects on living matters, especially in applications of hydrogels for grafting or injection. The cytotoxic effects of several photoinitiators strongly depend on the photoinitiator type and concentration, exposure time, and light intensity[109].

2.6 Research Gap

In the section 2.4.2, the most common technique to form neuronal spheroids is to use hydrogel arrays[9] [58] [75] [76]. This model offers simple yet *in vivo*-like structures that have been shown to represent the cellular organization and synaptic transmission[9]. Therefore, spheroids can be models for further study of synaptic events, namely contacts, remodeling, and plasticity. However, observing these activity-dependent events at the level of neuronal contacts is hampered due to the size and thickness of the spheroids. This is because of the scattering properties of light as it travels through thick live specimens and loses its intensity by a factor of $1/e$. This translates into a typical scattering lengths in the brain for visible and Near Infrared (NIR) light are in the 25–100 μm[110] and 100–200 μm[111] [112], respectively. To monitor neuronal contacts at synaptic levels, an ideal model must be amenable for optical microscopy in 3D (not larger than 200 μm) while it recapitulates *in vivo* -like structure, architecture, and function. The current hydrogel templates only allow forming spheroids of size above light penetration ability due to the limitation they face for fabricating smaller micro molds. Moreover, the fabrication of hydrogel arrays using micro molding is long (>24h), multistep, and requires expensive pieces of equipment and access to the cleanroom (**Figure 2.5**). Here we propose a hydrogel template platform[107] that allows fast and versatile fabrication of hydrogel templates with control height, shape, and size (50-100 μm) to generate neuronal spheroid and microtissues from rat Primary neurons.

2.7 Our Approach

In this work, we use 4-arm Poly(ethyl)glycol acrylate or 4-arm-PEGA (PEGTA) which is a hydrophilic polymer and in the polymerized state can hold high water

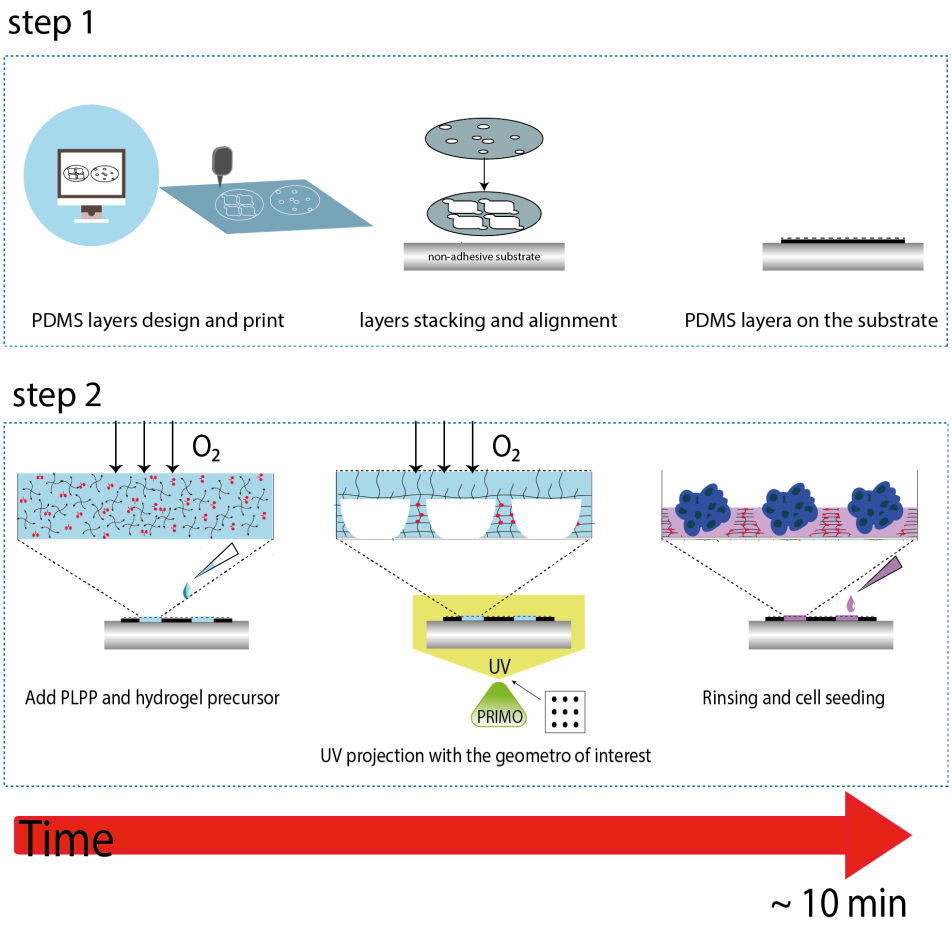

Figure 2.9: Hydrogel templates fabrication process using PRIMO system with two steps of 1) print and design of PDMS slabs and stacking them on the culture substrate. 2) Adding the reactive mixture of PEGTA and PLPP into the PDMS microareas followed by UV illumination with the geometry of interest, rinsing and cell seeding.

content. 4-arm-PEGA is biocompatible and naturally resistant to protein adsorption and therefore, does not support cell adhesion. Plus, the polymer length leads to a soft yet structured hydrogel. This macromer with reactive chain ends of acrylate allows free radical initiates chain photopolymerization in the presence of a photoinitiator molecule. We use 4-benzoyl benzoyl-trimethylammonium chloride or PLPP (Alveole, Paris) as a UV-sensitive photoinitiator to trigger the crosslinking and formation of the radicals. As mentioned, in radical photopolymerization, oxygen inhibits the polymerization which entails a large amount of a photoinitiator, and high UV intensity is needed to overcome the depletion of radicals by oxygen supplied from the air. We used this limitation in our favor to create oxygen gradients and by tuning the power of UV light we can control the thickness of the gels. **Figure 2.8** illustrates the diffusion of the oxygen through the mixed solution of photoinitiator and pre-polymer in the interfacial area containing large amounts of molecular oxygen when equilibrated with ambient air. Oxygen then reacts with free radicals generated from UV- photoinitiator interactions, resulting in a sparser surface with free chain-ends. Here we use a PDMS micro-area with small channels that create an oxygen gradient from the substrate (bottom) to the PDMS ceiling slap (top) and control the amount of oxygen reaching the reaction mixture. Tuning the laser power leads to a height control hydrogel system. Another feature of this hydrogel system is the intensity gradient of UV light over the course of illumination. In the PRIMO (Alveole, Paris) UV-projector system, Digital Micromirror Device (DMD) allows modulating light reaching the reaction mixture by the time length of the illumination on each micromirror which adds a dynamic effect to the photopolymerization process. DMD is a light modulator containing millions of mirrors. Each mirror in DMD has a reflective surface that steers the light by electrostatically switching each mirror between a binary state up to thousands of times per second. Upon illumination, each mirror either will reflect light towards the optical path, displaying white pixels, or deflect light from the optical path and display black pixels. Grayscale

shades are determined by the length of time that each mirror steer light during each frame. In this way, the light intensity is modulated for the initiation of the crosslinking process and one can tune the crosslinking with grayscale shades in illumination by projecting a pattern of interest onto the DMD (**Figure 2.11**). To form hydrogel via UV exposure, the mixed PLPP and PEG pre-polymers are prepared. Upon absorption of a photon, PLPP undergoes photoreactions and generates radicals on a polymer chain. The recombination of radicals and subsequent production of carbon-carbon bonds between the polymer chains cause crosslinking. simultaneously oxygen molecules diffuse through the PDMS micro-area and inhibit the reactions to their fullest potential by depleting the radical. Subsequently, the unreacted polymer is washed out upon completion of the crosslinking process (**Figure 2.9C-D**) and the hydrogel template is ready for cell seeding.

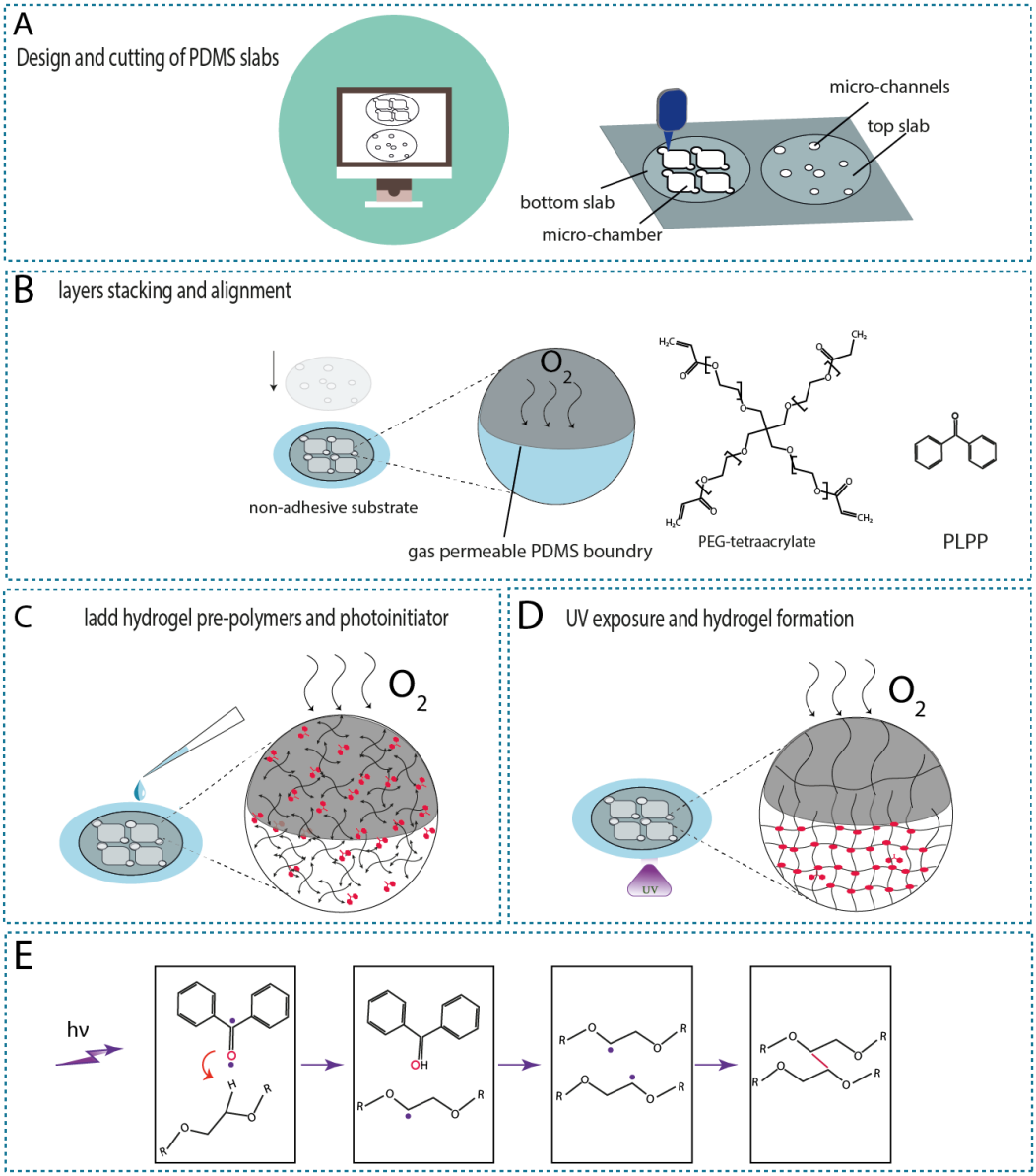

Figure 2.10: Fabrication of hydrogel template using maskless UV projector, PRIMO system. A) Designing and cutting PDMS films by xurography. B) Stacking PDMS slabs on a non-adhesive substrate in a way that the bottom slab contains micro squares that are covered by a top slab with two channels. C) Upon adding the PEGTA and PLPP, the oxygen reaction starts from the gas-permeable PDMS top slab. D) Upon UV exposure, free radicals are produced and start the chain-growth photopolymerization. E) UV light initiates the hydrogen abstraction in the PLPP photoinitiator which follows by forming free radicals and forming crosslinked networks.

2.7.1 Fabrication of Hydrogel Templates

Figure 2.11 and 2.10 schematically present the UV projector (PRIMO system) and the protocol to fabricate hydrogel microscale templates. PRIMO system includes the following components: an ultraviolet laser, DMD or digital micromirror devices which serve as a light modulator, a beam expander, a 4f system (**Figure 2.11**). In this protocol, we benefit from UV-sensitive material to trigger the photopolymerization process. As demonstrated in **Figure 2.10**, two PDMS layers are designed and cut by xurography. The bottom layer has 4 square- shape microwells each 0.5 cm in size (they can be up to nine microwells for an antifouling IBIDI dish; the non-adhesive area is around 2 mm) and the top layer is designed in a way that covers the microwells but leaves two holes at one diagonal of each microwell This prevents the oxygen reacts with the photoinitiator. The mix solution of the photocrosslinker and 4 hydrogel pre-polymers (5%) is added to each PDMS micro-area. A pattern with geometries of interest and a size of 1824x1140 is created and loaded into Leonardo software. In the software the intensity. To fabricate hydrogel templates the maximum laser power of 128 mw/cm^2 and illumination time of the 90s is being used unless it's mentioned otherwise. Alternatively, the DMD allows using gradients in the projected pattern. This means that the intensity of the illumination can be tuned by changing gray values in the grayscale patterns.

The hydrogel precursor is a mix of 5% of 4-arm-PEG-acrylate solved in 1X of PLPP photoinitiator. The solution is then added to the PDMS slab on a bioinert culture plate (IBIDI). The dish is placed at the stage of a converted microscope incorporated with the Primo system. A 100% UV light power for 60 seconds is shone. This step is repeated for each PDMS micro area, where the hydrogel precursor is added. The plate is rinsed with water 3X followed by rinsing with 70% Ethanol. Then the culture plate is incubated with a culture medium at 37 C and 5%CO_2 for at least 30 minutes before seeding cells.

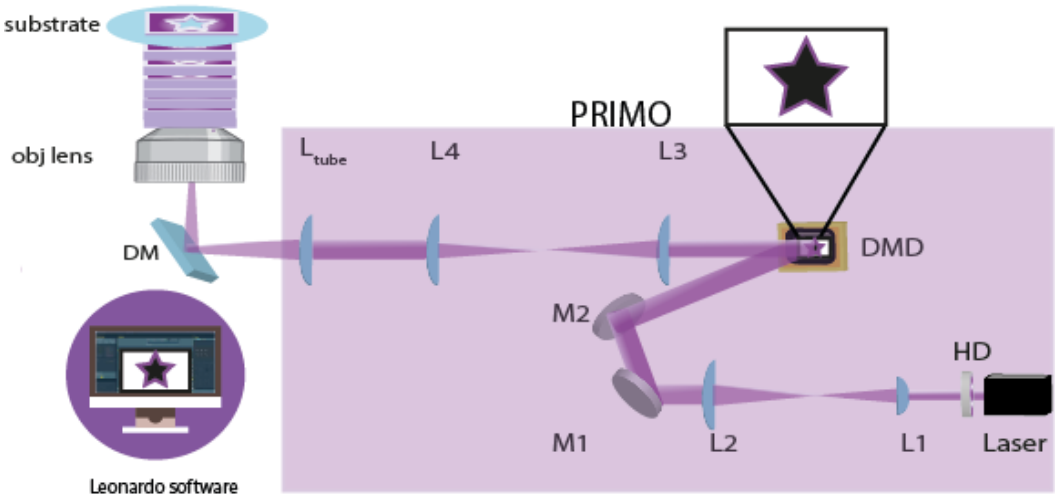

Figure 2.11: PRIMO system consists of a UV laser, holographic diffuser (HD), a DMD, a beam expander, and a 4f system. This system can be combined with any epifluorescence microscopes and project any patterns onto the sample using UV light. Leonardo software allows projecting patterns with control over the position, duration, and intensity of UV.

2.7.2 Cell Culture and Spheroid Formation

To generate neuronal spheroids, hydrogel templates are prepared as explained in 2.7. After incubating the micro areas with a culture medium, with a 1000 μl pipette, the medium from each PDMS micro-area is removed and the dissociated neurons are added into each PDMS micro-square (15 μl/square). **Figure 2.12** demonstrates a culture plate with 4 PDMS micro areas. The plate has antifouling properties that prevent cell adhesion on the bottom of the dish.

Immediately after seeding, neurons are floating in the micro-area after 2 hours that neurons settle into the recesses and the non-dropped cells on the surface of the hydrogel are washed out. Note that due to the intrinsic inertness of PEG, the cell would not adhere to the gels. The neurons then form aggregation after 24 hours. Using hydrogel arrays with sizes from 50 to 100 μm, we can generate neuronal spheroids and maintain them for 3 weeks. These spheroids are generated from hippocampal and cortical E18 rat primary neurons. Upon seeding, cells fall

into wells and after 2 hours they create aggregations. For the microscopy imaging, the size and thickness of the spheroids in these experiments do not exceed 100 μm. This size allows the spheroids to be compatible with light penetration and optical imaging ability to image in-depth, (the next chapter will present more detail on this). After preparation of the hydrogel arrays, they are incubated with a culture medium ($NB^+ + B27^+$) for 1 hour. Then cells are seeded at the density of around 50K per microwell. **Figure 2.13** shows neuronal spheroids' growth in arrays of various shapes and sizes.

As discussed previously, PEG hydrogels are antifouling materials. This is beneficial for spheroid cultures as the aggregation of the cells does not adhere to the gel. **Figure 2.12-A, B** shows that the floating cells on the gels are washed away after filling the culture plates with the medium. Moreover, PEG hydrogel comes with a variety of polymer length that allows us to tune hydrogel features to meet our criteria. Pasturel and colleagues have shown that pre-polymer length can affect the stiffness and degrading features of hydrogels[107] and PEGTA with a molecular weight of 10K can maintain the 3D networks of hydrogels rather than brittle structures while being soft enough to accommodate physiological conditions for cell cultures.

Different shapes of the arrays allow us to optimize the size of spheroids. For the microscopy imaging, the size and thickness of the spheroids in these experiments are at maximum of 100 μm (**Figure 2.13**)

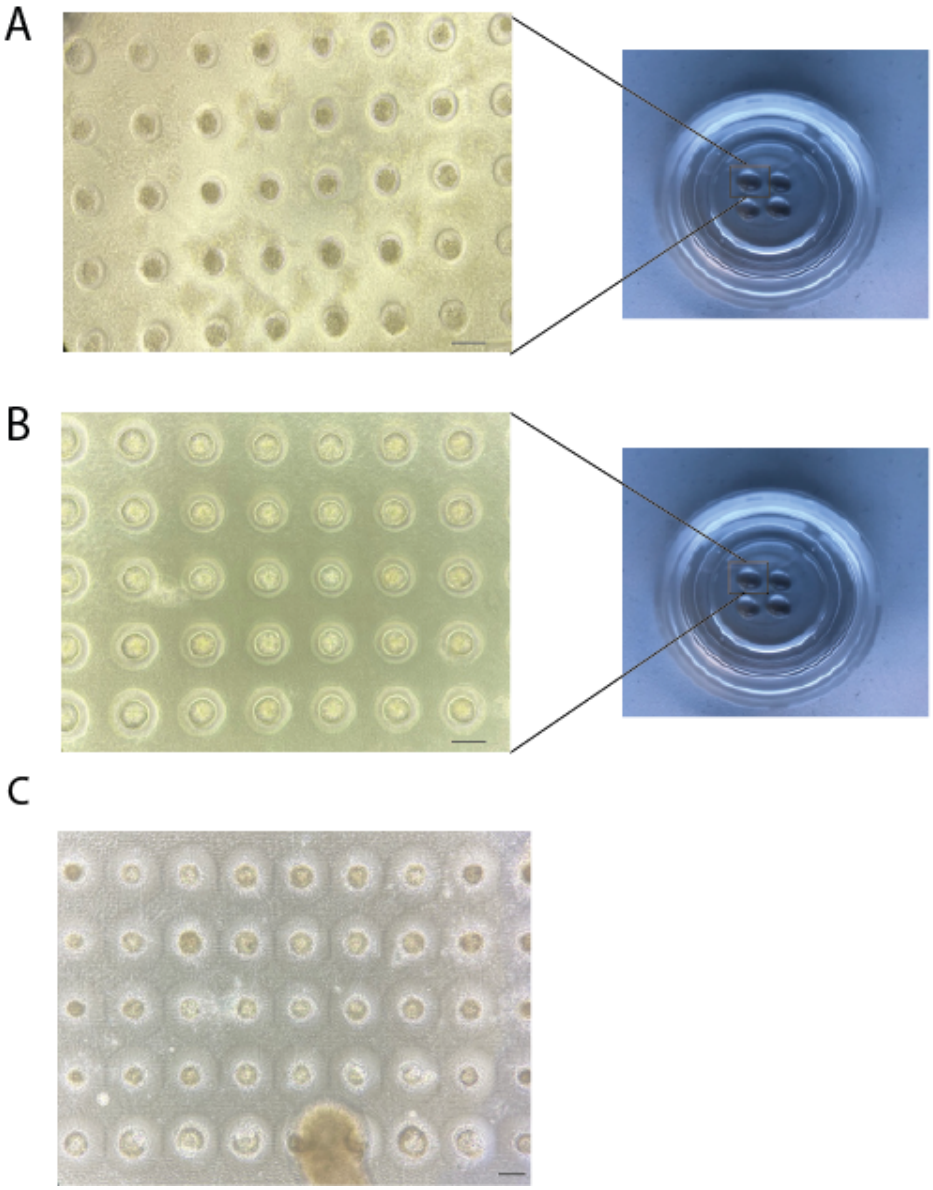

Figure 2.12: Spheroids generated from rat primary cortical neurons. Arrays cellular aggregations A) after seeding cells, B) 2 hours after seeding. C) Spheroids after 7 days in vitro. The floated aggregation in the medium attached to the wells. Scale bar is 70 μm.

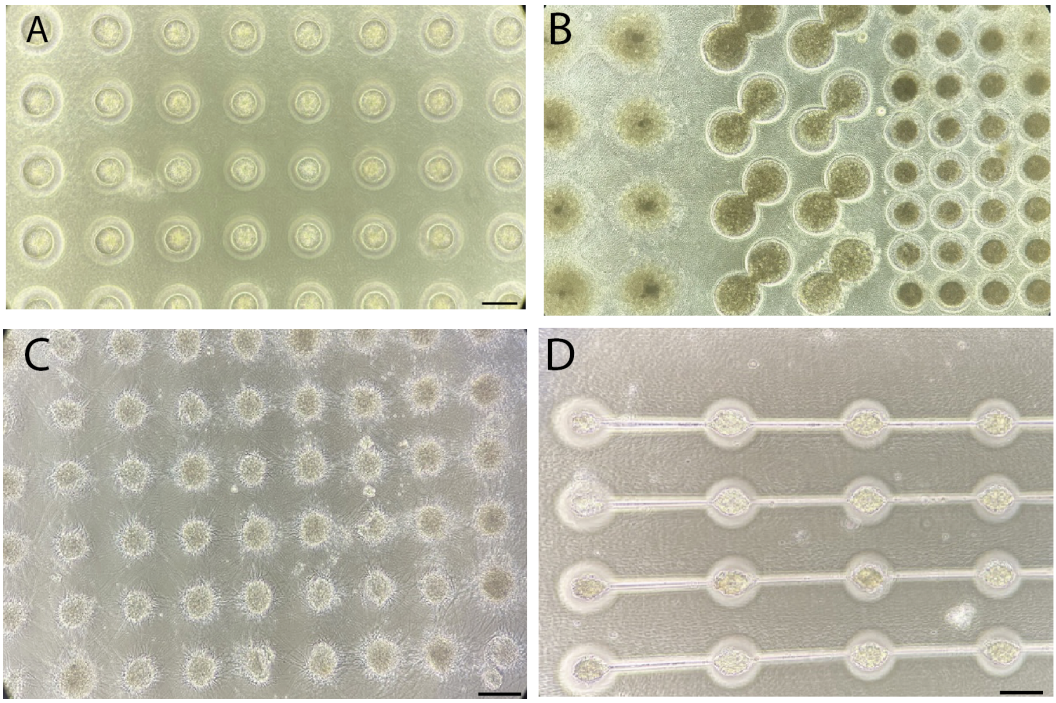

Figure 2.13: Hydrogel templates highlighting the ability of the PRIMO system to fabricate micro structure of different sizes and shapes. A) round-shape, B) small-size gradient round-shape , C) channeled round-shape, D) big-size round gradient, E) mix of eight-shape and round shape. Scale bar is 70 μm

2.7.3 Spheroids Characterization

To characterize the spheroids immunohistochemistry assay is performed to identify neuronal subtypes and how they grow in culture. For that, the concentration of the cell's solution should be high enough to create a final cell density of 10K per PDMS micro area after filling the plate with a culture medium.

Neurospheres (**Figure 2.14**) generated in the hydrogel templates (shown with dashes circles) are mixed cultures of progenitors, neuronal and glial cells followed

by filaments and processes only after 3 DIV (Figure 2.14) consistent with work from Dingle et al. Lamin labeling of nucleus shows that the diameters of the spheroids in the same PDMS micro-area may differ **Figure 2.14-C arrows** which is due to the randomness of the cells falling into each well. This effect can be seen less when a high cell concentration of cells is plated initially. However, plating cells with high concentrations may create unwanted aggregation above the wells which can aggregate with spheroids inside the wells. Then by adding the culture medium to fill the dish, cell aggregation together with spheroids break or detach from the wells and leave the wells empty.

Labeling spheroids with anti-nestin, anti-beta tubulin, and anti-MAP has shown diverse cell types in the spheroids. Nestin, a type VI intermediate filament protein, is a routine marker for neural progenitor cells. Anti-nestin label revealed that the progenitor cells grow in number and length of neurofilaments from 3 DIV to 7 DIV.[9]. As explained in the section 2.5, stiffness of the hydrogel materials depends on many parameters such as (e.g., the concentration of pre-polymer, length of chain). In our approach, using the PRIMO system, we are able to work around the stiffness of PEG pre-polymers by tuning the light intensity and exposure time. **Figure 2.14-D** shows processes of the spheroids have extended on the top of the gels, whereas in **Figure 2.14-C** the neuronal processes did not exceed the area of the well due to the higher stiffness. However, the neuronal network processes would eventually cover the top of gels when kept longer than 14 days *in vitro*. The result shows the effect of illumination intensity on the stiffness of the gel and therefore the growth of neurofilaments on the PEG gels. As the illumination dose affects hydrogel pore size[107], thus the stiffness, neurofilaments migrate onto the soft gel (Figure 2.14-C). whereas the templates created with full power illumination mode and stiffer gel show no growth on the gel. Depth color-coded images also reveal (**Figure 2.16**) the architecture of the neuronal processes inside the hydrogel wells. The hydrogel-based templates fabricated by a gradient pattern manifest a cup-nest shape

for randomly packed filaments. This highlights the effect of stiffness on neuronal migration and neurite outgrowth[35] [34]. Patterns with a gradient can be associated with the illumination of different doses. As explained in 2.7, the DMD can create grayscale shades by the length of time that each mirror steer light during each frame. This leads to hydrogel polymerization of different stiffness.

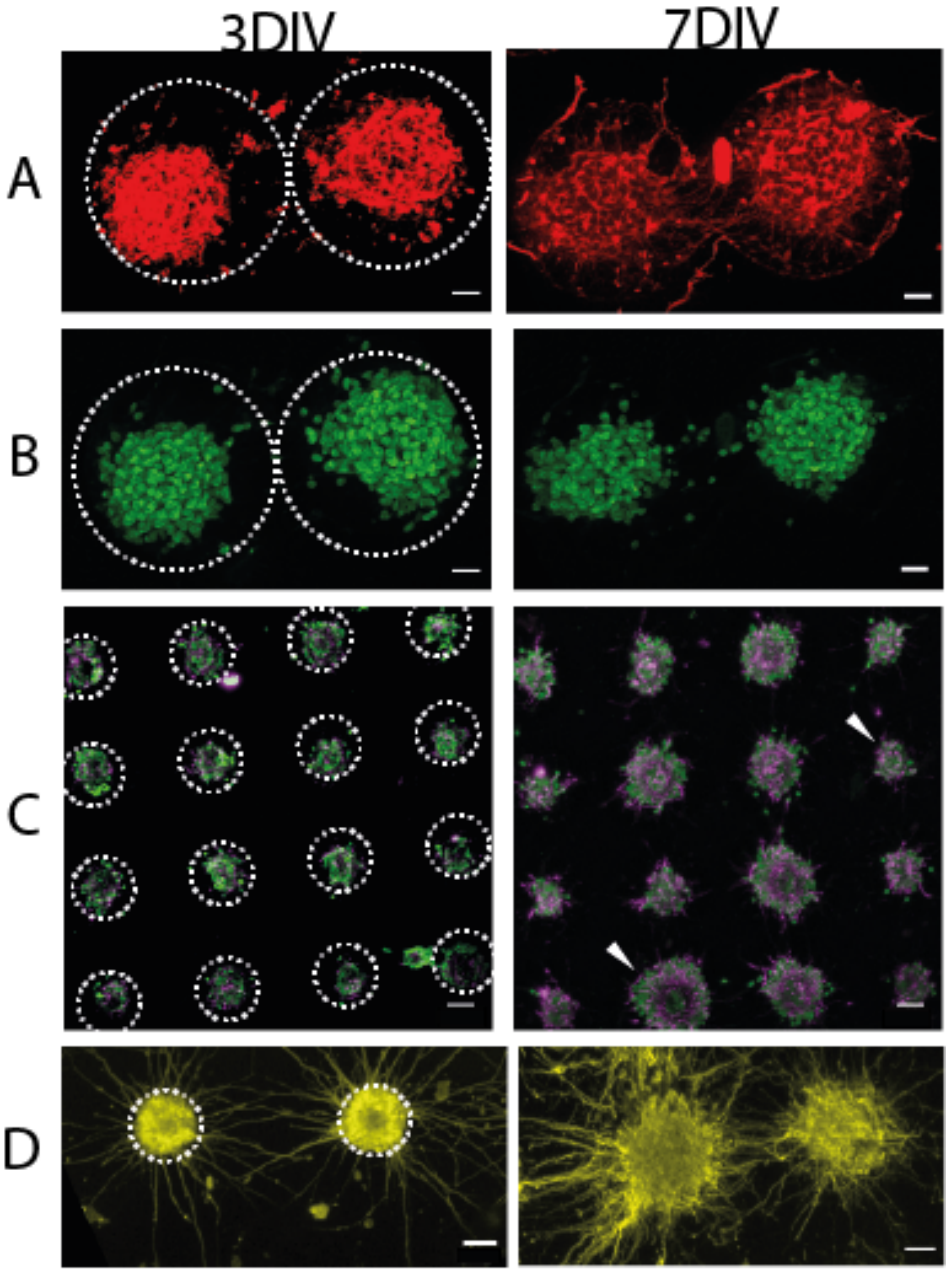

Figure 2.14: Immunohistochemistry labeling of spheroids in hydrogel templates in Left panel (3 days in vitro) right panels (7 days in vitro) dashed circles the size of the wells. A) beta-III Tubulin, TUBB3, (red) is a microtubule protein on beta chains specialized in neurons. The immunolabeling highlights the high population of neurons in spheroids. B) Lamin (green)is an intermediate type of filament at the nucleoplasm site of the nuclear membrane. Neuronal processes are grown inside the well because of the high stiffness of the gel. C) Nestin (magenta) is an intermediate filament-associated protein and contributes to the cytoskeleton. Expression of nestin in spheroids showed the presence of neuronal progenitor cells and their increase in population up to day 7 and growth in the length of neuronal processes. D) MAP2 (yellow) microtubule-associated protein 2 in all cells. MAP2 (yellow) microtubule-associated protein 2 all cells. The soft gel allows neuronal extension on the top gels. scale bar A-B = 20 μm, C-D = 50 μm. Max projection z-stack of A-B) a Spectral image scanning microscope and C-D) a confocal Microscope

2.7.4 Spines and Synaptic Contacts

For live-cell imaging, we use fluorescent protein tools to stain cells with distinctive colors. As we presented in the previous sections, immunostaining of spheroids shows the labeling of all cells within the spheroids. As discussed, sparse labeling not only provides a more accurate architecture of neurons that are selectively visualized but also offers images with higher SNR, as there are only a few neurons labeled in the spheroids.

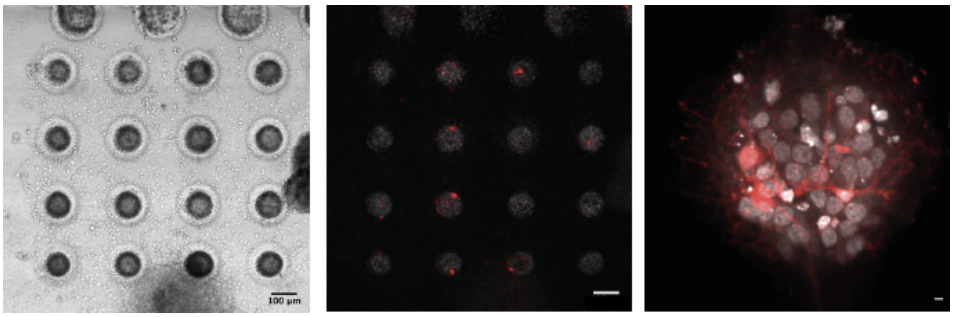

Figure 2.15: Sparse labeling in spheroids using electroporation technique. max projection of 3D confocal stacks after 14 DIV spheroids expressing GFP (in red) are fixed and stained with DAPI in gray. Only few neurons are labeled to facilitate visualization at the level of single cells.

Using electroporation technique (protocol in Appendix1) rat primary hippocampal neurons were transfected with GFP at 0 DIV. Then the transfected neurons are mixed with non-transfected cortical neurons (1:9) to perform sparser labeling. The FP starts to express 24 hours after transfection, and it is ready for chemical fixation or/and live-cell imaging. **Figure 2.15** presents the GFP expression of neurons in hydrogel wells.

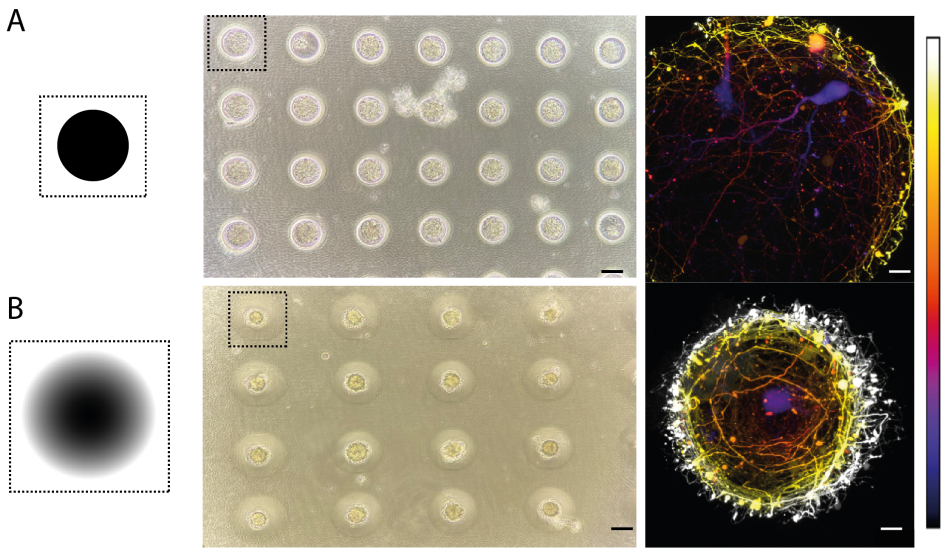

Figure 2.16: The effect of the gradient of patterns on the architecture of neurons in the hydrogel wells. Max projection confocal z-stack of neurons expressing GFP have extended their processes shown with the depth color code. The fabrication of the hydrogel wells has been done with full intensity power of the UV light for 90 seconds A) without and B) with gradient patterns. The DMD in the illumination path of the PRIMO system creates gray shades and modulates UV intensity by changing the duration of steering time. This change in illumination dose affects the crosslinking process, thus the stiffness of the gel. fluorescent images scale bar 10 μm, bright-field images 70 μm after 7 days in vitro

To obtain dense, mature neuronal networks *in vitro*, usually 10-14 DIV culture is required[113]. we, therefore, fixed the spheroids after 14 DIV. A series of maximum intensity projections of a confocal stack is shown in **Figure 2.15** at 5 different planes (each MIP contains 33 planes) with dendritic spines nicely visible in each plane. The image shows the spine organization and density for one single neuron. The 3D organization of the dendrites allows us to visualize them in a different plane and choose the plane of interest in the 3D stack for further image processing.

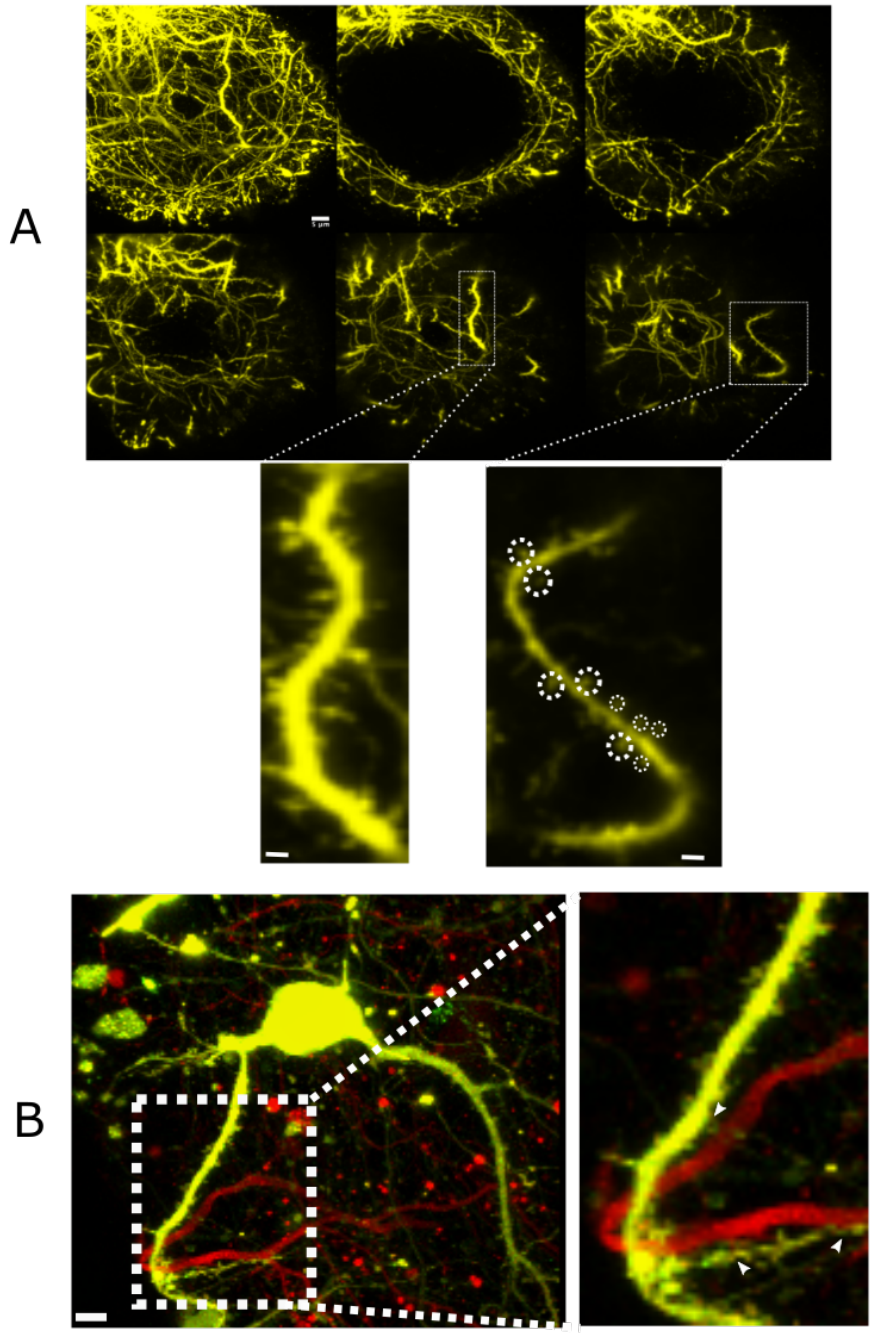

Figure 2.17: Dendritic spines and synaptic contacts of neurons within spheroids after 14 days in vitro. A) Max projection of 3D confocal stacks of a single neurons inside a spheroid expressing Tdtomato (FP 563nm) presenting dendritic spines after 14 DIV dashed circles highlights the dendritic spines in the last plane of the 3D stack. B) two neurons expressing tdtomamto (in red) and GFP (in yellow). Scale bars = 5 μm

2.8 Conclusion

We developed PEG hydrogel templates to generate uniform-sized multicellular neuronal spheroids (**Figure 2.12**). Using PRIMO UV-projection system, prepolymer (PEG tetra acrylate), and PLPP photoinitiator, we can fabricate hydrogel templates of different sizes, shapes, and thicknesses to form and grow multicellular neuronal spheroids (**Figure 2.13**). For the sake of optical microscopy, hydrogel-based arrays with diameters of 70 and 100 μm have been fabricated for this purpose. After 24 hours of plating neurons in the hydrogel templates, neuronal aggregations started to self-assemble and form spheroids. These spheroids are small yet with the capability to form synapses and connectivity after 14 days in a *in vivo*-like stiffness. This model allows further investigations and more importantly time-lapse measurements of network assembly within neuronal spheroids.

The method we described offers several advantages. It uses a common hydrogel PEG that is well-established and characterized for its biomechanical properties. The fabrication of hydrogel templates is versatile, straightforward, and is reproducible in spheroid size and cellular composition. Specifically, this approach does not require multistep lithography and micro molding and generates hundreds of microwells in only a few minutes and thus showing its potential for throughput assays. Because the spheroids are smaller than in reported studies, they are less likely to show a necrotic effect and can be maintained for 21-28 days. projecting different geometries and the gray shades into the PRIMO system, allows us to tune the hydrogel's softness and crosslinking networks. This feature allows the spheroids to rapidly fuse over the gel and create connections in softer gels.

Chapter 3

Imaging Synaptic Contacts

In this chapter, we will present the challenge of imaging 3D *in vitro* models of neuronal connections using optical microscopy and the current state of the art to perform 3D multicolor long-term imaging of these connections in real-time. It follows our imaging approach that provides efficient optical sectioning, with high spatio-temporal resolution and the result from a combination of a dedicated *in vitro* model with an original imaging technique.

3.1 Seeing in 3D, live, and multicolor

Light microscopy has long been a tool to investigate and study the structure and dynamics of matter or living systems. The first observations of the nervous system date back to the 1900s, when the light microscope was used together with Golgi's sparse staining of cell populations. This observation of cells in their whole has laid the foundation of histology and anatomy of the CNS, opening a new era in neuroscience. Besides the traditional imaging techniques in neuroscience (e.g., electroencephalography, magnetoencephalography, etc.,), optical imaging in combination with genetic tools and computational techniques brings advantages that make them appealing to neuroscientists. The major capability of optical imaging in the nervous system is the scale of imaging from the synapses to whole-brain imaging while achieving high spatial and temporal resolution. Moreover, they are

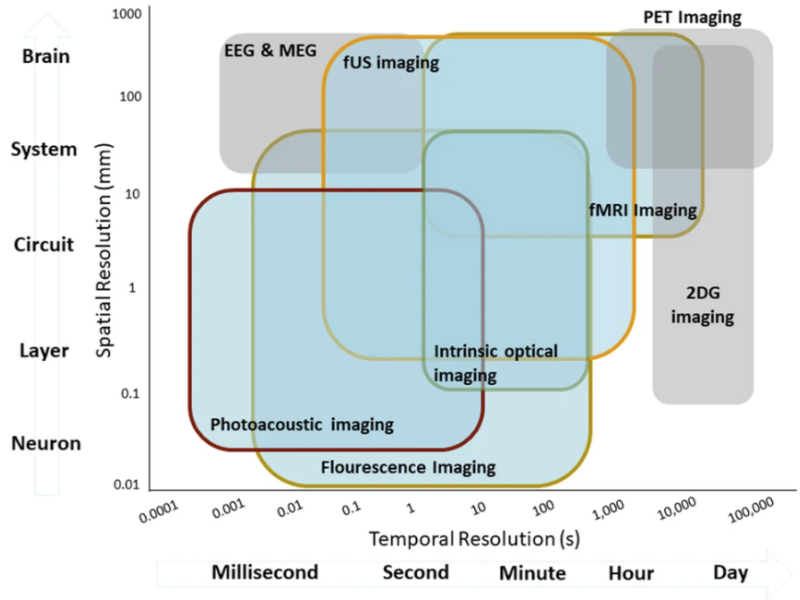

Figure 3.1: Different imaging techniques from single cells to whole brain imaging based on their temporal and spatial resolution (EEG electroencephalography, MEG magnetoencephalography, PET positron emission tomography, 2-DG 2-deoxyglucose, fUS functional ultrasound, fMRI functional magnetic resonance imaging) from [114].

flexible and compatible with necessary modifications to adapt to specific conditions or specimens. For instance, one can selectively label different neurons and follow their activities. But native nervous tissues hardly are compatible with optical imaging owing to their opacity and scattering properties of invisible lights. Besides, most living cells are sensitive to light due to the protective mechanism against photodamage. Therefore, microscopy observations of the nervous system have often been performed on chemically fixed specimens with improved optical transparency of brain tissue (e.g., tissue clearing). In turn, light imaging of living neuronal tissue is challenging but at the same time opens doors to developing and designing new optical instruments in order to circumvent intrinsic limitations. Combining optical microscopy with the development of Fluorescent Protein (FP) toolbox[115] has paved the way to observe the cellular structure of interest in living cells in real-time. Fluorescence, the absorption of a photon, and subsequent emission of a photon of lower energy, combined with optical microscopy techniques, lead the way for biologists to map specific cellular compartments with high contrast in live specimens. Engineering FP expression in neurons has vastly improved our understanding of cellular organizations and functions of the nervous system. Yet, capturing the dynamic events of synaptic remodeling (retraction, enlarging, shrinking, and elimination) and their contacts are technically difficult for several reasons. Indeed, the connectivity between neurons is complex and distinguishing prep- and post-synaptic neurons and their contact are sometimes impossible. Synapse synapses are small 3D structures with sizes varying from 0.5 to a few micrometers[116], thus a conventional microscope cannot resolve 3D synaptic connections. In addition, time-lapse imaging entails reducing photodamage to maintain cell viability with a temporal resolution of a few minutes to capture synaptic remodeling and interconnections[117]. Besides these already existing challenges in imaging neuronal contacts, new obstacles arise when imaging 3D structures in real-time with multiple fluorescent colors. For instance, the optical sectioning ability of the system plays a critical role in generating

3D imaging with a high signal-to-noise ratio. These criteria in optical microscopy are interrelated, therefore, a compromise exists between them depending on the application. A trade-off between spatial resolution, phototoxicity, photobleaching, and acquisition speed must be made. We now discuss these aspects and the trade-off between each to achieve 3D live-cell imaging and the established techniques to visualize the dynamics of synaptic contacts.

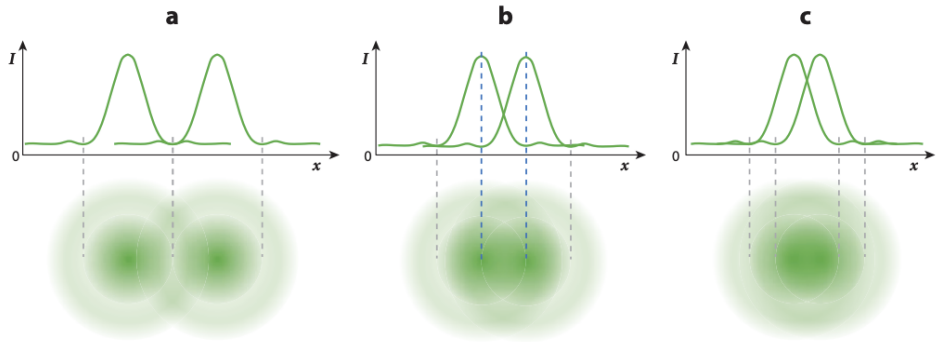

Figure 3.2: Rayleigh criterion for assessing spatial resolution in an optical system. Airy discs from two neighboring point sources and their corresponding intensity profile. a) Two points are distanced larger than the resolution limit and therefore they are resolved by the optical system. b) The points are fairly distanced with the separation radius of an airy pattern that represents the resolution limit. c) The distance between the two points sources is smaller than the resolution limit and therefore they are resolved by the optical system. Adopted from [118].

3.1.1 Spatial Resolution

The resolution of an optical microscope is fundamentally limited by the diffraction of light. The light from the sample spreads out and impacts the ability of our system to resolve and differentiate fine details in the specimen. This resolution limit was initially recognized by Ernst Abbe and indicated that the diffraction-limit image resolution of objective lenses with high numerical aperture is app. 250 nm and 500 nm for lateral and axial resolution, respectively. In essence, these numbers represent the minimum distance at which an optical microscope can distinguish between two or more point objects[119]. When light is emitted from a point object, the objec-

tive lens collects and focuses the light at a point on the image plane. In an ideal optical system, the focus point is infinitely small. Practically, however, it produces a diffraction pattern of concentric rings in the lateral plane known as an airy disk. Point Spread Function (PSF) is the three-dimensional intensity distribution of the point object. The resolution of a focusing light microscope can be assessed by the Full-Width Half Maximum of the focal spot or the PSF which is the characteristic of a microscope system and represents an image of a point source.

$$\Delta x, \Delta y = \frac{\lambda}{2n\sin(\alpha)}$$
$$\Delta z = \frac{2\lambda}{2n\sin^2(\alpha)}$$

where λ, n, and α denote the wavelength, the RI, and the aperture angle in the objective lens. As shown in the equation above, the lateral resolution of an objective lens is significantly better than its axial. This is because the light is more spread out when traveling in the axial direction. When a light wavefront is passing through the objective lens, only some portion of the spherical wave is collected by that lens. The Numerical Aperture (Numerical Aperture (NA)) of the objective lens determines the fragment of the spherical wavefront. Spine's size can vary from 0.5 to 4 micrometers (e.g. filopodial spines have longer shapes, see **figures 3.3**) and their structural geometry correlates with the strength of synaptic connections and may change over time. With regards to synapses and their morphological interactions, **Figures 3.3-A** demonstrates the projection of a confocal stack of morphological contacts between axonal boutons and dendritic spines. **Figures 3.3-B** represents a high-resolution image of 2D neuronal culture with resolved protrusions. This image highlights the fact that monitoring the dynamic of neuronal connection super-resolution is not the main concern but the optical sectioning ability of the system for generating high-quality images of 3D structures. **Figure 3.2** depicts the spatial resolution ability of conventional optical microscopes.

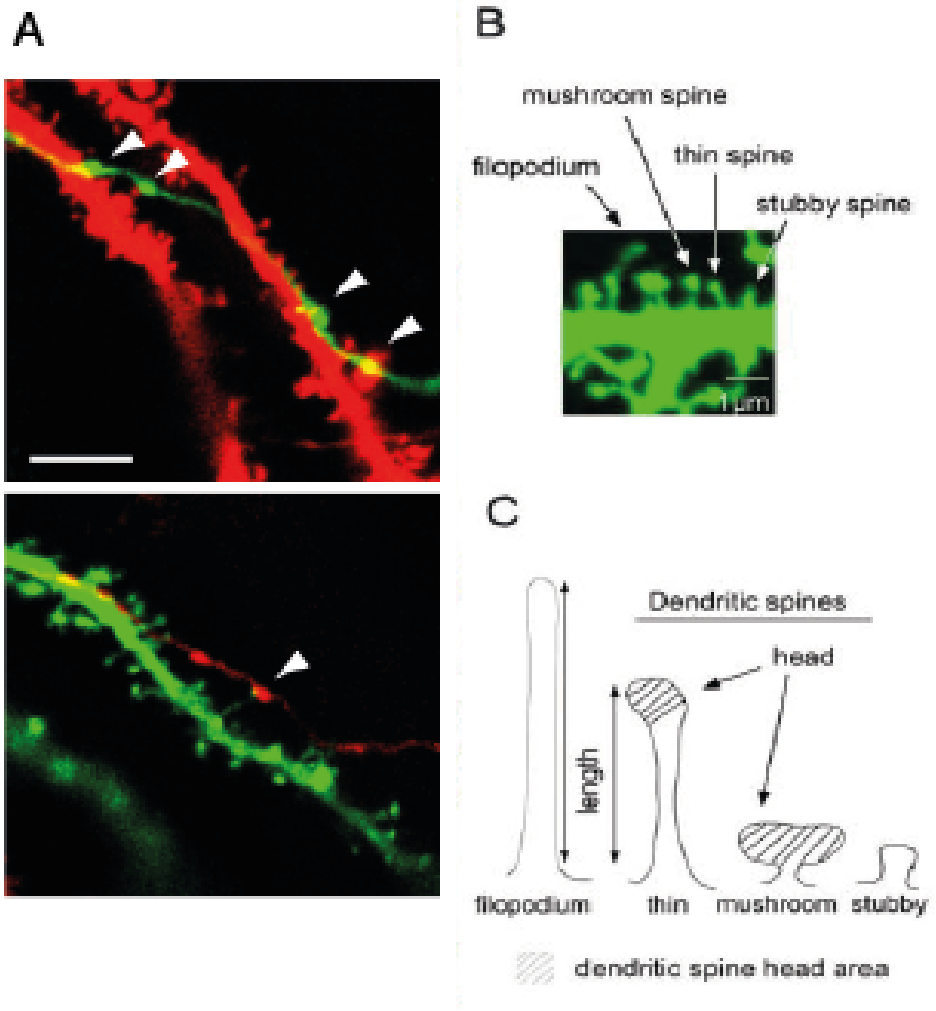

Figure 3.3: Spines sizes and types. A) A confocal stack image of two hippocampal neurons are expressing GFP (green) and tdtomato (red) in rat organotypic slice, showing the neuronal contacts at synaptic level, from[1]. B) Dendritic spines in cultured hippocampal neurons expressing GFP after 14 days. D) Schematic presentation of filopodia-like protrusions of dendritic spines and mature mushroom spines showing the largest heads and thin necks, from[120].

BOX 1

Signal to noise ratio refers to the ratio of fluorescence signal from a region of interest to the total noise (Noise). In order to perform quantitative imaging, it is crucial to have adequately high SNR. For any photon incident on the detector, the S/N ratio can be written as $QE\tau I_p/\sqrt{QE\tau I_p}$ with a photon flux of I_p, an exposure time of τ, and quantum efficiency of QE. In addition to the mentioned parameters, SNR depends on other factors such as sensor pixel size which determines how much signal one single pixel can collect.

Noise or sensitivity refers to random variation of the measured signal in measurement and can be defined as a form of signal-dependent uncertainty due to the nature of photons. In microscopy, noise originates from two main types of noise, amongst others. Photon noise is the inherent uncertainty in the measurement of light that makes the arrival of photons to the sensor a random process that can vary from frame to frame. The results of these noises would be images with less sharpness and crispness.

3.1.2 Optical Sectioning and Imaging in Depth

?? The light-tissue interaction is a complex process due to multi-component tissue structures with inhomogeneous optical properties. When light is incident on a cell, it may reflect at the cell interface, be absorbed, scattered multiple times, or refracted when light enters layers with different refraction indexes (RI). Living tissues contain cellular parts with different RI such as proteins, water, and lipids cause a mismatch between the cellular compartments as well as the interface of the specimen (e.g. glass) where the light enters[121] (**Figure 3.5**).

These effects can effectively worsen and undergo abrupt changes in thicker tissue due to light attenuation and cause blurring and contrast loss in microscopy images (**Figure 3.5**). As the excitation light spreads over the sample with a volume larger than a diffraction-limited spot, the intensity of the light becomes weaker to excite

the sample in depth. The fluorescent light emitted from fluorophores within the depth of the specimen is also scattered before reaching the objective such that it

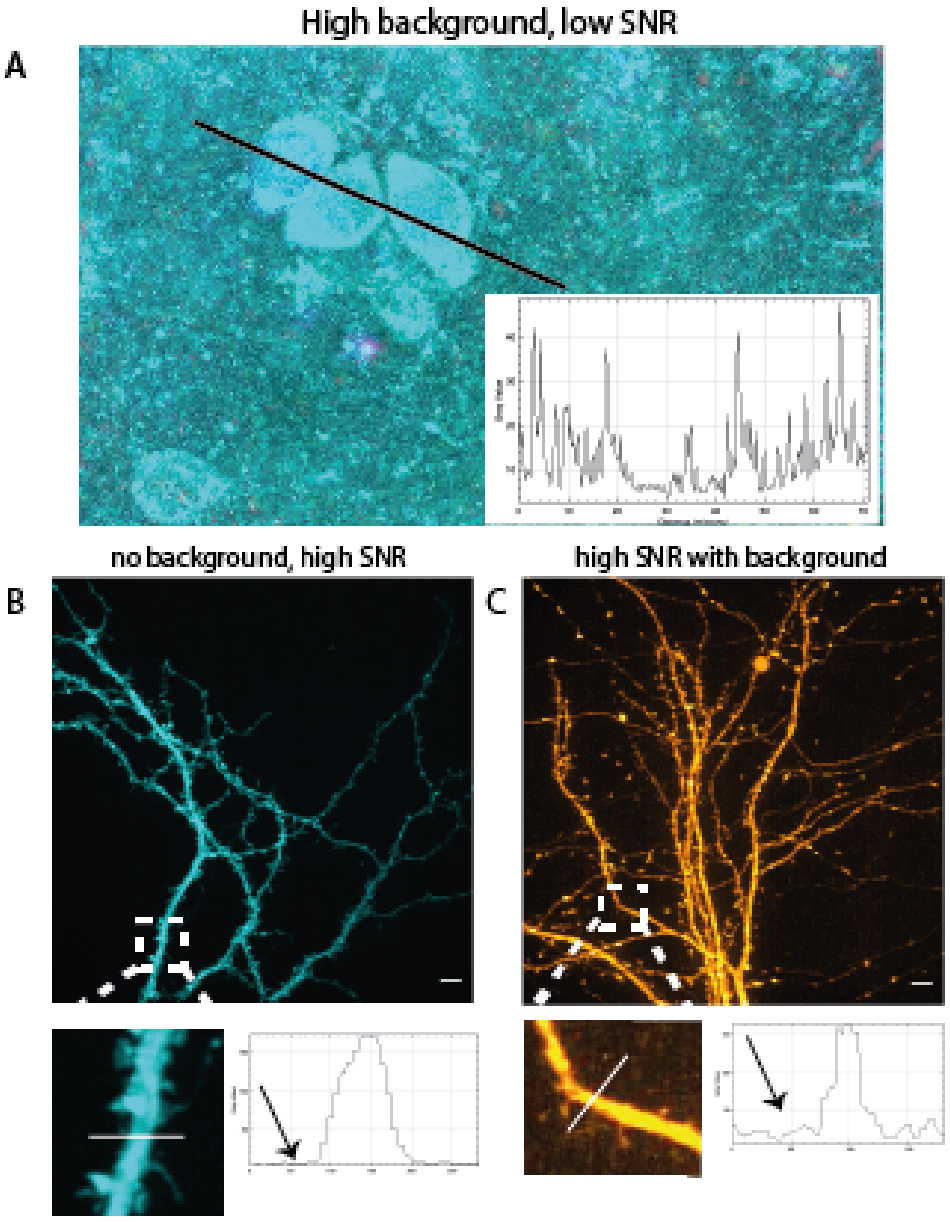

Figure 3.4: Signal to noise ratio and background. A) projection of a 3D stack with high background. B) projection of 2D culture images with B) low background, high SNR, and high contrast. C) acceptable SNR with background and lower contrast, still the signal in the area of interest is high enough to visualize the dendrite and spine.

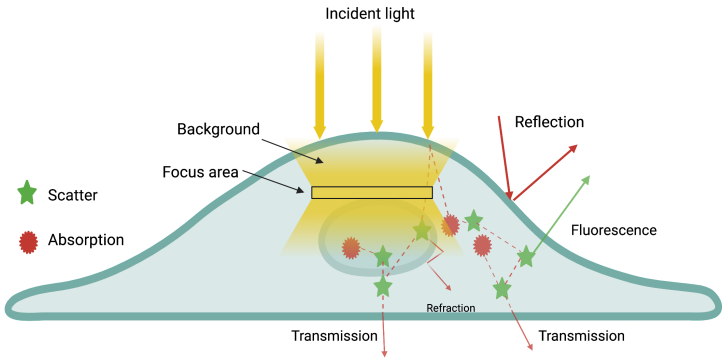

Figure 3.5: What happens when light incident live matters. Reflections on the tissue surface result in the change in direction of the light wave caused by a single interaction with a large object. Absorption is where the energy of the light is absorbed by the cells and then converted into a different form such as heat. Fluorescent results in the absorption of a photon and subsequent emission of a photon of lower energy. Light scatters when the incident light changes the direction of propagation due to different RI which limits the depth of light penetration. A small amount of light may be transmitted.

seems no longer from an in-focus point and becomes the out-of-focus light that deteriorates the quality of the image.

Optical sectioning is the ability of an optical microscope to remove the background caused by out-of-focus light from generated images. One main issue in fluorescence microscopes is that when the light excites the fluorophore in the specimen, emission light arises from each sample plane that produces intensity within a solid cone and causes the entire specimen to fluorescence (**Figure3.5**). This results in unwanted light out of the focal plane (out-of-focus) reaching the objective lens and reduces both the resolution and the contrast of the in-focus region by creating background noise.

For instance, for a 100X objective lens with an NA around 1.3, the depth of field is 300 nm. Therefore, the majority of the volume of a specimen is out of focus (thickness of cells is from 5 to 15 μm). For the sake of image quality and contrast, it is desired to collect light only from the thin section around the focal layer of the system. To do so, scientists have developed techniques that either physically (e.g., a pinhole

in confocal microscopy), intrinsically (2-photon excitation), or computationally (e.g. spatial filtering) avoid out-of-focus lights.

BOX 2

Light penetration in biological samples:

In biological samples penetration of light is limited to the scattering and absorption nature of light. The strength of scattering can be described by an average distance between scattering events, known as 'mean free path' l_s. For an object with comparable size concerning the wavelength of the light, scattering can be quantified by transport free path; l_t where g is the anisotropy parameter. l_t is essentially the 'memory direction' distance after which the direction of the light is changed. This is exactly the distance that limits light penetration in biological specimens. For brain gray matter this value yields a value of 50–100 μm at 630 nm in tissue and of about 200 μm at 800 nm in vivo[122]. This value increases with wavelength (i.e., NIF).

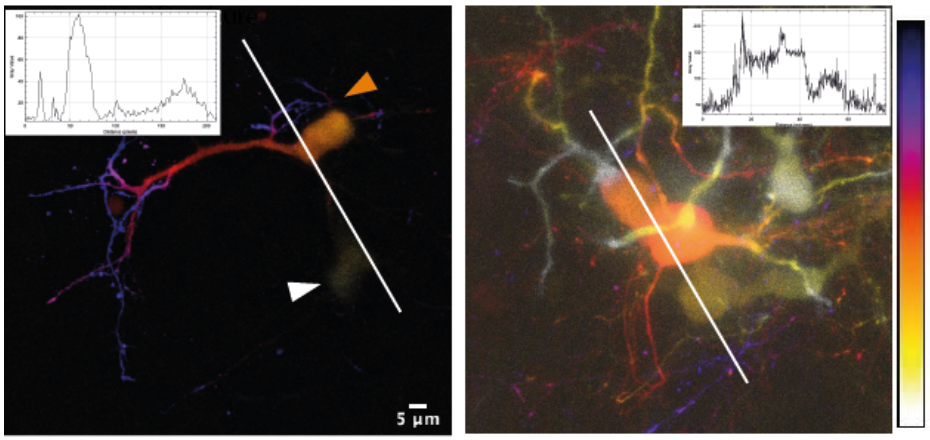

Figure 3.6: Projections of a 3D stack of transfected neurons in hydrogel wells with color-coded depth. Left) 50 μm thickness, arrowheads highlight the different SNR in two cells where light scattering diminished the fluorescent emission at the plane further from the specimen-objective plane. Right) More than one fluorescent neuron in a 100 μm spheroids.

In a linear system, fluorescence light is generated by a single photon process with

uniform (zero spatial frequency) illumination, such as in a conventional microscope. This system exhibits poor optical sectioning, but Non-uniform illumination methodology with non-zero spatial frequencies along with post-processing results in sharply in-focus optical sections[123]. In a nonlinear methodology, a molecule is arisen to the excited state by a two-photon pulsed laser, which leads to excitation only in the focal point and, therefore, intrinsically provides thin optical sections within tick specimens[124] [125].

To generate an in-depth image, a series of thin in-focus sections of the volume is taken as the specimen is axially moving through the focal region. Then this sequential data set is processed to build up a 3D visualization of the object. However, even without aberrations, the image plane cannot present an infinitely thin section of the specimen because each image point is spread into a diffraction pattern that extends above and below this plane. The depth of field is the axial distance above and below the specimen plane that appears to be in focus and does not lose detectable sharpness of the images with readjusting the microscope and is different from the depth of focus which is the thickness of the imaging plane). The parts of the image that lie outside the DOF tend to be blurred and less sharp. Both depth of focus and depth of field is determined by the numerical aperture of the objective; higher NA systems have deeper focus depth which translates into a thicker image plane even though the depth of the field is less. In long-term time-lapse imaging, the specimen may drift resulting in a loss of contrast and quality in the final image. A perfect focus system (PFS) is a unique solution for maintaining the specimen in focus throughout imaging.

BOX 3

Depth of Field is the distance from the nearest **object plane** in focus to that of the farthest plane while the specimen appears in-focus and can be calculated from:

$DOF = \frac{\lambda.n}{NA^2} + \frac{n}{NA.M}d$

Where DOF represents the depth of field, λ is the wavelength of light, n is the NIR of the medium, NA is the objective numerical aperture with the magnification of M, and e is the smallest distance that can be resolved by a detector.

Depth of focus refers to the depth of the image plane and represents the depth of the image. Depth of focus value changes with NAA and magnification of the objective lens. High NA systems represent deeper focus depths than do those systems of low NA.

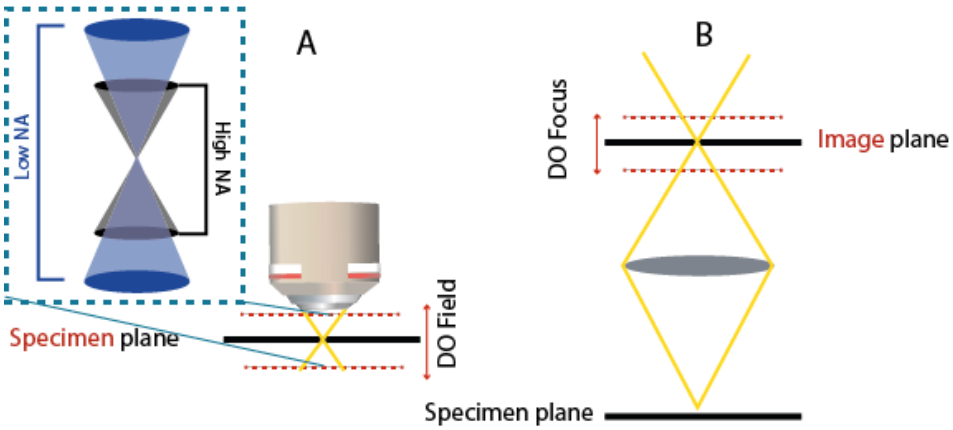

Figure 3.7: Depth of field and depth of the focus.

The Perfect Focus System (PFS) automatically corrects the drift occurring during the live-cell imaging caused by temperature changes and mechanical vibrations. An auxiliary optical system containing a NIR light LED (870 nm), offset lenses, and a sensor is introduced into the microscope via a dichroic mirror. Upon initiation of the PSF system, the focus point of the objective lens and PSF lenses are coincided

at the focal point of the specimen at zero offsets to make a reference plane. Any drift of specimen from the reference plane is tracked and detected in real-time by the CCD and is corrected within a millisecond by the offset unit. The offset ranges available with the PFS unit are determined by the type of objective lens being used (from zero from glass coverslip interface to 10 μm for oil immersion objectives, 20 μm for water immersion objectives, and 100 μm for dry objectives). **Figure 3.8** shows a schematic diagram of a PSF unit. PSF unit is advantageous for long-term imaging where mechanical or thermal drift may hamper the imaging, especially for high resolution (high NA) objective lenses where small drift disturbs the best focus due to the low Depth of field.

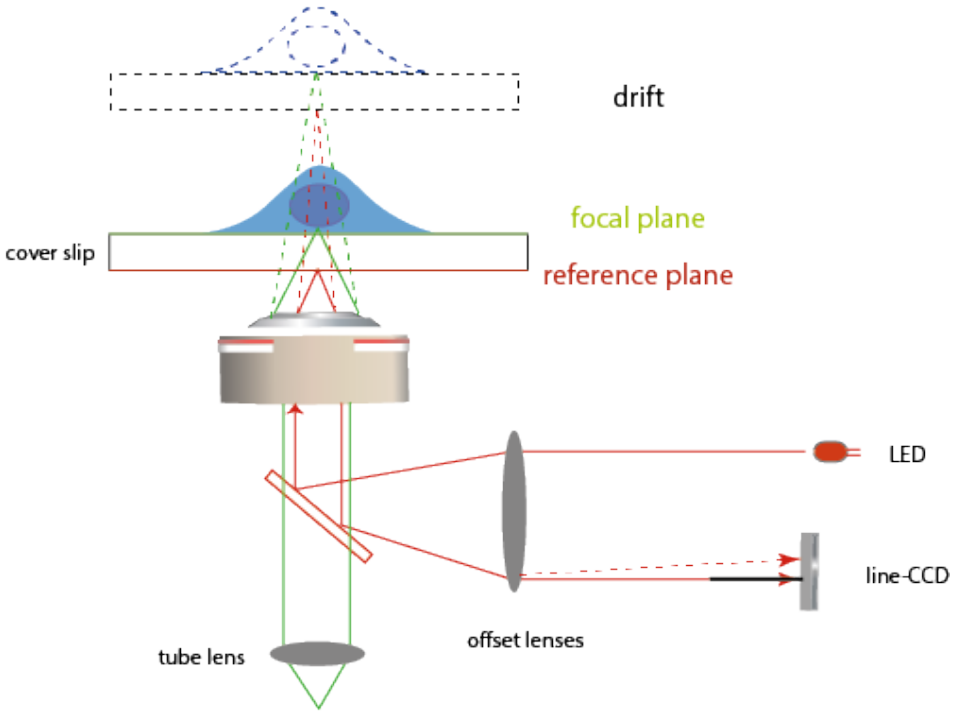

Figure 3.8: Perfect focus system. Any change in the position of the coverslip is detected by PFS and is relocated to the reference plane.

3.1.3 Phototoxicity and Live-cell Imaging

Fixed sample imaging only provides a snapshot of a specific cellular process at a given time point. This can damper the interpretation of data, particularly in highly dynamic processes such as plasticity and neuronal development. To fully apprehend these processes, live-cell imaging obtains dynamic information consisting of continuous events that occur over time and space. The development of fluorescent proteins (FP) and other live-cell dyes have opened up exciting opportunities for live-cell imaging. In live-cell imaging of synapses, the main challenge is to balance the "photon budget" to obtain stack images of high Signal to Noise Ratio (SNR) with the time and intensity of the light that is shone onto specimens to prevent photodamage. Therefore, the ideal live-cell imaging modality is sensitive enough to generate high-quality images from fluorescent samples, while is fast enough to capture synaptic contacts and their changes. Synapse remodeling can happen in a time ranging from a few minutes in immature to months for mature neurons.

The sensitivity of the system helps us to reduce exposure time and intensity of the light to obtain an optimal SNR (BOX 1) while maintaining cell viability. Long-term light exposure to living cells may lead to phototoxicity and photobleaching and consequently to cell death. This may be more critical in 3D volumetric imaging as the whole specimen must be illuminated for each image plane.

Efficient FP expression in specimens avoids using high laser power. This can be achieved by removing or preventing background in the field of view (FOV) in the course of imaging. One way to avoid excessive background is to label the specimens collectively.

Concerning synaptic contacts, ideally, several cells can be labeled to avoid creating a bulk of fluorescent samples that not only makes the interpretation of the data complicated but also impacts the quality of the final image. Sparse labeling along with live-cell imaging not only provides invaluable information about the synaptic interactions of individual neurons but also technically helps with the optimal SNR

of the images. The suitable microscopy technique candidate generates 4D (3D + time) with a rate enough to capture neuronal contacts and avoid phototoxicity and photobleaching.

3.1.4 Multicolor Imaging

Fluorescent labeling of any proteins in living cells is now possible by introducing the respective DeoxyriboNucleic Acid (DNA). This DNA encodes a Fluorescent Protein (FP) variant using simple molecular cloning methods and then expresses the encoded protein in cells. It is becoming more common to simultaneously use two or more different fluorescent dyes of distinctive colors for imaging cells' compartments or various cells of a sample. This brings us to the concept of sparse labeling. In sparse labeling, cells are labeled with fluorophores of distinctive colors so that the architecture of the neurons can be selectively visualized. In the 1870s, Golgi developed a technique, also known as a black reaction, to stain brain tissues (**Figure 3.10-A**) in a way that individual neurons were stained in their beauty and completeness. Perhaps the main success of this technique is in its inefficiency that not all the neurons in the tissue are labeled and one could trace neural circuits. The same idea was carried on centuries later when the Jeff Lichtman team[126] developed the Brainbow technique to paint neurons with 100 different hues.

Brainbow technique (**Figure 3.9**) takes advantage of additive primary colors, red, blue, and green, that can combine and generate hundreds of different hues in the visual spectrum. These RBG colors are generated from Fluorescent Proteins (FP) and randomly expressed in different ratios. The result is individual tagged neurons with a distinctive color. This color-coding is possible through what is called Cre-lox recombination. This process relies on two components to function; 1) DNA sequence Lox and 2) the Cre- recombinase enzyme to recognize, cut, and rearrange specific tag sequences of DNA. Inserting DNA equivalent of FP of three colors into cells, each DNA has cutting sites called LoxP. The Cre protein stochastically chooses a

pair of Lox sites to cut and eliminate from the DNA sequence. Then the neuron expresses the very first gene of the sequence. Given different colors of FP and through the action of Cre, each neuron contributes to creating its own unique mix color of random ratios of the original FP DNA. Brainbow techniques discriminate neurons from the adjacent and allow following individual neuron branches as they crisscross over other neurons' processes and reach their contact partners throughout the brain. There are different strategies (DNA excision or DNA inversion) that are used to create a brainbow that can be found in A. Weissman et al. 2015 [127].

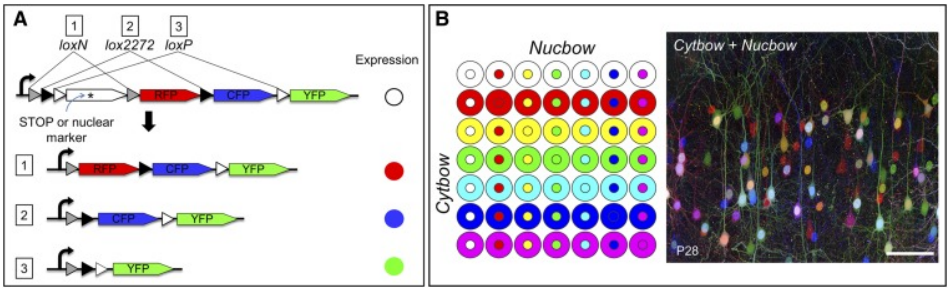

Figure 3.9: Brainbow technique. A) A Brainbow construct with equal probability of expressing RFP, CFP, or YFP. B) sparsely labeled neurons with brainbow technique

The brainbow technique indicates the importance of multicolor microscopy imaging by which neural networks can be visualized individually. Multi-color fluorescence images can be acquired either by simultaneous or sequential multicolor excitation. In sequential multicolor imaging, different color fluorescence images are obtained by sequentially switching both excitation wavelength and emission filters or different emission paths for each color. This requires multiple optical components and detectors increasing system size and complexity. The Sequential multicolor acquisition may impose limitations for live-cell observations as the time of imaging increases in proportion to the number of images for one stack of multicolor images. Simultaneous multicolor imaging in fluorescence microscopy can be performed by a color camera which is relatively expensive with a higher noise level compared to monochromatic cameras. Because each pixel of a monochrome sensor can detect a broader spectrum

of light due to the absence of the color filter arrays, their performance in low signal improves over the color camera.

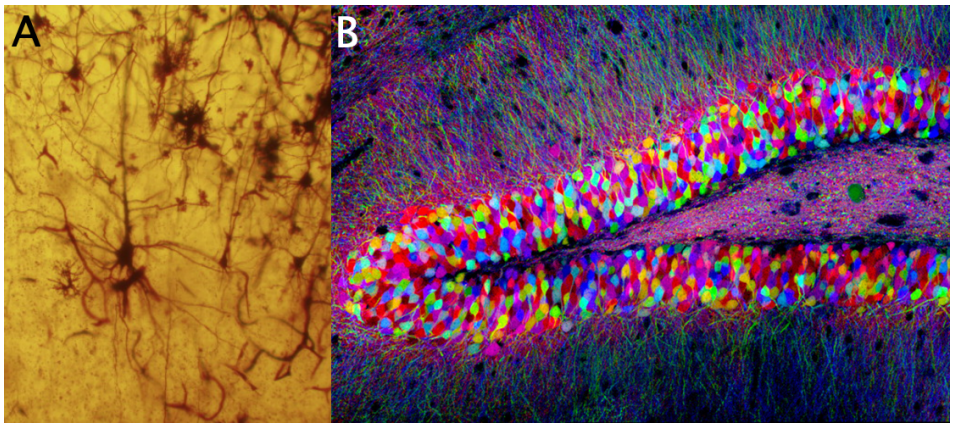

Figure 3.10: Sparse labeling of nervous tissues. A) Golgi's staining technique of individual neurons of the dentate gyrus B) Brainbow technique expression in a layer of the hippocampus expressing Brainbow

3.2 Current Techniques

The non-destructive nature of optical microscopy has made it popular in diverse areas, such as studying living specimens. The early microscopes achieved cellular imaging in a thin specimen yet provided us with valuable information about living matter. Still, the desire to pursue "deeper" insights to extend our view from 2D to 3D of the entire sample has prompted the exploration of alternative microscopy approaches, allowing imaging cellular events in real-time in live samples.

In this section, we present the principle of established microscopy techniques and assess their ability to perform 3D imaging of neuronal contacts in real-time. For this purpose, we grouped the microscopy technique based on their detection methods to laser scanning microscope (or single-photon counting recording) and parallelized detection.

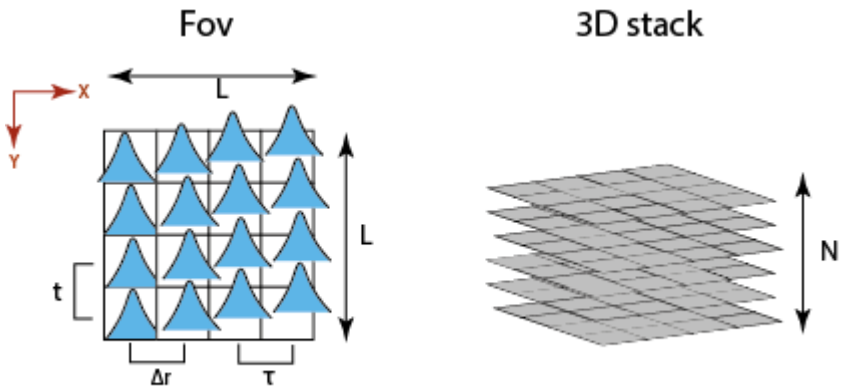

Figure 3.11: Laser scanning microscopy principle. Light raster the specimen with a pixel dwell time of τ that is the time the focused laser beam raster on a single pixel. The acquisition time for such a system is calculated in (BOX 4).

BOX 4

FOV and acquisition time in LSCM: Let us Suppose an LSCM that images a FOV with LxL and the pixel spacing Δr defined by Rayleigh resolution of the objective lens and pixel dwell time of Δt. Then the total acquisition time can be written as $(L/\Delta r)^2\Delta$t. If the acFOV increases by a factor of P, the acquisition time increases by a factor of P^2. Now to image a volume of N the acquisition time can be calculated by $(L/\Delta r)^2\Delta t P^2 N_z$. Besides, there is a non-zero delay to move from one axial plane to the next. Therefore, image a large volume using an LSCM at the resolution of Δr the acquisition time significantly increases.

3.2.1 Laser Scanning Techniques

In a conventional microscope, a wide area of the object is illuminated by the light source, and it returns 2D images with relatively high contrast and speed. However, in thicker samples, these 2D images often contain a high level of background signals that significantly obscure specimen details and reduce contrast. Laser scanning microscopes refer to two main techniques: confocal and two-photon microscopes. In

both techniques the laser beam raster across the sample by scanning galvanometer mirrors. To scan a typical 2D frame, representing a single optical section within a 3D sample, the laser beam spot of less than 1 μm is directed onto a pair of scanning mirrors sweeping the beam in x and y-direction. The laser beam must dwell over 512 lines, each comprising 512 points. The signal from each point is then transmitted to a photon-counting detector. The scanning process is repeated for multiple focal planes, which is called a z-stack. An appropriate algorithm processes the z-stack to generate a 3D image of the object.

3.2.1.1 Confocal Microscopy

In laser scanning confocal microscopy (LSCM) light from a laser is focused on a specimen and excites the fluorescent light on the cone of illumination. The fluorescence light passes through a pinhole in a conjugate image plane in front of a detector along the fluorescence detection path. The pinhole blocks the out-of-focus fluorescence and only allows the emission from the in-focus plane (**3.12-B**). This creates an intensity profile of the scanned area on the sample which is scanned back and forth in a raster pattern across the sample to create an image. To create a 3D image, the same raster scan is performed for each plane of the 3D structure. Upon collecting successive images of all-optical sections of the sample, a 3D image stack is generated. The pinhole size in the LSCM can affect the spatial resolution of the final image. By increasing the diameter of the pinhole (> 1 Airy Unit (AU)), more extra focal light is allowed to pass and overall intensity and SNR seem to improve (if the pinhole is infinitely large, the microscope acts like a non-confocal widefield microscope **3.12**). By closing the pinhole diameter to 0.2 AU, the axial resolution improves by 1.4x compared to the 1 AU pinhole diameter. This of course comes at the cost of the poor SNR (95% loss at 0.2 AU). I The size of the airy disk, hence the diameter of the pinhole, depends on the wavelength of the light and NA of the objective lens. To offer the best compromise between optical sectioning and SNR

the pinhole diameter is traditionally set to 1 AU.

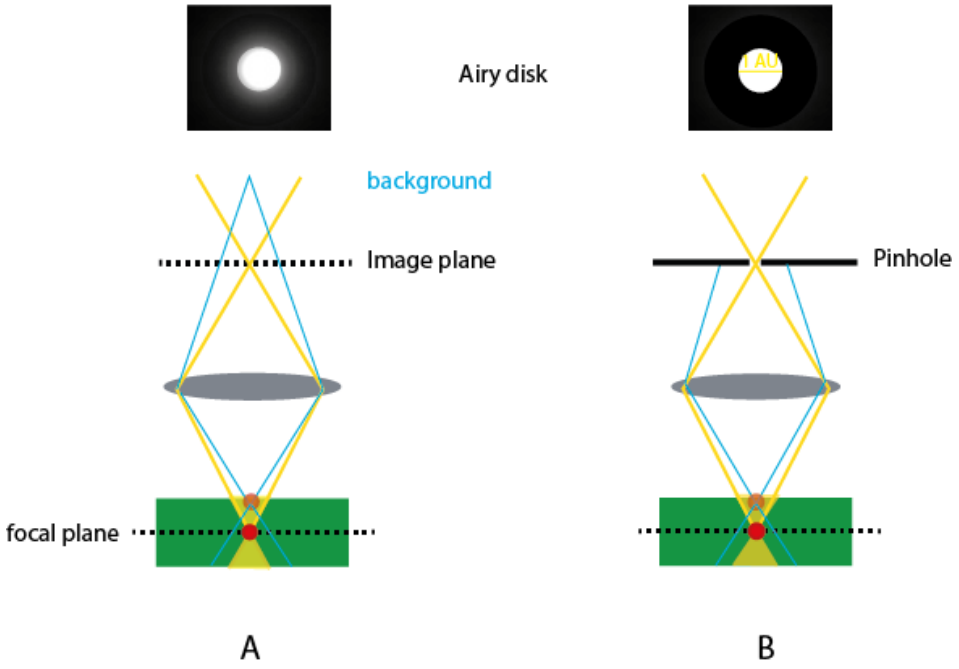

Figure 3.12: out-of-focus lights in thick samples. A) In a widefield microscope, the intermediate image of a point source is detected from the focal (yellow) and the extra focal plane (blue. The detector then records both signals, resulting in a blurry disk. B) A pinhole at the intermediate image plane blocks the extra focal signal and only allows in-focus light, resulting in a crisp in-focus disk.

The pinhole size in the LSCM has a considerable effect on the spatial resolution of the resulting image. By increasing the diameter of the pinhole (> 1 airy unit or AU), more extra focal light is allowed to pass and overall intensity and SNR seem to improve. By closing the pinhole diameter to 0.2 AU, the axial resolution improves by 1.4x compared to the 1 AU pinhole diameter. This of course comes at the cost of the poor SNR (95% loss at 0.2 AU). I The size of the airy disk, hence the diameter of the pinhole, depends on the wavelength of the light and NA of the objective lens. To offer the best compromise between optical sectioning and SNR the pinhole diameter is traditionally set to 1 AU.

limitations:

Confocal microscopy offers great optical sectioning to generate images of 3D structures. This technique is a gold standard to image brain tissue. Study of the density and morphology of dendritic spines, The use of the CSM brings with it several potential problems. Foremost among them is the increased risk of phototoxicity and photobleaching. Nevertheless, the detected emission light is from the in-focus plane, the entire sample is illuminated in the z-direction (**3.12**). The scanner contains galvanometer mirrors that direct the laser light in the x and y direction of a single FOV and then move incrementally across the entire sample to produce an image of the optical section. The speed of this method is limited by scanning mirrors. In modern confocal microscopes, acousto-optic tunable filters (APTFs) are implemented to rapidly attenuate laser light and select which wavelength excites the specimen. They also turn off the laser beam during the backward scan time which may avoid unnecessary light exposure to the sample. The photomultiplier tube (photomultiplier tube (PMT)) is the most common detector used for weak signals. Two essential detector characteristics in 3D microscopy are; Quantum Efficiency (Quantum Efficiency (QE)) and Noise Level (BOX 1). The former refers to the actual signals at the detection level contributing to an output signal to the photon input[128]. QE in a PMT has now reached a level of 43% at 350, close to its theoretical value nm[129]; yet a considerable portion of the signals do not contribute to the outcome. To accumulate more signals, either scan speed must be lowered to allow longer excitation dwell times, or the intensity of the excitation must be increased. Either way, it increases the photodamage. More current detectors are semiconductor technology, represented by APDs (avalanche photodiodes), and Hybrid detectors that combine vacuum and semiconductor technologies to offer beneficial features of both. However, to scan a 2-D frame, the laser must dwell over each point in about 5 microseconds. PMTs are very sensitive but have a low QE for converting the photons of the emitted fluorescent signal into photo-electrons. They detect 10% or less of the fluorescence signal that gets through the pinhole[130].

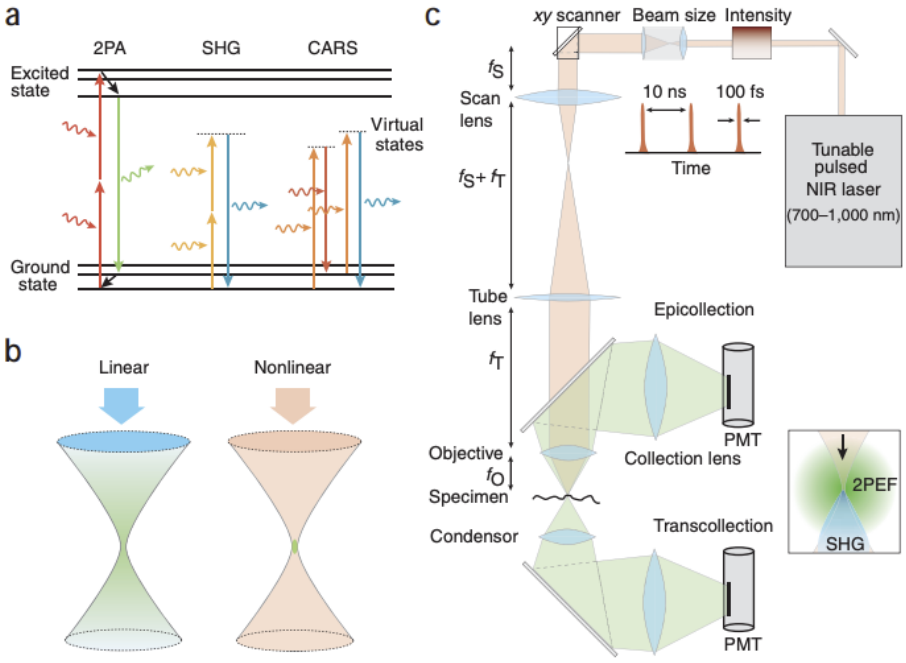

Figure 3.13: Two photon Microscopy layout and principle. Adopted from [122]

3.2.1.2 Two-Photon Microscopy

Another laser scanning technique with unique properties for optical sectioning is 2-Photon Microscpy (2PM) based on Two-Photon Excitation (2PE) of the specimen. The (2PE) is a nonlinear process in which the absorption of two photons is adequate to induce a molecular transition to an excited electronic state. In a two-photon process, an ultra-short pulsed laser (80–250 fs) excites the fluorophore to a virtual excited state followed by absorbing the second photon simultaneously, which brings the molecule to the excited state **Figure3.13-a**. One significant hallmark of (2PM) techniques is that both scattered and unscattered photons during the imaging process can be collected [131] [132]. Since 2PE is inherently confined in focal volume, essentially all emitted photons from the in-focus area could be collected (**Figure 3.13-b**). The depth of focus in 2PM results from the quadratic dependence of the excitation probability of the fluorophore on the spatial photon concentration

resulting in highly efficient removal of out-of-focus beam light. This property provides excellent optical sectioning to image thick specimens. Other advantages of 2PM include being less phototoxic with greater depth penetration owing to the NIR light (BOX 5). For live imaging at synaptic levels, this technique suffers from several drawbacks. Similar to confocal microscopy, the scanning approach and photon detector cause slow acquisition time. Other disadvantages include the considerable cost and size of regenerative amplifiers and their near lack of wavelength tunability. Two-photon microscopy is, in particular, useful for the interrogation of neural processes. For instance, uncaging of signaling molecules such as glutamate because the stimulation can be confined at small voxels of synapses. Another application of 2PM is to visualize cellular structure and function in living animals at depths far beyond possible for other microscopy techniques (e.g. confocal microscopy)[132]. In vivo 2PM has become an indispensable tool for investigating synapse development and plasticity[133][134][135]. However, to generate a 3D image sequential raster scanning of the excitation volume is required which decreases the data acquisition rate, especially in larger sample size or FOV (BOX 5 and **Figure 3.14**). Moreover, finite fluorophore lifetime and concentration limit the efficiency of photon generation rate even with very fast scanning mechanisms. Thus, to improve the acquisition rate in 2PM, a parallelized excitation process is one effective approach. In recent advances, a technique called temporal focusing axially modulates the photon density and achieves axial confinement in large areas with millisecond temporal resolution and sub-millisecond temporal precision[136]. Underlying concepts of temporal focusing are demonstrated in **Figure 3.14**.

BOX 5

Light penetration in nonlinear optics:

In the nonlinear process of 2PM only non-scattered photons contribute to signal generation in the focal voxel (focal volume). This on-scattered power follows the Lambert-Beer exponential and can be quantified as $P_nonscattered = P_0 e^{-z/l_s}$. In 2PE because of quadratic intensity-dependence, the fluorescence intensity declines as $P_{2PE} \propto (e^{-z/l_s})^2 = e^{-2z/l_s}$ where z represents depth,l_s length constant, and surface power of P_0 d. Therefore, the maximum light penetration is proportional to the scattering mean-free path (l_s) and depends logarithmically on laser power. Assume a laser with 100 fs pulses the maximum depth is limited by the average power resulting in an imaging depth of 600-800 μm in neocortex[122].

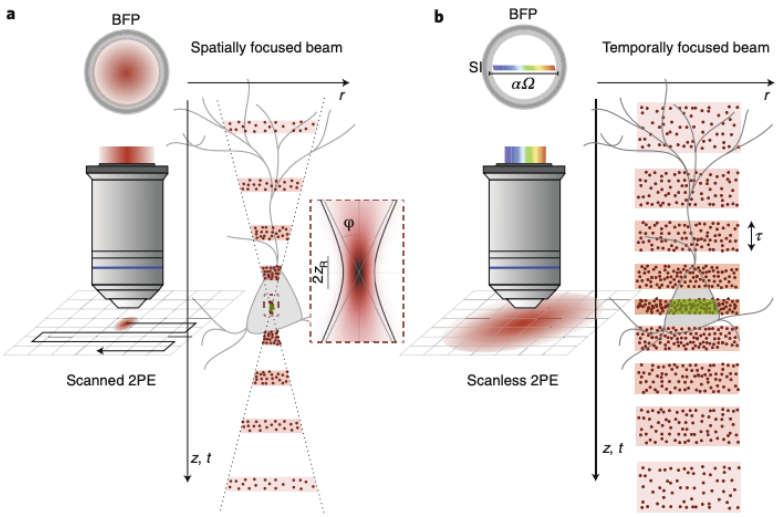

Figure 3.14: Spatially and temporally focused beams. a) An optical pulse is spatially focused and sweeps along the axial direction with constant temporal pulse width. The distribution of photons is a way that it reaches a maximum at the focal voxel where the two absorptions are proportional to the square of the power. b) A diffraction grating is placed at the conjugate image plane allowing the laser pulses 'disperse' in time and simultaneously excite the whole plane. Adapted from[136].

3.2.2 Parallelized Detection Techniques

While 2PM and LSCM are powerful techniques to image 3D optically dense structures, their slow acquisition rate hinders in vitro observation of neuronal interactions in real-time. The grand challenge of understanding the neuronal interactions in complex neuronal circuits in 3D lies in the lack of imaging modalities to monitor the dynamics at a sufficiently high spatiotemporal resolution and with a low level of photodamage. To address these challenges, parallelized illumination and detection approaches in 3D imaging have become popular in the recent past. In this approach, all voxels (3D pixels) are simultaneously excited and detected resulting in a relatively fast imaging speed and high photon budget.

3.2.2.1 Spinning Disk Microscopy

One way to increase the scan time without compromising the SNR is to illuminate several pixels simultaneously and collect light from all of them at the same time. A Spinning Disk Confocal Microscopy (SDCM) employs a disk with a series pinhole aperture. The pinholes are arranged on the disk in a way that by rotating the disk every location of the FOV is illuminated. As shown in **Figure 3.15** most light does not pass through the disk, but mini beams are created by each pinhole to sweep the image field by the disk rotation. Every mini beam is considered a confocal beam and each hole has an aperture for excitation and emission of light. One drawback of the SDCM is that a large portion of the illumination is wasted because of the disk and makes it inefficient in using the excitation lights which hampers imaging of very dim fluorescent specimens. In the new design, the illumination light is focused into pinholes using micro-lenses arranged in the pattern as pinholes[137] and greatly increases illumination efficiency to about 60%. The SDCM presents a compromise between resolution and SNR regarding the aperture size, as in LSCM. In a commercialized spinning disk system, the size of the pinholes on the disk is fixed and cannot be adjusted. The background rejection in SDCM is closely related

to the size and spacing of the aperture on the disk; the more pinholes are spaced, the stronger the background rejection is[130]. In the SDCM each of the pinholes creates a two cone-shaped (glass hour shape) illumination about the specimen. At the focal plane, out-of-focus planes are illuminated only by the cones from each spaced pinhole aperture. As the cones expand over distance, the cones from adjacent pinholes cross and excite the fluorophores, diminishing the axial resolution, especially in thick samples.

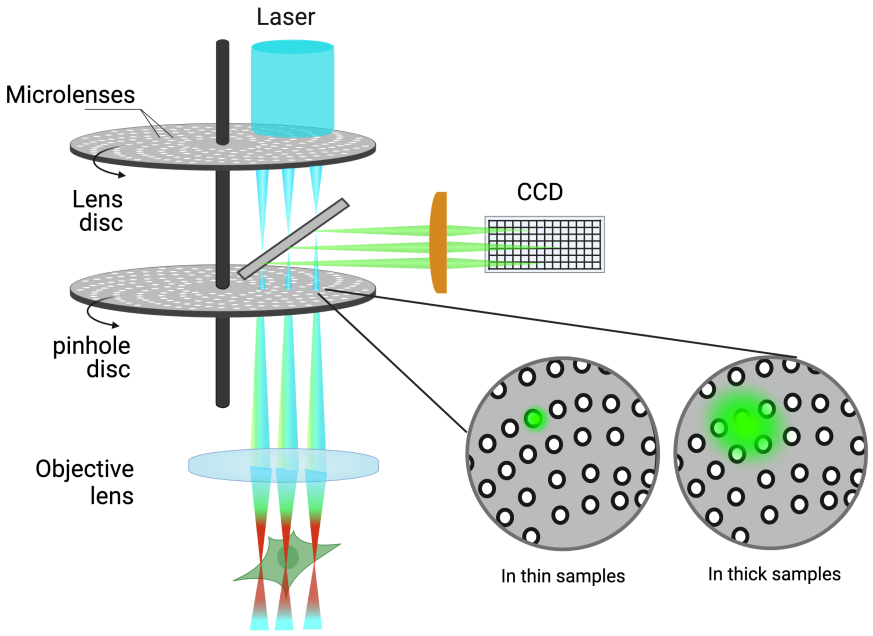

Figure 3.15: Spinning disk confocal microscope optical layout includes an array of lenses aligned with the pinhole on the spinning disk to focus light into each pinhole. The zoom schematic of the disk shows how light propagates and expands as it travels through thick specimens.

3.2.2.2 Light Sheet Fluorescence Microscopy

Light-sheet fluorescence microscopy (LSFM) or selective plane illumination microscopy (SPIM) was introduced in life sciences in 2004[138] although the concept was proposed already in 1904 by H. Siedentopf and R. Zsigmondy. In the recent decade, efforts have been placed on developing different instrumental designs clas-

sified as light-sheet microscopes, but they all follow the same was to provide optical sectioning, illuminating the sample with a thin laminar laser beam, generating fluorescence in a thin slice, and image with an array detector. The LSFM splits fluorescence excitation and detection into two separate light paths where the detection and illumination axis are perpendicular. In this configuration, two objective lenses are orthogonally aligned such that the thin sheet of light is positioned in the focal plane of the detection objective lens. A cylindrical lens, in the light pass, imposes convergence in the middle and then diverges out again, in a way that the waist beam is in the center of the sample. This thin illumination does not excite the entire illumination cone but instead introduces the light from the side on the plane of interest and image at the focal overlap. This is a unique feature for thick samples that provides inherent optical sectioning while avoiding excitation beyond the focal plane, resulting in high-quality 4D images with reduced phototoxicity and photobleaching. A few studies are comparing LSFM and confocal microscopy techniques to assess their optical sectioning capability and reducing photodamage during 4-dimensional imaging[139] [140] [141] [142]. Weber and colleagues[140] compared the spinning disk (SDCM) and the light-sheet microscopy (LSFM) for the effect of light exposure on living cells. They performed live-cell imaging on LLC-PK1 cultured cells expressing mEmerald-EB3 and observed EB3 signals quickly faded in the spinning disk microscopy, while little photobleaching of the sample in the LSFM system. They have also compared a published data cell cycle of retinal progenitors in zebrafish using confocal microscopy[143] and the LSFM and detected phases of the cell cycle in data from a confocal microscope are prolonged most likely because of higher phototoxicity. In the LSFM, as mentioned, the thin flattened beam is generated by a cylindrical lens in the y-direction, while forming a low-NA focus in the x-direction. Low-NA Gaussian is not, however, a real thin sheet and expands at beam waist (**Figure 3.16**) and forms a thicker beam longer range. A higher NA beam generates a narrower waist at the cost of a shorter z-range. This trade-off

makes it challenging to obtain both high-resolution optical sectioning and a large FOV[144]. One approach to circumvent this limitation is using Bessel beams which have a narrower wait with larger FOV but with side lobes, artifacts[145](**Figure 3.16**).

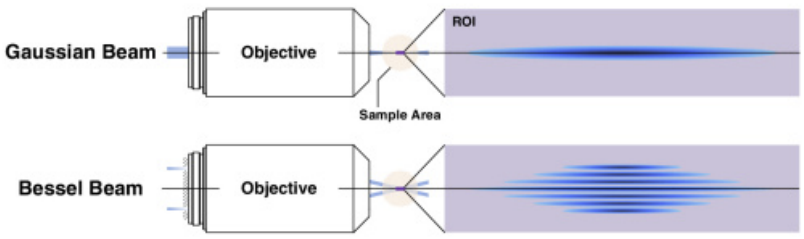

Figure 3.16: Bessel beam vs Gaussian beam illumination in LSFM. Represents the light intensity distribution along the propagation axis.

In the recent past, multiple different light-sheet approaches were suggested to overcome the limitations of traditional multi-objective light-sheet implementations such as objective coupled planar illumination (OCPI)[146],oblique-plane microscopy[147], swept confocally aligned planar excitation (SCAPE) microscopy[148]. These implementations have opened up *in vivo* interrogation of freely moving animals and small organisms and allow combining imaging with electrophysiology studies[144].

In neuroscience, the LSFM has become quickly popular owing to its flexibility to navigate between resolution, penetration depth, and acquisition rate with minimum photodamage and photobleaching. One of the exciting application of the LSFM is its ability to visualize entire neuronal networks for analysis in the intact brain[149][150][151][152][153][154]. The reason that the LSFM represents its great potential in fixed and clear samples is due to the limit for light to penetrate the sample horizontally. When the light sheet passes through the sample from its side, the light may undergo refraction, scattering, and absorption which translates into a quality degrading of the image from the left side (where the light initially enters the sample) and right side. This can be overcome by using a pivot scanner

to rotate the light sheet up and down allowing the illumination to penetrate beyond the optically dense structures. Some implies of LSFM combined with the super-resolution or two-photon excitation techniques have achieved fast, large-scale, and single-molecule resolution[155] [156] [157] [158]. What neuroscientists expect from microscopy imaging systems is to acquire data from a large population of neurons at a temporal resolution of 10-20 ms for the functional study of neurons. Furthermore, there is a need for imaging not only transparent samples but also non-transparent brain structures in real-time. There have been several studies on fixed nervous structures[159] or other transparent species than rodents animals such as larval zebrafishes[160] [161] [162] [163] [164] [165] [166]. The more recent advance in the LSFM includes using a 2D lattice that generates ultra-thin light sheets of 1μm to reconstruct 4D data with high speed (at 200–1000 planes/sec) and exceptionally low photodamage with improved axial resolution and usable field size[167]. For instance Lattice LSFM combined with expansion microscopy generates 3D rendered volumes of mouse brain tissue sections[168] [169] [170]. Although lattice LSFM readily achieves exceptional volumetric images of thick specimens, it relies on specialized high numerical aperture lenses that are only compatible with aqueous solvents (RI=1.333) with a relatively small FOV[159].

3.2.2.3 Structured Illumination Microscopy

Structured Illumination Microscopy (SIM) is a technique that overcomes spatial resolution limits by encoding lost information corresponding to high spatial frequencies in the sample through spatial frequency mixing. SIM employs a spatially patterned excitation light source together with an array detector to extract high-resolution information from low-frequency data that is otherwise lost by conventional microscopes. One main hallmark of SIM is its significant improvement in speed of acquisition compared to the point scanning microscopy techniques (3.2.1). However, for a single 2D reconstructed image several frames are required, thus, the

speed of acquisition in this technique scales with the speed of array detectors. **Figure 3.17-D** demonstrates the Optical Transfer Function (OTF) of a conventional microscope. OTF is defined as the Fourier Transform of the point spread function and describes the strength with which spatial frequencies are transferred to the image[171]. The OTF in SIM extends the supports in the frequency plane (k_x, k_y) by filling the missing cone (**3.17C-D**).

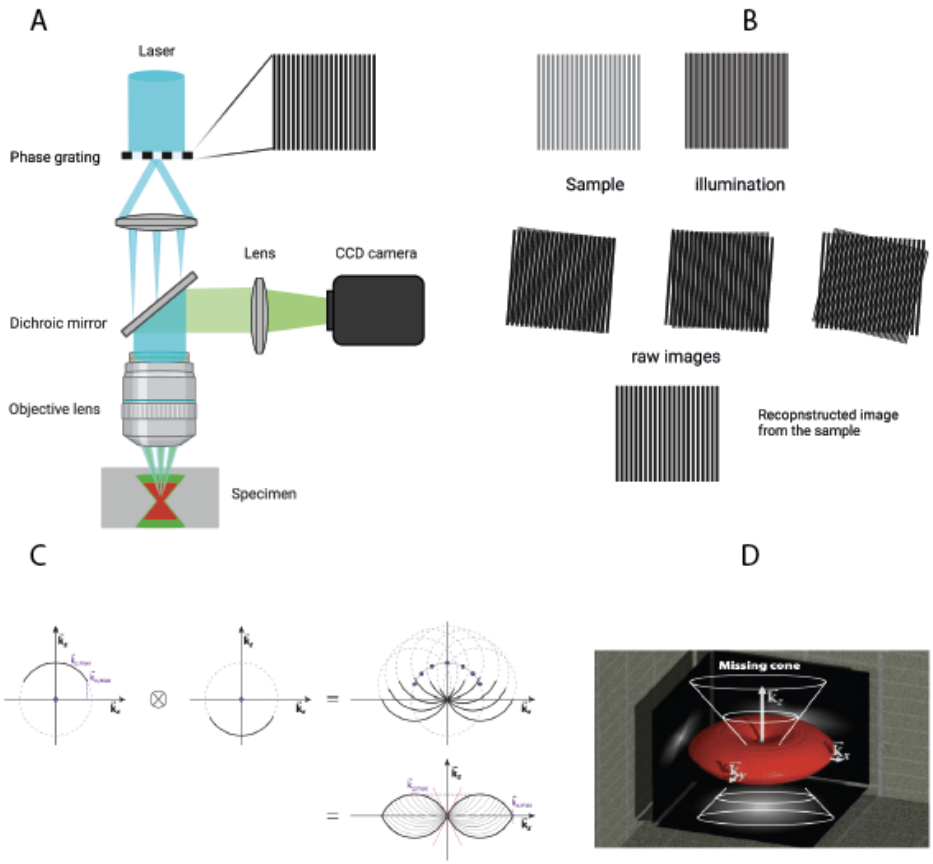

Figure 3.17: The schematic diagram of SIM and its principle. A) Laser light is modulated by a diffraction grating. The diffracted light is focused on the back focal plane of the high NA objective lens to generate a sinusoidal pattern. B) The grating is mechanically rotated to change the angle of the stripe pattern. The superposition of the stripe pattern with the sample creates an effect called Moiré: the overlap of two structures of high spatial frequency can generate a low spatial frequency. C)-D) The rotation of stripe patterns fills the missing cone and finally, a super-resolution image is reconstructed by computational methods, adapted from[118].

There have been several advancements to the classical SIM implementation. One of the implementations of SIM is referred to as super-resolution (SR) SIM, first introduced by Gustafsson and colleagues in 1995[172]. In the traditional SR-SIM, the modulated signal is usually generated by a spatial light modulator or a diffraction grating that creates multiple interfering beams (typically 2 and 3 beams). Diffraction orders originating from the high spatial frequency are placed farther on the observable region of BFP of the objective lens. By computational processing, the grating orders are separated, and spatial frequencies in Fourier space are shifted. The Fourier-transformed information of the sample can be shifted to make the missing cone area accessible and generate a super-resolved image. The second variant of SR-SIM is known as spot-scanning SR-SIM. In this technique, the fluorescence emission is collected by an array detector, instead of a point detector in LSCM. Super-resolution images can be reconstructed by the process of pixel reassignment through which a pixel offset from the excitation spot and detected fluorescent is corrected. Another recent advancement in SIM has been a technique known as an image scanning microscope (Image Scanning Microscopy (ISM)). The ISM first was introduced by Sheppard in 1988[173] but the concept was only implemented 20 years later by Müller and Enderlein[174]. Here, the authors suggested the term image scanning microscope for this technique and replaced the point detector with a detector array composed of a multitude of small light-sensitive elements for fluorescence detection. In this approach, each array serves as a pinhole and records images of the illuminated sample for each scan position. Then postprocessing reassigns the photon detected at different detector elements to their original point on the image. Despite its super-resolution achievement, this configuration suffers from the limited frame rate of the Charge-Coupled Device (CCD) camera. Another ISM implementation developed by A.York and colleagues[175] where they used a Digital Micromirror Device (DMD) as a spatial light modulator to generate sparse multi-spot patterns. The multifocal images are then captured and then digitally pinholed, re-scaled, summed,

and deconvoluted. The images processing improves resolution 2-fold compared to a conventional microscope providing a lateral resolution of 145 nm and 400-nm axial resolution at 1-Hz frame rates. In general, ISM and SIM both are known for their super-resolution capabilities that are beyond the diffraction limit. In this work, our focus has been on optical sectioning which is a critical feature to acquire high-resolution 3D images. The optical sectioning using structured light is achieved by spatial filtering. In optical sectioning SIM (OS-SIM) the sinusoidal modulation (incoherent light) is high only in proximity to the focal plane of the objective lens. Spatial frequencies in the OTF attenuates with defocus whereas PSF in planes away from the focal plane is uniformly illuminated which can be suppressed. The result is an optically sectioned image achieved by a discrimination algorithm[176]. **Figure 3.18** shows a schematic diagram of optical sectioning in SIM. In wide-field microscopy, the illumination is uniform without structures and therefore contains only the zero spatial frequency with no optical sectioning capability.

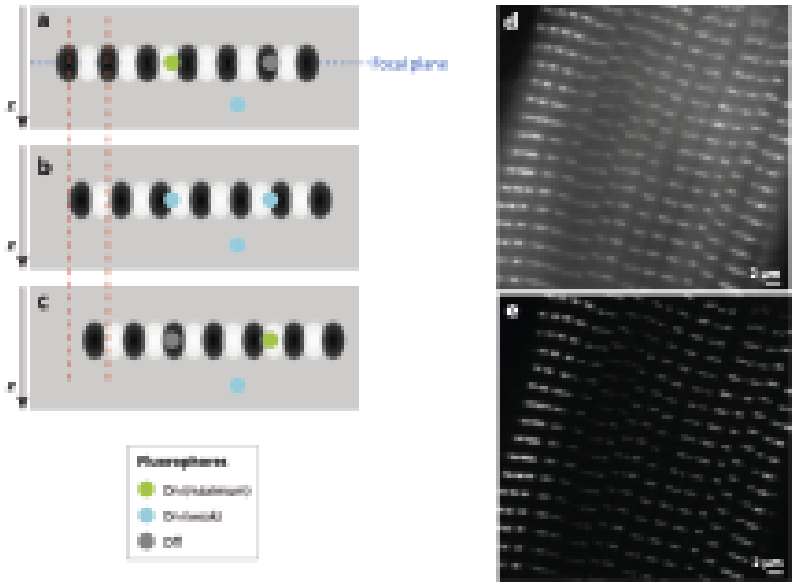

Figure 3.18: A series of z plane and optically sectioned sample acquired by SIM.a) The black (dark fringe) and white (bright fringe) dots represent the contrast of grating. a) The fluorophore that resides in the bright fringe is excited with a modulated signal, following an emission (green dot). The contrast of the grating points decreases in out-of-focus planes. b) By axially shifting the grating with a third of a period, other existing fluorophores follow the same rule and those in the dark fringe are not excited, and out-of-focus planes are excited only with uniform illumination with low contrast and therefore can be removed computationally (blue dots). c) Similarly, the grating is shifted by a third of a period, and fluorophore places in the dark fringes are not excited. Immunostained images of rat cardiomyocytes, d) acquired by a wide-field microscope e) acquired and reconstructed by a SIM. Adapted from [118].

3.3 Research Gap

As briefly discussed, laser scanning techniques such as established confocal and 2-photon microscopy techniques suffer from slow acquisition time and may not be a suitable technique to perform live-cell imaging for a long time. On the other hand parallelized detection techniques such as SDCM, LSFM, and SIM may be good candidates for time-lapse imaging with a temporal resolution of a few minutes. OptiOpticaltioning SIM technique offers efficient optical sectioning, resulting in high-resolution 3D images. With regards to the neuronal contacts observation, we emphasized the importance of multicolor labeling and imaging for better visualization of the neuronal branched and their connectivity. This requires the imaging system to simultaneously record neurons connections of different colors. To our knowledge, there is no technique 1) capable of optical sectioning to provide high-quality 3D imaging, 2) at the same time with high sensitivity to capture the image with a high temporal resolution, high SNR and, low photodamage and 3) allowing simultaneous multicolor imaging of neuronal contact for a long time.

3.4 Our Approach

In this work, we demonstrate a Spectral DMD-based ISM with optical sectioning and spectral resolving capabilities. The DMD generates multifocal or grid point patterns allowing to remove out-of of-focus light by spatially filtering the high-frequency contents in the focal plane. This approach provides optical sectioning for the thick specimen (<100 μm). We image 3D samples at one 2D image (1024x1024) per 2 seconds at resolutions around 350 nm laterally and 450 nm axially. We obtain 196 frames originating from the spacing between the illumination points and shifting them to cover the FOV. To perform simultaneous multicolor imaging, we employed a prism to disperse emission lights on the camera. The final OS ISM image results from a summation of high frequencies sectioned frames. To perform simultaneous multicolor imaging, we employed a prism to disperse emission lights on the camera. In addition to 3D multicolor of fixed samples, we can monitor neuronal contacts in live at planes deeper than 50 μm. We can capture dynamics of sparsely labeled neurons in spheroids of size around 75-100 μm for a long time and simultaneously in multicolor.

3.4.1 Principle

When a thick specimen is illuminated by a uniform light, the fluorescent light from in-focus and out-of-focus planes is detected with zero spatial contents. When using structured light, on the other hand, the spatial information from in-focus and out-of-focus light can be discriminated. In other words, the out-of-focus light is not modulated in the same way as in the focal plane. It has been shown[123] that the structured light is lost in defocus. In another word, at the focal plane sample is illuminated by high spatial frequency, which is the frequency of the structured light, while out-of-focus light only contains low spatial frequency and therefore, can be removed in the image reconstruction process using a high-pass spatial filter with

a cut-off spatial frequency of lower than of the structured light. The structured excitation (point illumination pattern) in Spectral ISM is generated by a DMD. We employ spatial filtering using a 2D lowpass gaussian to attenuate low-frequency signals originating from out-of-focus lights. By subtracting the filtered low-frequency content of exa focus planes, the final image contains only high frequency and is optically sectioned. This reverse process is only for the sake of faster image processing in MATLAB (low-pass Gaussian filter process faster than high-pass Gaussian filter).

The core equation to show the optical sectioning in ISM summarizes in the following equation[177]:

$$g(u,\delta) = \Gamma(\delta).\left[2\frac{J_1[u\delta(1-\delta/2)]}{u\delta(1-\delta/2)}\right] \tag{3.1}$$

where u is $4kzn\sin^2(\alpha/2)$ and represents the defocus and δ^2 frequency coordinates, and Γ the first-order Bessel function. The Above equation is a form of the OTF $g(u,\delta) = P \bigotimes P^*$, indicating the effect of OTF on the defocus in high spatial frequency. In the conventional microscope which exhibits no optical sectioning, OTF for a thin fluorescent sheet is equal to one and independent of the defocus. For the structured light, on the other hand, the OTF drops rapidly by increasing defocus at high spatial frequency.

3.4.2 Optical Layout

The schematic diagram of the Spectral ISM system is mounted on an inverted microscope (Nikon, Ellipse Ti) illustrated in **Figure 3.19**. The optical setup contains a 4f system with focal lengths of 150 mm and a DMD in a plane conjugate to the image plane. The f4 system is made of two achromatic doublets that relay the image from the DMD to the microscope. A 100X silicone immersion objective magnified each DMD pixel of 13.68×13.68 μm in the sample plane. The 100 mW diode lasers with 408 nm, 488 nm, 563 nm, and 647 nm wavelengths serve as excitation sources. To reduce the laser speckle and to change the beam profile into

a uniform flat-top mode, we used a laser beam homogenizer (ALBEDO, ERROL) that combines a multimode input fiber with a laser de-speckled and a square-core multimode output fiber to cover the DMD area. The expanded and despeckled laser beam is then directed to the DMD at a 24-degree angle. The diffracted light from the DMD passes through a 4-f system, L1, L2, and the tube lens, Lt, before being reflected by a quadra-band dichroic beam splitter (Semrock, quad-notch) into the back focal plane of the objective lens.

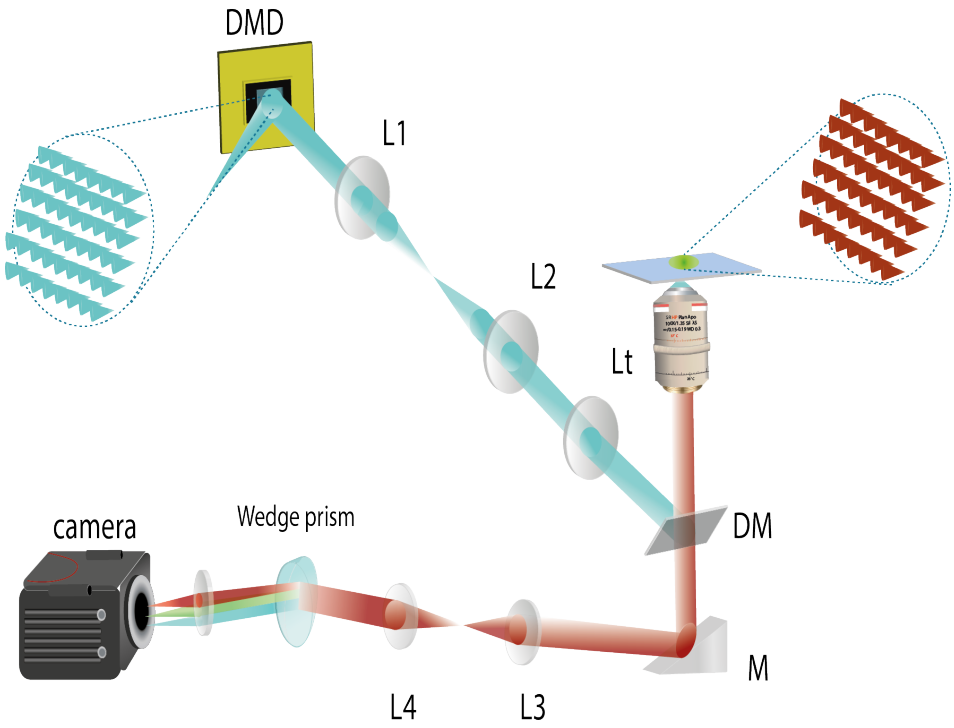

Figure 3.19: The optical layout of Spectral ISM

The sample is mounted on a manual XY and Z-axis motorized translation stage (Piezo) It can be moved axially in a maximum of 100 micrometers and a minimum 200nm step. The fluorescence light from the sample is directed into the camera port and passes through a 4f system with a wedge-prism (8 degrees, Thorlabs) and an achromatic lens. A CMOS camera (Hamamatsu Orca V.4 2024x2024 pixel with a pixel size of 6.5 micrometers) is employed to capture the fluorescence. The minimum

camera exposure time is 10 microseconds. Data collection, DMD patterns generation, and controlling cameras are implemented by custom software programmed in MATLAB. To build up the setup, first, a collimated laser module (650 nm) is centered on two adequately distanced apertures in a cage system. The laser is aligned using a two-axis translation mount. The cage system is then mounted onto the nosepiece of the microscope using an external thread. The aligned laser beam leaves the back of the microscope. To center the beam at the back of the microscope, we use an adjustable filter cube with 4 screws to move the beam in x and y directions. The beam leaving the microscope should be centered at two fairly distanced apertures (the first aperture after the tube lens and the second lens is placed on the Fourier plane of the 2f system). At this step, the diffraction of the DMD must be co-centered with the incident beam on the second aperture. The tube lens (200 mm) is placed in the back focal plane of the objective lens to use an infinity-corrected objective lens. The second (150 mm) is placed at the focal plane of the tube lens and is aligned such that the back reflection of the lens and the incident beams are fairly co-centered. The third lens (150 mm) is placed between the aperture and the DMD to create a 4f system. Then back reflection and incident beams are centered.

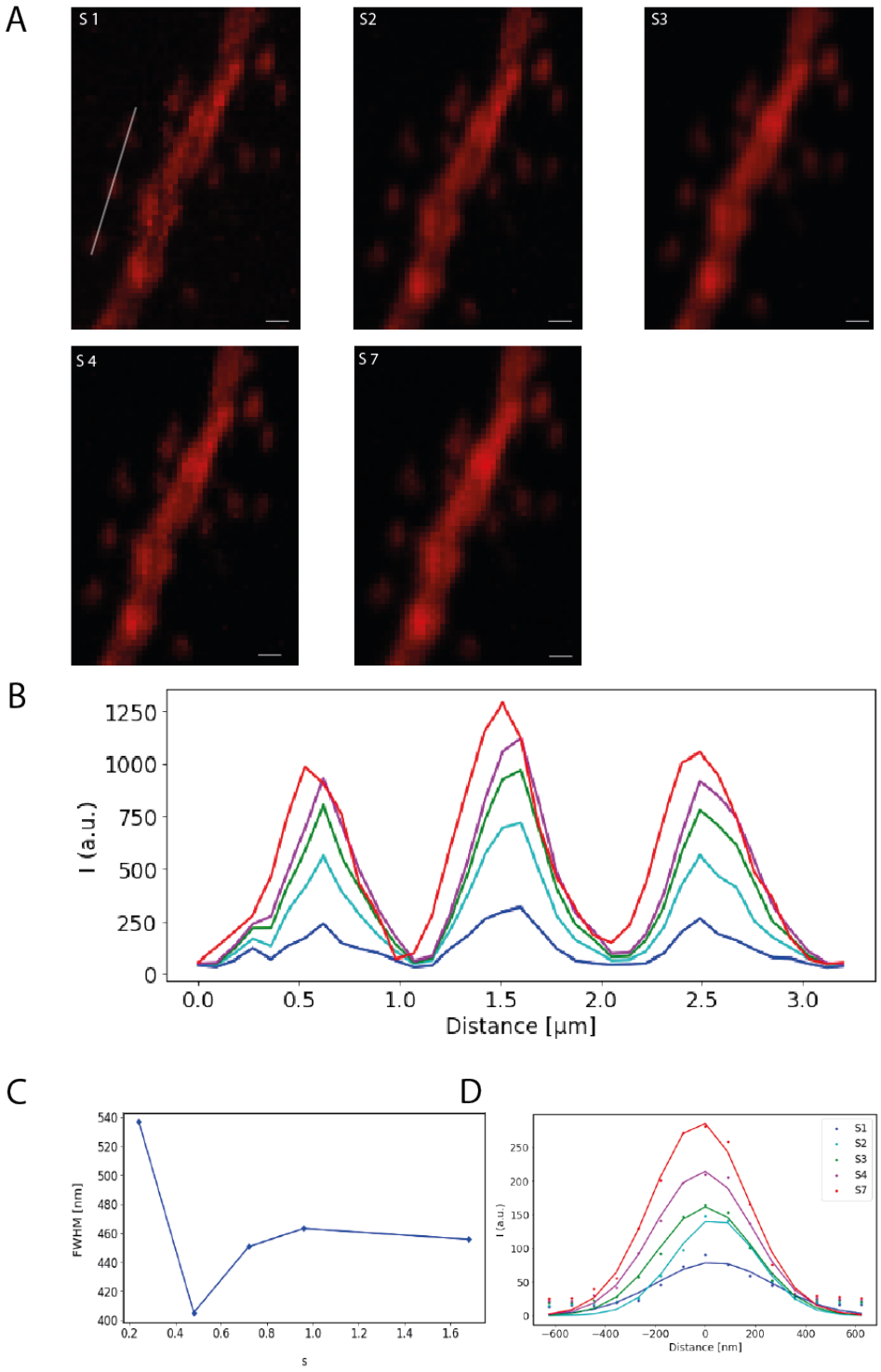

Figure 3.20: The effect of (S $=(\lambda/\sigma NA)$) on the axial resolution. A) Max intensity projection of a dendrite labelled with tdtomato reconstructed with different s values labeled in the images, scale bar = 4 μm. B) Axial Gaussian distribution for s values each from 15 spines. C) Full-Width-Half-Maximum calculated for s values. D) Intensity Z-profiles fitted with a Gaussian distribution for different widths, 'S'.

For a given illumination spacing and a sample, the optical sectioning can be adjusted by changing the spatial frequency of the Applying a Gaussian filter of larger size obtains more information from the ISM raw image, while a smaller filter passes less information from the raw image with higher SNR than the larger width. The size of the filter can be written as a dimensionless spatial frequency of ($s = \lambda/\sigma NA$). **Figure 3.20-A** illustrates the reconstructed images of dendritic spines with different 'S' values for the Gaussian spatial filter. The 'S1' value describes a small filter size with high FWHM. This value then drops to 450 nm for 'S2'. This stresses the strength of optical sectioning for S2 and its optimal size to obtain high spatial frequencies at the focal plane and suppress the unwanted signals from defocus planes.

3.4.3 Image Processing and Reconstruction

Obtaining optically sectioned images generated by Spectral ISM includes two main steps calibration and reconstruction. In the calibration steps, 1) DMD pixels are mapped on the camera pixel, and 2) dispersed emission lights are assigned to their illumination point captured on the camera image (up to 4 colors). 3) create a 3D matrix of x and y locations for each frame and color. In the reconstruction step 1) a 2D Gaussian low pass filter is applied on each of 196 frames, 2) illumination patterns for each color and position are summed to generate a 2D multicolor image.

Calibration: Mapping DMD and Camera Pixels

The pattern of grid points is created and arranged in hexagons. The hexagon arrangement provides a pattern of equally spaced illumination points. The grid points are projected on the DMD with a spacing of 14 pixels. Each 2x2 DMD pixel appears as a point illumination (see **Figure 3.21**). To cover the entire FOV, the grid point pattern is shifted in the x and y-direction. The spacing of 14 pixels generates 196 frames which produce one 2D image of the specimen. To map the DMD pixels on the camera, we use a homogeneously fluorescent layer as a sample. The DMD projects the grid point pattern on the fluorescent sample. The actual DMD pixel with the

coordinates of (x, y) appears as illumination points with coordinates of (x', y') on the camera. We locate (x', y') by finding the maxima of each illumination point in the on-camera image with an automated process of a peak finding algorithm. The actual (x', y') are located on the camera image with subpixel precision from the expected (x, y) position on the DMD. The actual and expected coordinates are fitted with a second-degree polynomial function.

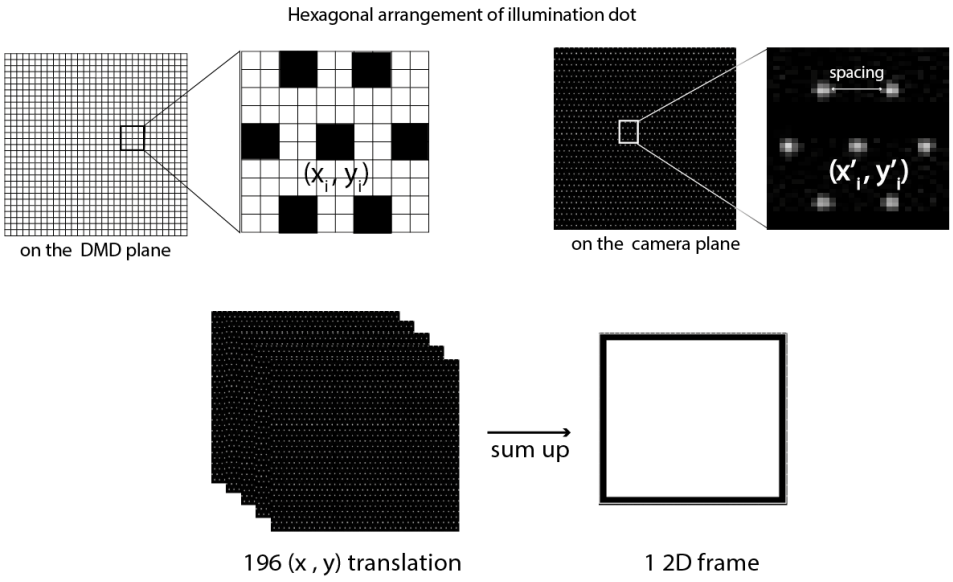

Figure 3.21: ISM calibration

Calibration: Color Assignment

In this step, we use our sample of interest labeled with one or multiple fluorescents have to be done for each sample separately. All the emission fluorescence that is recorded simultaneously appears as distanced points along the axis of the prism on the camera image. To assign and register each illumination point to its color, we extract a subimage of x-by-y centered at each illumination location and frame based on the expected illumination in the first calibration. Sub images are generated for each illumination point, color, and every 196 frames with corresponding camera plane coordinates. The sub-images are summed up to an image with x-by-y size containing the summed point illuminations (see **Figure 3.22**-A). Each summed

illumination spot is assigned to each color by defining a circle around the points by the user and stored (**Figure 3.22**-B). The output of this step is a matrix (a mask) with 1s inside the illumination points and 0s elsewhere.

Reconstruction: Generate Coordinates

3D matrices containing actual x and y point coordinates and the number of frames for each color are created. These 3D matrices contain 1s at the location of each illumination and zero otherwise. The expected x' and y' coordinates are generated using the first calibration. The output of this step is a generation of matrices assigned to each color.

Reconstruction: Spatial Filtering A 2D Gaussian lowpass filter is applied on each of the 196-point illumination frames. To optimally remove the background with a larger size of the filter, we introduce a threshold parameter that defines the background and any values below the threshold become zero for each frame and color. The output of this step is 3 3D matrices for each color and frame with a suppressed background. The illumination points for each color are still separated.

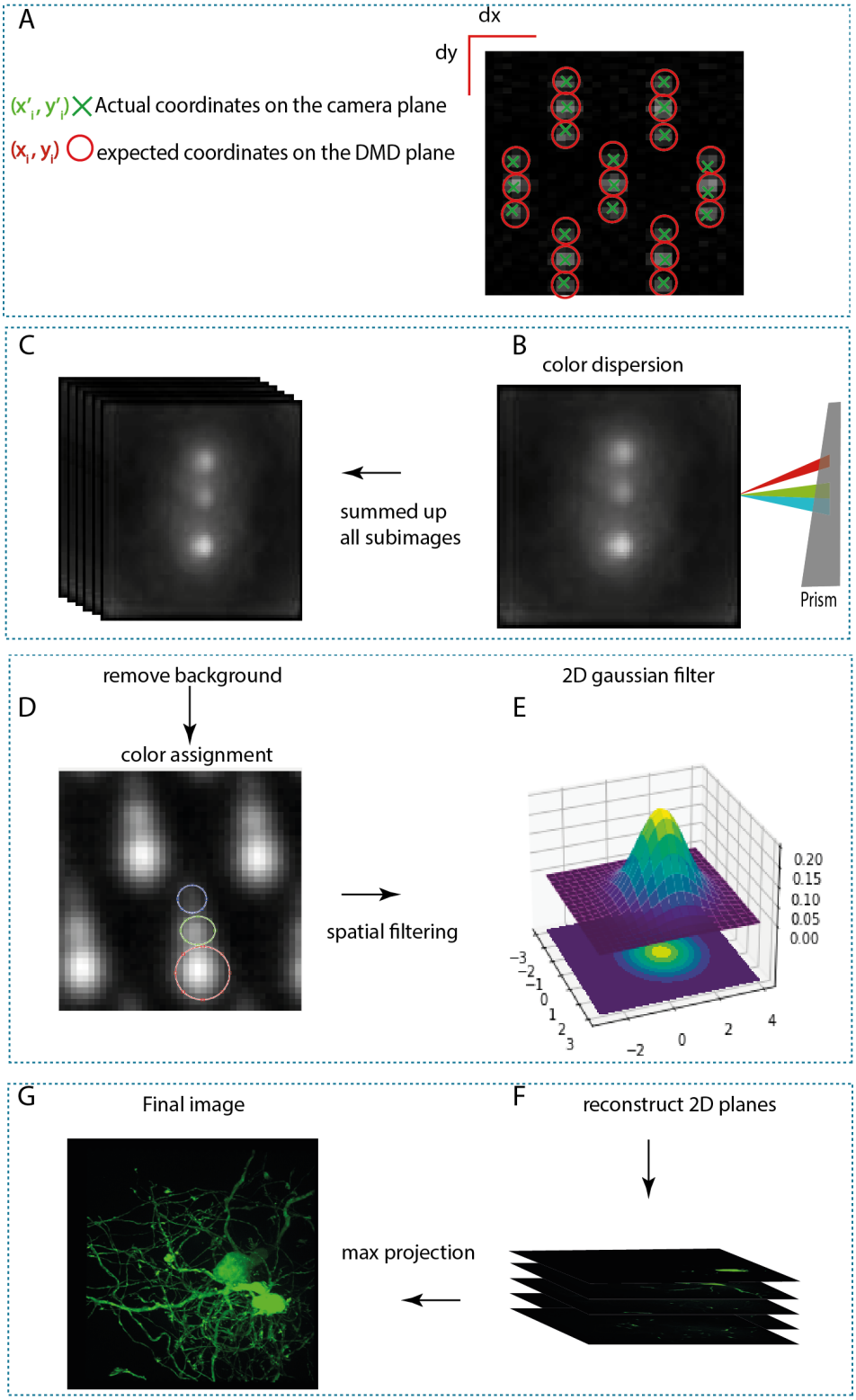

Figure 3.22: Color reassignments and image reconstruction

Reconstruction: Summing and Colocalizing Colors

The 3D Matrices of 3 colors with x-by-y size translated into the center of the maxima for each illumination point according to the expected coordinations. The output of this step is a summed 3D with the colocalized location of illumination points. Two main parameters influence the sectioning capabilities of a Multifocal (MF) illumination ISM for a given objective lens. Varying spacing between the illumination points and the Gaussian filter width, 's'. The spacing between point illumination also affects the speed of acquisition. Widely spaced points result in less background in the spatial filtering process, but entail more patterns and therefore, longer acquisition time. For the spacing of 14 DMD pixels, 196 frames with a minimum exposure time of 10 ms generate a 2D image in 2 seconds. Dense patterns, on the other hand, generate more background to the extent that it acts as a wide-field microscope in zero-spaced points. The spacing from 12-14 pixels is proved to be optimal to provide optical sectioning without much compromising on the speed of acquisition.

3.4.4 DMD in Optical Microscopy

A DMD is a light modulator, as a liquid crystal spatial light modulator, with spatial and temporal control over the illumination. On its surface, a DMD has arrays of micro-mechanically driven mirrors in a binary fashion. Each micromirror element is independently controlled and tilted along its diagonal between two 'ON' and 'OFF' modes with tilt angles of $+12$ and -12, respectively (See **Figure ??-A**). The OFF-position of the mirrors reflects the beam of the optical path while the ON-positions reflect the light to the optical path to spatially map each pixel of video data to a pixel on a screen. An important aspect of a DMD used in an optical system is its particular diffraction characteristic. According to the light diffraction in grating diffraction, light diffracts into several different directions (orders of diffraction) relative to the normal of the grating surface (**Figure ??-B**). The location of each order is determined by grating pitch, the wavelength, and the incident angle

of the beam. In such a design two possibilities are to occur: the blazed condition where the maximum grating efficiency in the diffraction pattern is concentrated in a specific order or off-blazed condition where the maximum intensity peak (center of the intensity envelope) falls between orders then multiple orders contain an equal amount of energy in the diffraction pattern. In the blazed condition, the center of the intensity envelope is not coupled with the zeroth order of diffraction but can be lined up with an order if the blazed angle, $\beta_m = 2\theta$ is fulfilled (**Figure ??-C**). For a given wavelength, only adjusting the indecent angle would coalign the intensity envelope peak with one of the diffraction orders to produce a blazed condition, thus, only one wavelength generates the center of the intensity distribution coaligned with the center optical path.

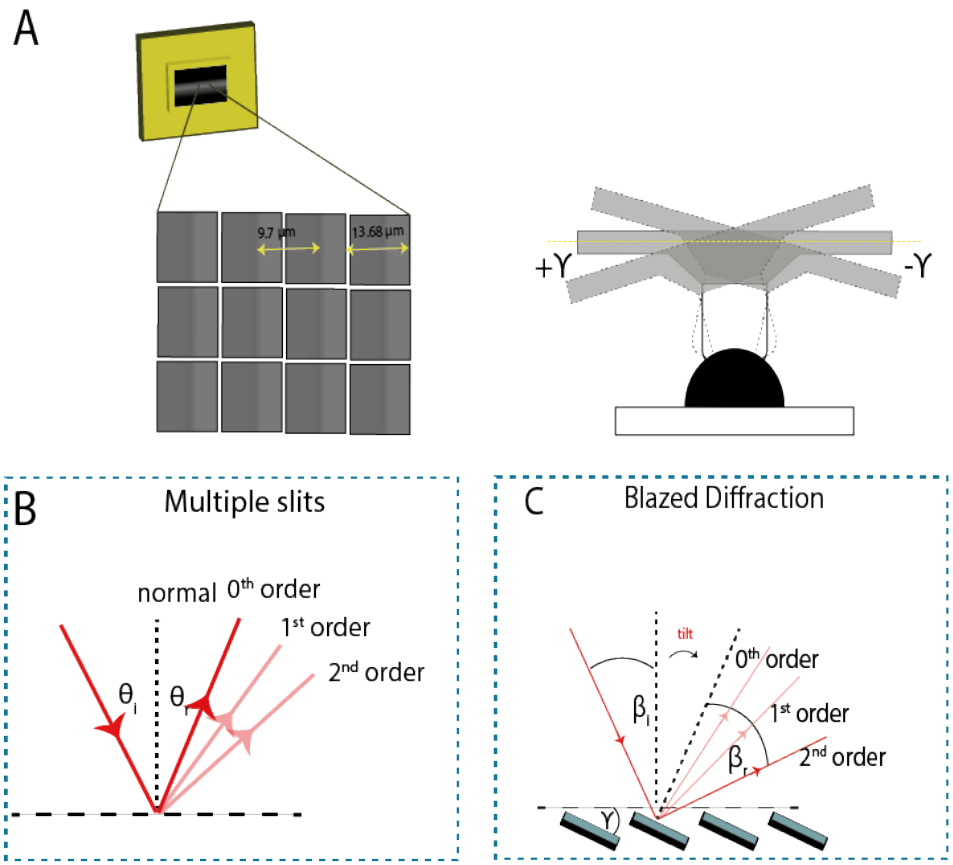

Figure 3.23: DMD configuration in an optical setup

3.4.5 Characterization

To characterize the system, an Argolight slide has been used. Argolight slide is a commercialized calibration system to monitor the performance of fluorescent imaging systems. In Argoslide, different patterns are embedded in a special glass substrate through the "brush fluorescent" technology to create non-bleaching reusable fluorescent geometries. These 2D or 3D patterns in Argoligh slide with known sizes in x, y, and z are fluorescent in the entire visible light which makes them a great tool for the assessment of 3D and multicolor images. **Figure 3.25** presents the 3D sphere pattern consist of three circles. The Argo-HM slide is designed for high-resolution microscopes (e.g., confocal microscopes).

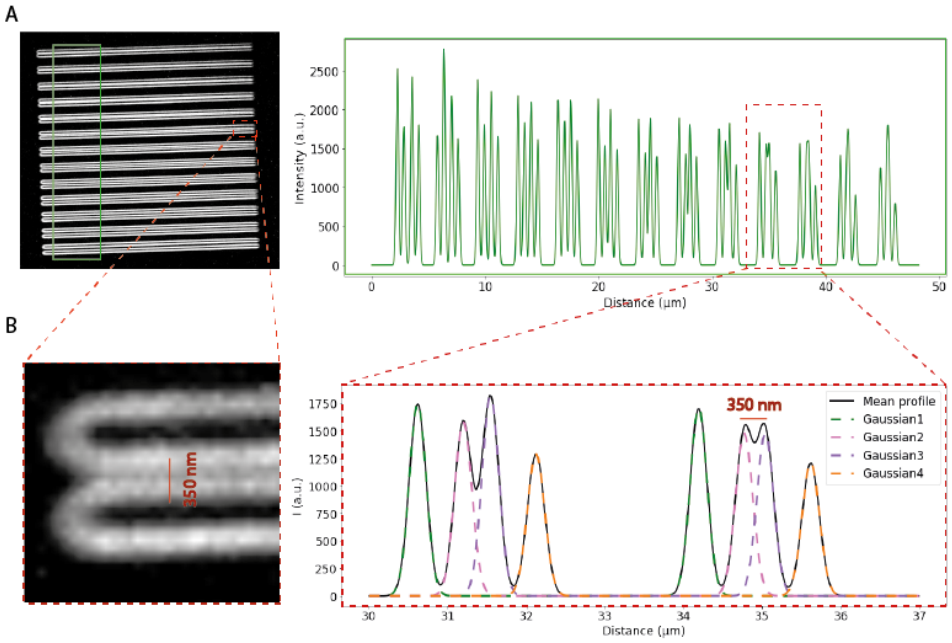

Figure 3.24: Spatial resolution assessment of Spectral ISM by Argolight slides. Image is recorded using a 100X silicone immersion objectove lens. The spacing between lines in this pattern gradually increases from 100 nm to 700 nm. The lateral resolution of Spectral ISM is shown around 350 nm.

Figure 3.24 represents spaced lines pattern with known spacing between each line that is gradually increasing. The zoom image shows the lines that can be re-

solved by Spectral ISM and indicate the lateral resolution of 350 nm. **Figure 3.25** illustrates a 3D view of a sphere pattern that can be used to assess the 3D reconstruction of our system using our Image reconstruction algorithm. The three-color image acquisition has been simultaneously reconstructed to generate multocolor 3D images of this pattern. The color reassignment is shown in **Figure 3.25- A** representing the colocalization of three color with our system. Here we used 3 different wavelengths (488, 563, and 647 nm) with 100 ms exposure time using a silicone immersion 100X. The reason for using such a long exposure time originates from the DMD and its properties for blazed conditions and as explained, the blazed condition is not fulfilled with the wavelength and current configuration of the system. This leads to the off-blazed diffraction in which the intensity of the maximum center of the envelope is distributed over 4 different diffraction orders, thus a significant reduction in light intensity at the image plane.

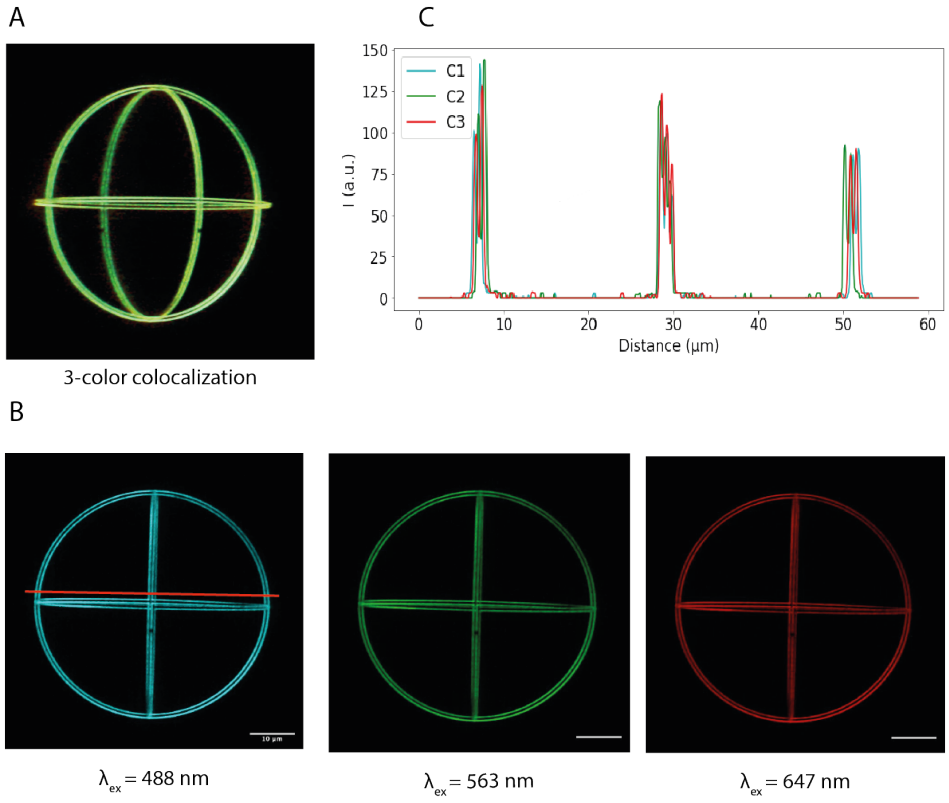

Figure 3.25: Spectral ISM characterization with Argolight slides. A sphere pattern is recorded simultaneously with 488 nm, 563 nm, and 647 nm excitation light. A) A 3D view of color reassignment and colocalization. B) Top and bottom 3D view of the reconstructed images for 3 colors. C) Intensity profile of the horizontal line shown in B.

3.4.6 Live-Cell Imaging of neuronal contacts using Spectral ISM

Using the *in vitro* model that we developed (Chapter 2), we have generated neuronal spheroids from rat dissociated cortical and hippocampal neurons. We designed a protocol (A.4) to create sparse labeling and mix the labeled and non-labeled neurons before cell seeding. The cells start to express on the following day. **Figure 3.26 - left** shows Spectral ISM max projection of a living spheroid expressing GFP and tdtomato after 14 day in vitro transfected using electroporation technique. Spectral ISM time-lapses were recorded using 488 nm and 563 nm excitation using a 40X oil immersion objective lens for 10 hours. The emission light of 2 colors was simulta-

neously recorded using a CMOS camera with 11 μs exposure time. The cells were kept in a chamber in physiological condition of 37 $\circ$ C and 5% CO_2 during the time lapse. The neuronal connectivity between neuron neurons of distinctive colors over the 10 hours time-lapse is shown in **Figure 3.26 - right**.

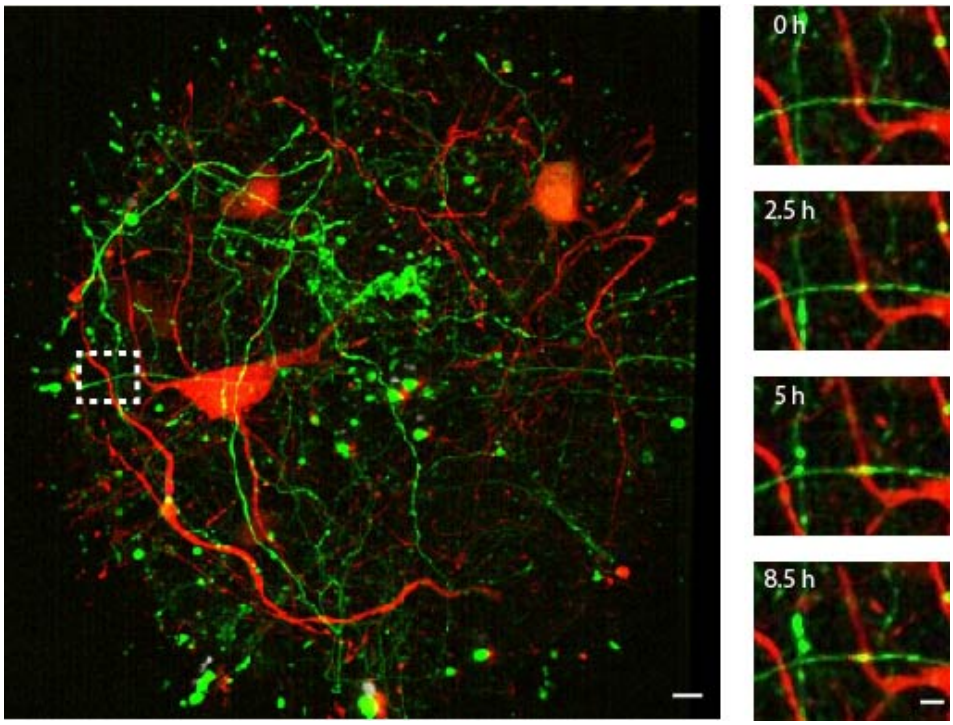

Figure 3.26: Live-cell time-lapse of neuronal contacts in spheroids recorded over 10 hours with 488 nm and 563 nm laser excitation. Left-image shows a max projection Spectral ISM z-stack recorded of the spheroid and neurons transfected with GFP and Tdtomato, scale bar = 5 μs. Right-image shows the dashed-box in 5 time points of the time-lapse, scale bar = 5 μm.

Chapter 4

Summary and Conclusion

In this study, we described a combination of a 3D engineered *in vitro* model with a spectral image scanning microscope that fulfills two key challenges in studying neuronal contacts and remodeling: a 3D *in vitro* synaptic model and a microscopy modality.

First, we aimed at reducing the complexity of the model to increase its amenability for further experimental manipulation. At the same time, we maintained its 3D architecture, mechanical, chemical, and physical cues. This versatile and controllable 3D micro-engineered model presents key features of the CNS microenvironment, namely neuronal subtypes, synaptic formation in an *in vivo*-like stiffness. For that, we used a UV projector PRIMO system which allows UV projection with high spatiotemporal control. This technology uses a spatial light modulator device, DMD, to generate illumination patterns with a high switching rate (10 kHz) and different gray scales. The UV projector along with a photoinitiator (PLPP) and pre-polymers (PEGTA) enables the fabrication of hydrogel templates in a versatile, time-effective, and user-friendly manner. PEG is a biocompatible, nonadhesive gel, and mechanically tunable by varying its polymeric length. This method benefits from the free radical photopolymerization process to transform a liquid mixture of a multifunctional PEG into a cross-linked macromolecule by a chain reaction initiated by reactive species. The initiation is formed by a benzophenone-based photoinitiator absorbing UV light to generate initiating radicals. These radicals then propagate and react with the prepolymer to create 3D polymer networks. In this protocol, there are a few considerations including the stiffness of the gels.

The stiffness of the gel depends on the length of the PEG macromers and PEGTA with the molecular weight of 10K Da (g/mol) has shown an effective degree of stiffness, maintaining the 3D polymer chains after the photopolymerization and rinsing process. The results for shorter (8K Da) PEG, photocrosslinked hydrogels are brittle and are readily deformed upon rinsing. On the other hand, longer (20K Da) chains of PEG result in swollen hydrogel templates. In the polymerization process, oxygen molecules inhibit several steps and reduce the overall effectiveness of polymerization. Our method turns this disadvantage into an opportunity to control the polymerization by creating oxygen gradients. For this purpose, PDMS slabs are used to confine the pre-polymer mixture with a gas-permeable top layer where oxygen molecules slowly diffuse through the reaction mixture of PLPP and PEGTA and essentially terminate or consume the radicals required for the polymerization. The result is height and size controllable hydrogel templates to generate neuronal spheroids. The result shows spheroids of size from 50-100 μm are formed in hydrogel templates offering *in-vivo*-like environments that promote self-assembly of dissociated neurons. In this model, cellular organizations and subtypes were characterized by an immunohistochemistry assay. The results are consistent with other studies[9] [178] and show neuronal subtypes including progenitor, neurons self-assemble and form neuronal aggregations. We demonstrated the effect of dose illumination and photon flux on the stiffness of the templates. This finding highlights the importance of the mechanical properties of hydrogels on the activity of neurons. Sparse labeling using electroporation of two different fluorescent proteins enabled selectively monitoring of neuronal connectivity. The sparse labeling allows first to differentiate between pre-and post-synapses for better visualization. Second, with regards to microscopy imaging, it improves the signal-to-noise ratio. The sparse labeling of spheroids revealed the formation of synapses and their contacts after 14 DIV inside spheroids. Controlling the size of the spheroids enables compatibility with measurements and optical imaging. This model comprises the complexity of the CNS with

the versatility for imaging microscopy and experimental manipulations.

The multifocal illumination offers an almost closed pinhole, but without an existing trade-off in signal-to-noise ratio in confocal microscopy with a speed enhancement of 2 seconds per spectral frame. This is accomplished by replacing the conventional photon detector with a detector array, i.e., a CMOS camera and a multi-spot illumination. A multifocal illumination pattern generated from a digital micromirror device is projected onto the sample resulting in simultaneous excitation of hundreds of spots with a high switching rate (20 kHz). The fluorescence emission spectrum from the sample is then dispersed by a prism at each illumination point along its axis. The Gaussian blur of the raw images for each pattern position (e.g., 196) was subtracted to obtain high-frequency information that only occurs at the focal plane. Consequently, each pattern position contains only high frequency modulated light and can be summed to a final 2D image with optical sectioning. Tuning two parameters, the width of the spatial filter and threshold to block background results in optimal image reconstruction for specimens with different SNR. For instance, when imaging samples with high SNR such as sparsely labeled neurons in 3D microtissues, a larger 'S', or filter size may provide a higher signal at the cost of lower optical sectioning. This results in reverse when directly obtaining the high frequencies from the raw image instead of subtracting the blur (low frequencies). In our algorithm, a low-pass Gaussian filter was applied and then substrated to achieve high spatial information. This is only for the sake of faster processing in MATLAB. In our reconstruction, subtracting blur comes with the benefit of faster image processing. On the other hand, when imaging noisy samples, the higher threshold can improve the SNR without sacrificing the optical sectioning.

In this work, we focused on the optical sectioning ability of the system, while it first introduced[174] by its ability to enhance the resolution 2-fold using pixel reassignment. The pixel reassignment can be done with our system, however, the presence of the prism may impact the lateral resolution to reach the 2-fold increase.w

Optical sectioning using spatial filtering presents more robust sectioning than deconvolution algorithms used in many microscopy techniques. Because in this approach spatial filtering applies to the raw image to suppress the low frequencies generated from out-of-focus planes while deconvolution separates out-of-focus light from the actual in-plane information. This is why ISM exhibits efficient optical sectioning at zero or little cost of SNR (contrary to confocal microscopy techniques). This gain of efficiency in photon collecting is advantageous for live-cell imaging, as sufficient SNR decreases the probability of cell damage in long-term imaging. Although classical SR-SIM requirements are faster, the DMD-based ISM is more robust to aberrations or reconstruction artifacts than traditional SIM implementations. This is crystal clear that for thicker samples, multiphoton excitation is necessary as the problem of light penetration in live samples is inevitable. LSFM implementations offer less background at the expense of spatial resolution and complicated sample preparation and mounting.

This technique along with sparse labeling of neurons in the spheroids can reveal neuronal connection and the level of synapses. The result shows the capability of the system for long-term imaging (20h) of 3D neuronal networks in two-color. The key feature of this technique, contrary to sequential multicolor techniques, is that acquiring a 3D stack from a sample fluorescent in different colors does not require extra time, as light is simultaneously dispersed along a prism axis onto the camera plane.

Appendices

Appendix A

Appendix Example

A.1 Appendix

A.2 Rat Primary Neurons

First, E18 Sprague-Dawley rats' embryos were sacrificed. Then the hippocampus and cortex were dissected. The dissociated cortical and hippocampal neurons were prepared as described by Kaech and Banker, 2006[179]. For 2D culture, cells were plated at a density of 200-300 x 103 cells per 60-mm dish containing coverslips pre-coated with poly-L-lysine for 1.5 hours (Marienfeld, cat. No. 117 580). Neurons were maintained in Neurobasal Plus medium and supplemented with 0.5 mM GlutaMAX and 1X B-27 Plus supplement (Thermo Fischer Scientific). Cells were plated. Cells were plated in supplemented Neurobasal Plus medium containing 1.5% Horse serum heat-inactivated. 48h later, the medium was replaced by a pre-equilibrated maintenance medium to remove Horse serum, and 2µM Ara-C was added between DIV 6-8, according to glia's proliferation.

A.3 Hydrogel-based Microwells

The hydrogel precursor is a mix of 5% of 4-arm-PEG-acrylate (Laysan Bio, Inc.) solved in 1X of PLPP photoinitiator (Alveole, Paris). The solution is then added to the PDMS stencil on a bioinert culture plate (IBIDI). The dish is placed at the stage of a converted microscope incorporated with the Primo system. A 100% UV light power for 60 seconds is shone. This step is repeated for each PDMS square, where the

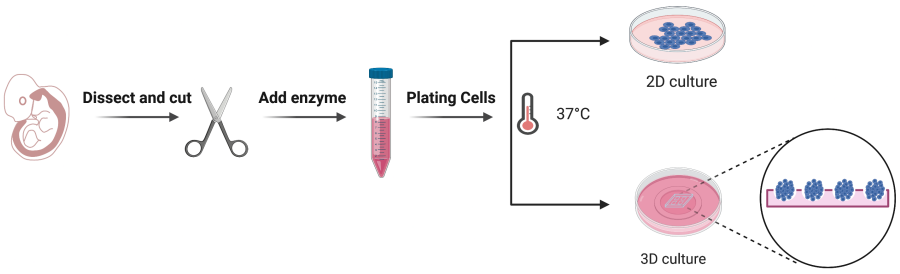

Figure A.1: Various methods to create 3D cell culture

hydrogel precursor is added. The plate is rinsed with water 3X followed by rinsing with 70% Ethanol. Then the culture plate is incubated with a culture medium at 37 C and 5%CO_2 for at least 30 minutes before seeding cells. With 1000 μl pipette, remove the medium from each PDMS area and add the dissociated neurons to each PDMS square without breaking the drops. Let the cells form aggregation for 2 hours. Then the prewarmed medium is added carefully to the dish. It is important not to add the medium vigorously as the cell aggregations can be disturbed.

A.4 Cell Electroporation

Cell Electroporation is a method for introducing DNA into living cells. This method permeabilizes the cell membrane by applying an electrical pulse and moving molecules into the cell via the electrical field. The cell membrane acts as a barrier for cells and hinders the free exchange of molecules between the cytoplasm and the cell's external environment. Upon applying electric puls, transient pores of small dimensions are formed and reseal when the supply of electric field is terminated. The protocol to transfect Neurons with NucleofectorTM is as following:

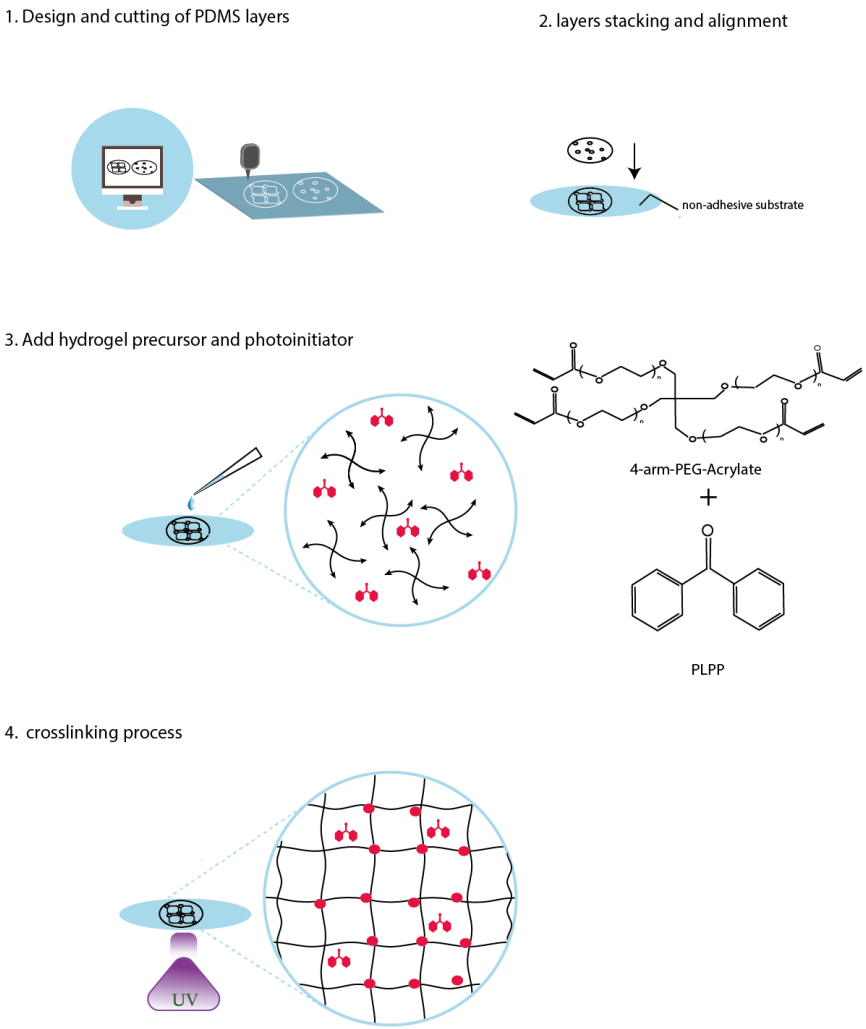

Figure A.2: Hydrogel based microwells preparation.

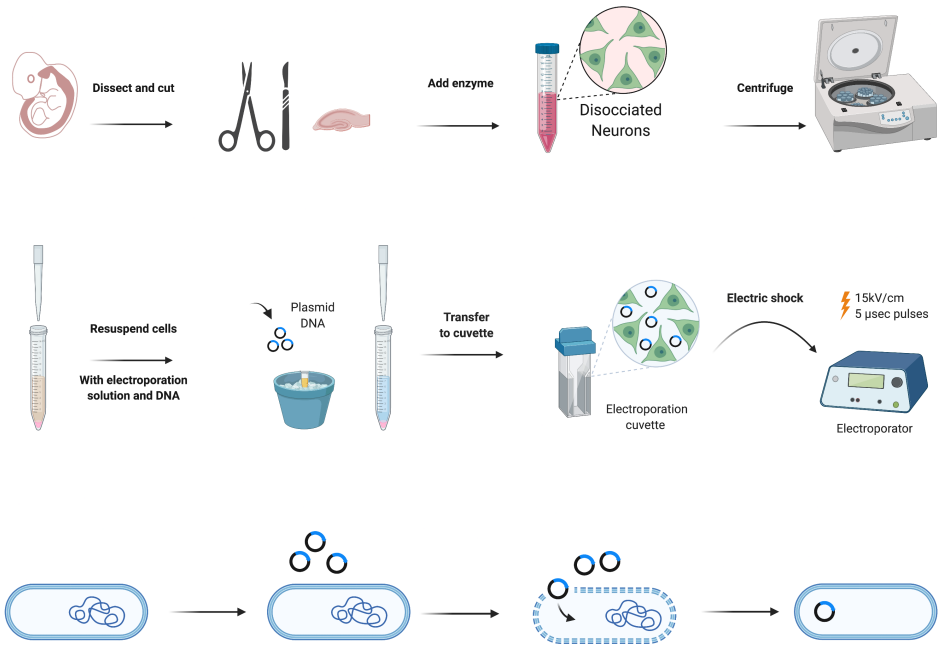

Figure A.3: Transfection of dissociated neurons using electroporation technique.

A.5 Immunohistochemistry

Immunohistochemistry (IHC) employs antibodies to target the location of proteins and other antigens of interest in tissues. The interaction between the introduced antibody and the antigen can be observed using either chromogenic detection with a colored enzyme substrate or fluorescent detection with a fluorescent dye. All the IHC experiments were performed using the following protocol:

Fixation

:

The Medium is removed from the culture vessel. Cells are incubated in 4% PFA for 15 minutes in RT. The cells are carefully rinsed with 1X PBS three times.

Blocking and permeabilization

:

Cells are incubated in 0.1% of Triton-100X and .03% of BSA for 30 and 60 minutes in RT, respectively. The last two steps are followed by 3X rinsing with PBS.

Antibody staining

:

Cells are incubated with the primary antibody of interest over night in 4C, followed by 3X rinsing. Then the secondary antibody with recommended concentration is introduced to the culture vessel and incubated for 2 hours, followed by 3X PBS rinsing. The plates are ready for imaging and can be stored in 4C.

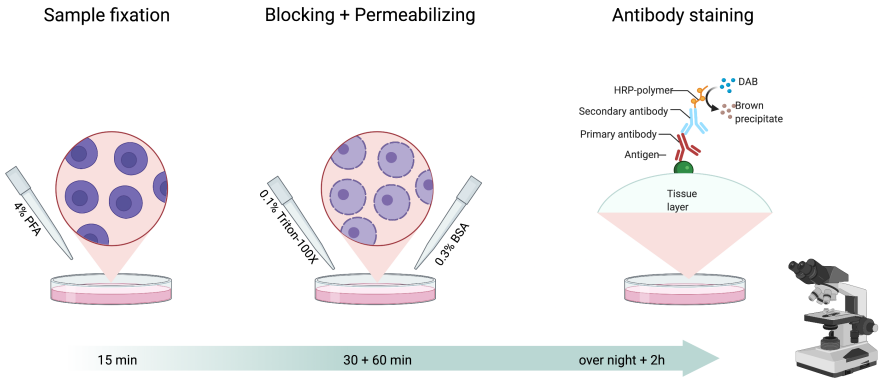

Figure A.4: Immunohistochemistry assay.

A.6 Confocal Microscope

Confocal imaging was done at Bordeaux Imaging Center, Bordeaux with the following microscope system: The excitation lights generated from a white light laser 2 (WLL2) with freely tuneable excitation from 470 to 670 nm (1 nm steps) and a diode laser at 405 nm was directed in to a Leica SP8 WLL2 on an inverted stand DMI6000 (Leica Microsystems, Mannheim, Germany). Light is scanned using either a conventional scanner (10Hz to 1800 Hz) or a resonant scanner (8000Hz). The illumination is then focused on the sample using two objective lenses with characteristics of oil immersion HCX Plan Apo CS2 (63X, NA of 1.40) and a Glycerol immersion HC PL APO CS2 motCORR (93X, NA of 1.3). The emission light was collected using 2 internal photomultiplier tubes (PMT), 2 internal hybrid detectors and 1 external PMT for transmission. The images were acquired by the LAS X Life Science (Leica Microsystems, Mannheim, Germany). The parameter to adjust in the software includes the excitation and emission range for the laser and the detectors. Pixel size and zooming were also tuned depending on the objective lenses.

Bibliography

[1] Mathieu Letellier, Florian Levet, Olivier Thoumine, and Yukiko Goda. Differential role of pre- and postsynaptic neurons in the activity-dependent control of synaptic strengths across dendrites. *PLOS Biology*, 17(6):e2006223, jun 2019. ISSN 1545-7885. doi: 10.1371/journal.pbio.2006223. URL https://dx.plos.org/10.1371/journal.pbio.2006223. (Cited on pages 2 and 58.)

[2] Madeline A. Lancaster, Magdalena Renner, Carol-Anne Martin, Daniel Wenzel, Louise S. Bicknell, Matthew E. Hurles, Tessa Homfray, Josef M. Penninger, Andrew P. Jackson, and Juergen A. Knoblich. Cerebral organoids model human brain development and microcephaly. *Nature*, 501(7467):373–379, sep 2013. ISSN 0028-0836. doi: 10.1038/nature12517. URL http://www.nature.com/articles/nature12517. (Cited on pages 3, 21 and 22.)

[3] Sergiu P. Pașca. The rise of three-dimensional human brain cultures. *Nature*, 553(7689):437–445, jan 2018. ISSN 0028-0836. doi: 10.1038/nature25032. URL http://www.nature.com/articles/nature25032. (Cited on pages 3, 5 and 18.)

[4] Molly E. Boutin, Liana L. Kramer, Liane L. Livi, Tyler Brown, Christopher Moore, and Diane Hoffman-Kim. A three-dimensional neural spheroid model for capillary-like network formation. *Journal of Neuroscience Methods*, 299: 55–63, 2018. ISSN 1872678X. doi: 10.1016/j.jneumeth.2017.01.014. URL http://dx.doi.org/10.1016/j.jneumeth.2017.01.014. (Cited on pages 5 and 22.)

[5] Hod Dana, Anat Marom, Shir Paluch, Roman Dvorkin, Inbar Brosh, and Shy Shoham. Hybrid multiphoton volumetric functional imaging of large-scale bioengineered neuronal networks. *Nature Communications*, 5(1):3997,

sep 2014. ISSN 2041-1723. doi: 10.1038/ncomms4997. URL http://www.nature.com/articles/ncomms4997. (Cited on pages 5 and 18.)

[6] M. D. Tang-Schomer, J. D. White, L. W. Tien, L. I. Schmitt, T. M. Valentin, D. J. Graziano, A. M. Hopkins, F. G. Omenetto, P. G. Haydon, and D. L. Kaplan. Bioengineered functional brain-like cortical tissue. *Proceedings of the National Academy of Sciences*, 111(38):13811–13816, sep 2014. ISSN 0027-8424. doi: 10.1073/pnas.1324214111. URL http://www.pnas.org/cgi/doi/10.1073/pnas.1324214111. (Cited on pages 5 and 18.)

[7] Madeline A. Lancaster and Juergen A. Knoblich. Organogenesis in a dish: Modeling development and disease using organoid technologies. *Science*, 345 (6194), jul 2014. ISSN 0036-8075. doi: 10.1126/science.1247125. URL https://www.science.org/doi/10.1126/science.1247125. (Cited on pages 5, 18, 20 and 21.)

[8] Junghyun Jo, Yixin Xiao, Alfred Xuyang Sun, Engin Cukuroglu, Hoang-Dai Tran, Jonathan Göke, Zi Ying Tan, Tzuen Yih Saw, Cheng-Peow Tan, Hidayat Lokman, Younghwan Lee, Donghoon Kim, Han Seok Ko, Seong-Oh Kim, Jae Hyeon Park, Nam-Joon Cho, Thomas M. Hyde, Joel E. Kleinman, Joo Heon Shin, Daniel R. Weinberger, Eng King Tan, Hyunsoo Shawn Je, and Huck-Hui Ng. Midbrain-like Organoids from Human Pluripotent Stem Cells Contain Functional Dopaminergic and Neuromelanin-Producing Neurons. *Cell Stem Cell*, 19(2):248–257, aug 2016. ISSN 19345909. doi: 10.1016/j.stem.2016.07.005. URL https://linkinghub.elsevier.com/retrieve/pii/S1934590916302004. (Cited on pages 5 and 18.)

[9] Yu-Ting L. Dingle, Molly E. Boutin, Anda M. Chirila, Liane L. Livi, Nicholas R. Labriola, Lorin M. Jakubek, Jeffrey R. Morgan, Eric M. Darling, Julie A. Kauer, and Diane Hoffman-Kim. Three-Dimensional Neural Spheroid Culture: An In Vitro Model for Cortical Studies . *Tissue En-*

gineering Part C: Methods, 21(12):1274–1283, 2015. ISSN 1937-3384. doi: 10.1089/ten.tec.2015.0135. (Cited on pages 5, 22, 24, 35, 45 and 104.)

[10] Martin Chalfie. The 2009 Lindau Nobel Laureate Meeting: Martin Chalfie, Chemistry 2008. *Journal of Visualized Experiments*, (36), feb 2010. ISSN 1940-087X. doi: 10.3791/1570. URL http://www.jove.com/index/Details.stp?ID=1570. (Cited on page 5.)

[11] Alberto E. Pereda. Electrical synapses and their functional interactions with chemical synapses. *Nature Reviews Neuroscience*, 15(4):250–263, apr 2014. ISSN 1471-003X. doi: 10.1038/nrn3708. URL http://www.nature.com/articles/nrn3708. (Cited on page 8.)

[12] Shanglin Zhou and Yuguo Yu. Synaptic E-I Balance Underlies Efficient Neural Coding. *Frontiers in Neuroscience*, 12, feb 2018. ISSN 1662-453X. doi: 10.3389/fnins.2018.00046. URL http://journal.frontiersin.org/article/10.3389/fnins.2018.00046/full. (Cited on page 9.)

[13] R.G.M Morris. D.O. Hebb: The Organization of Behavior, Wiley: New York; 1949. *Brain Research Bulletin*, 50(5-6):437, nov 1999. ISSN 03619230. doi: 10.1016/S0361-9230(99)00182-3. URL https://linkinghub.elsevier.com/retrieve/pii/S0361923099001823. (Cited on page 9.)

[14] Raphael Lamprecht and Joseph LeDoux. Structural plasticity and memory. *Nature Reviews Neuroscience*, 5(1):45–54, 2004. ISSN 1471003X. doi: 10.1038/nrn1301. (Cited on page 10.)

[15] Shigeo Okabe, Hong-Duck Kim, Akiko Miwa, Toshihiko Kuriu, and Haruo Okado. Continual remodeling of postsynaptic density and its regulation by synaptic activity. *Nature Neuroscience*, 2(9):804–811, sep 1999. ISSN 1097-6256. doi: 10.1038/12175. URL https://www.nature.com/articles/nn0999{_}804. (Cited on page 10.)

[16] Glen S. Marrs, Steven H. Green, and Michael E. Dailey. Rapid formation and remodeling of postsynaptic densities in developing dendrites. *Nature Neuroscience*, 4(10):1006–1013, oct 2001. ISSN 1097-6256. doi: 10.1038/nn717. URL http://www.nature.com/articles/nn717. (Cited on page 10.)

[17] Peter Penzes, Michael E Cahill, Kelly A Jones, Jon-Eric VanLeeuwen, and Kevin M Woolfrey. Dendritic spine pathology in neuropsychiatric disorders. *Nature Neuroscience*, 14(3):285–293, mar 2011. ISSN 1097-6256. doi: 10.1038/nn.2741. URL http://www.nature.com/articles/nn.2741. (Cited on page 10.)

[18] R Harrison. BIOLOGY AND MEDICINE . Observations on the living developing nerve fiber . *Scientific Proceedings*, 98(241), 1907. (Cited on page 12.)

[19] J LEIGHTON. A sponge matrix method for tissue culture; formation of organized aggregates of cells in vitro. *Journal of the National Cancer Institute*, 12(3):545–61, dec 1951. ISSN 0027-8874. URL http://www.ncbi.nlm.nih.gov/pubmed/14889259. (Cited on page 12.)

[20] A. Moscona. THE DEVELOPMENT IN VITRO OF CHIMERIC AGGREGATES OF DISSOCIATED EMBRYONIC CHICK AND MOUSE CELLS. *Proceedings of the National Academy of Sciences*, 43(1):184–194, jan 1957. ISSN 0027-8424. doi: 10.1073/pnas.43.1.184. URL http://www.pnas.org/cgi/doi/10.1073/pnas.43.1.184. (Cited on page 12.)

[21] R. J. Petri. Eine kleine Modification des Koch'schen Plattenverfahrens. 1887. (Cited on page 12.)

[22] Luise Schultz, Marie-Gabrielle Zurich, Maxime Culot, Anaelle da Costa, Christophe Landry, Patricia Bellwon, Theresa Kristl, Katrin Hörmann, Silke Ruzek, Stephan Aiche, Knut Reinert, Chris Bielow, Fabien Gosselet, Romeo Cecchelli, Christian G. Huber, Olaf H.-U. Schroeder, Alexandra Gramowski-

Voss, Dieter G. Weiss, and Anna Bal-Price. Evaluation of drug-induced neurotoxicity based on metabolomics, proteomics and electrical activity measurements in complementary CNS in vitro models. *Toxicology in Vitro*, 30(1):138–165, dec 2015. ISSN 08872333. doi: 10.1016/j.tiv.2015.05.016. URL https://linkinghub.elsevier.com/retrieve/pii/S0887233315001204. (Cited on page 12.)

[23] K. H. Christopher Choy, Jiaqi K. Luo, Cassandra M. J. Wannan, Liliana Laskaris, Antonia Merritt, Warda T. Syeda, Patrick M. Sexton, Arthur Christopoulos, Christos Pantelis, and Jess Nithianantharajah. Cognitive behavioral markers of neurodevelopmental trajectories in rodents. *Translational Psychiatry*, 11(1):556, dec 2021. ISSN 2158-3188. doi: 10.1038/s41398-021-01662-7. URL https://www.nature.com/articles/s41398-021-01662-7. (Cited on page 12.)

[24] Anthony Holtmaat, Tobias Bonhoeffer, David K Chow, Jyoti Chuckowree, Vincenzo De Paola, Sonja B Hofer, Mark Hübener, Tara Keck, Graham Knott, Wei-Chung A Lee, Ricardo Mostany, Tom D Mrsic-Flogel, Elly Nedivi, Carlos Portera-Cailliau, Karel Svoboda, Joshua T Trachtenberg, and Linda Wilbrecht. Long-term, high-resolution imaging in the mouse neocortex through a chronic cranial window. *Nature Protocols*, 4(8):1128–1144, aug 2009. ISSN 1754-2189. doi: 10.1038/nprot.2009.89. URL http://www.nature.com/articles/nprot.2009.89. (Cited on page 12.)

[25] Myunghwan Choi, Sheldon J. J. Kwok, and Seok Hyun Yun. In Vivo Fluorescence Microscopy: Lessons From Observing Cell Behavior in Their Native Environment. *Physiology*, 30(1):40–49, jan 2015. ISSN 1548-9213. doi: 10.1152/physiol.00019.2014. URL https://www.physiology.org/doi/10.1152/physiol.00019.2014. (Cited on page 12.)

[26] Pablo Perel, Ian Roberts, Emily Sena, Philipa Wheble, Catherine Briscoe, Pe-

ter Sandercock, Malcolm Macleod, Luciano E Mignini, Pradeep Jayaram, and Khalid S Khan. Comparison of treatment effects between animal experiments and clinical trials: systematic review. *BMJ*, 334(7586):197, jan 2007. ISSN 0959-8138. doi: 10.1136/bmj.39048.407928.BE. URL https://www.bmj.com/lookup/doi/10.1136/bmj.39048.407928.BE. (Cited on page 12.)

[27] Daniel G. Hackam and Donald A. Redelmeier. Translation of Research Evidence From Animals to Humans. *JAMA*, 296(14):1727, oct 2006. ISSN 0098-7484. doi: 10.1001/jama.296.14.1731. URL http://jama.jamanetwork.com/article.aspx?doi=10.1001/jama.296.14.1731. (Cited on page 12.)

[28] Rasheena Edmondson, Jessica Jenkins Broglie, Audrey F. Adcock, and Liju Yang. Three-Dimensional Cell Culture Systems and Their Applications in Drug Discovery and Cell-Based Biosensors. *ASSAY and Drug Development Technologies*, 12(4):207–218, may 2014. ISSN 1540-658X. doi: 10.1089/adt.2014.573. URL http://www.liebertpub.com/doi/10.1089/adt.2014.573. (Cited on page 13.)

[29] Jennifer H. LaVail and Merrill K. Wolf. Postnatal development of the mouse dentate gyrus in organotypic cultures of the hippocampal formation. *American Journal of Anatomy*, 137(1):47–65, may 1973. ISSN 0002-9106. doi: 10.1002/aja.1001370105. URL https://onlinelibrary.wiley.com/doi/10.1002/aja.1001370105. (Cited on page 13.)

[30] C. Humpel. Organotypic brain slice cultures: A review. *Neuroscience*, 305:86–98, oct 2015. ISSN 03064522. doi: 10.1016/j.neuroscience.2015.07.086. URL https://linkinghub.elsevier.com/retrieve/pii/S0306452215007162. (Cited on page 13.)

[31] Douglas S. Richardson and Jeff W. Lichtman. Clarifying Tissue Clearing. *Cell*, 162(2):246–257, jul 2015. ISSN 00928674. doi: 10.1016/j.

cell.2015.06.067. URL https://linkinghub.elsevier.com/retrieve/pii/S0092867415008375. (Cited on page 14.)

[32] Francesco Pampaloni, Emmanuel G. Reynaud, and Ernst H. K. Stelzer. The third dimension bridges the gap between cell culture and live tissue. *Nature Reviews Molecular Cell Biology*, 8(10):839–845, oct 2007. ISSN 1471-0072. doi: 10.1038/nrm2236. URL http://www.nature.com/articles/nrm2236. (Cited on page 14.)

[33] Sarah E. Cross, Yu-Sheng Jin, Jianyu Rao, and James K. Gimzewski. Nanomechanical analysis of cells from cancer patients. *Nature Nanotechnology*, 2(12): 780–783, dec 2007. ISSN 1748-3387. doi: 10.1038/nnano.2007.388. URL http://www.nature.com/articles/nnano.2007.388. (Cited on page 14.)

[34] Quan-You Zhang, Yan-Yan Zhang, Jing Xie, Chen-Xu Li, Wei-Yi Chen, Bai-Lin Liu, Xiao-an Wu, Shu-Na Li, Bo Huo, Lin-Hua Jiang, and Hu-Cheng Zhao. Stiff substrates enhance cultured neuronal network activity. *Scientific Reports*, 4(1):6215, may 2015. ISSN 2045-2322. doi: 10.1038/srep06215. URL http://www.nature.com/articles/srep06215. (Cited on pages 14 and 46.)

[35] Chao Zhang, Yan Tan, Jiantao Feng, Chang Huang, Biyuan Liu, Zhu Fan, Bing Xu, and Tao Lu. Exploration of the Effects of Substrate Stiffness on Biological Responses of Neural Cells and Their Mechanisms. *ACS Omega*, 5 (48):31115–31125, dec 2020. ISSN 2470-1343. doi: 10.1021/acsomega.0c04279. URL https://pubs.acs.org/doi/10.1021/acsomega.0c04279. (Cited on pages 14 and 46.)

[36] Alexander Dityatev, Melitta Schachner, and Peter Sonderegger. The dual role of the extracellular matrix in synaptic plasticity and homeostasis. *Nature Reviews Neuroscience*, 11(11):735–746, nov 2010. ISSN 1471-003X. doi: 10.1038/nrn2898. URL http://www.nature.com/articles/nrn2898. (Cited on page 15.)

[37] Rossana Rauti, Noa Renous, and Ben M. Maoz. Mimicking the Brain Extracellular Matrix in Vitro : A Review of Current Methodologies and Challenges. *Israel Journal of Chemistry*, 60(12):1141–1151, dec 2020. ISSN 0021-2148. doi: 10.1002/ijch.201900052. URL https://onlinelibrary.wiley.com/doi/10.1002/ijch.201900052. (Cited on page 15.)

[38] KLAUS VON DER MARK, VERENA GAUSS, HELGA VON DER MARK, and PETER MÜLLER. Relationship between cell shape and type of collagen synthesised as chondrocytes lose their cartilage phenotype in culture. *Nature*, 267(5611):531–532, jun 1977. ISSN 0028-0836. doi: 10.1038/267531a0. URL http://www.nature.com/articles/267531a0. (Cited on page 15.)

[39] O. W. Petersen, L. Ronnov-Jessen, A. R. Howlett, and M. J. Bissell. Interaction with basement membrane serves to rapidly distinguish growth and differentiation pattern of normal and malignant human breast epithelial cells. *Proceedings of the National Academy of Sciences*, 89(19):9064–9068, oct 1992. ISSN 0027-8424. doi: 10.1073/pnas.89.19.9064. URL http://www.pnas.org/cgi/doi/10.1073/pnas.89.19.9064. (Cited on page 15.)

[40] Anna C. Luca, Sabrina Mersch, René Deenen, Stephan Schmidt, Isabelle Messner, Karl-Ludwig Schäfer, Stephan E. Baldus, Wolfgang Huckenbeck, Roland P. Piekorz, Wolfram T. Knoefel, Andreas Krieg, and Nikolas H. Stoecklein. Impact of the 3D Microenvironment on Phenotype, Gene Expression, and EGFR Inhibition of Colorectal Cancer Cell Lines. *PLoS ONE*, 8(3): e59689, mar 2013. ISSN 1932-6203. doi: 10.1371/journal.pone.0059689. URL https://dx.plos.org/10.1371/journal.pone.0059689. (Cited on page 15.)

[41] Susanne Sebens and Heiner Schafer. The Tumor Stroma as Mediator of Drug Resistance - A Potential Target to Improve Cancer Therapy? *Current Pharmaceutical Biotechnology*, 13(11):2259–2272, aug 2012. ISSN 13892010. doi: 10.2174/138920112802501999.

URL http://www.eurekaselect.com/openurl/content.php?genre=article{&}issn=1389-2010{&}volume=13{&}issue=11{&}spage=2259. (Cited on page 15.)

[42] Caroline Bonnans, Jonathan Chou, and Zena Werb. Remodelling the extracellular matrix in development and disease. *Nature Reviews Molecular Cell Biology*, 15(12):786–801, dec 2014. ISSN 1471-0072. doi: 10.1038/nrm3904. URL http://www.nature.com/articles/nrm3904. (Cited on page 15.)

[43] C. S. Chen. Geometric Control of Cell Life and Death. *Science*, 276 (5317):1425–1428, may 1997. ISSN 00368075. doi: 10.1126/science.276.5317.1425. URL https://www.sciencemag.org/lookup/doi/10.1126/science.276.5317.1425. (Cited on page 15.)

[44] Helena T Hogberg, Joseph Bressler, Kimberly M Christian, Georgina Harris, Georgia Makri, Cliona O'Driscoll, David Pamies, Lena Smirnova, Zhexing Wen, and Thomas Hartung. Toward a 3D model of human brain development for studying gene/environment interactions. *Stem Cell Research & Therapy*, 4(S1):S4, dec 2013. ISSN 1757-6512. doi: 10.1186/scrt365. URL https://stemcellres.biomedcentral.com/articles/10.1186/scrt365. (Cited on page 15.)

[45] Dana M. Cairns, Nicolas Rouleau, Rachael N. Parker, Katherine G. Walsh, Lee Gehrke, and David L. Kaplan. A 3D human brain–like tissue model of herpes-induced Alzheimer's disease. *Science Advances*, 6(19), may 2020. ISSN 2375-2548. doi: 10.1126/sciadv.aay8828. URL https://www.science.org/doi/10.1126/sciadv.aay8828. (Cited on page 15.)

[46] Gene Modification in Mice. *Nobel Prize Outreach*, 2007. URL https://www.nobelprize.org/prizes/medicine/2007/advanced-information. (Cited on page 17.)

[47] Kazutoshi Takahashi and Shinya Yamanaka. Induction of Pluripotent Stem Cells from Mouse Embryonic and Adult Fibroblast Cultures by Defined Factors. *Cell*, 126(4):663–676, aug 2006. ISSN 00928674. doi: 10.1016/j.cell.2006.07.024. URL https://linkinghub.elsevier.com/retrieve/pii/S0092867406009767. (Cited on page 17.)

[48] Huck-Hui Ng and M. Azim Surani. The transcriptional and signalling networks of pluripotency. *Nature Cell Biology*, 13(5):490–496, may 2011. ISSN 1465-7392. doi: 10.1038/ncb0511-490. URL http://www.nature.com/articles/ncb0511-490. (Cited on page 17.)

[49] Hitoshi Niwa. The principles that govern transcription factor network functions in stem cells. *Development*, 145(6), mar 2018. ISSN 1477-9129. doi: 10.1242/dev.157420. URL https://journals.biologists.com/dev/article/145/6/dev157420/48880/The-principles-that-govern-transcription-factor. (Cited on page 17.)

[50] Keisuke Okita, Tomoko Ichisaka, and Shinya Yamanaka. Generation of germline-competent induced pluripotent stem cells. *Nature*, 448(7151):313–317, jul 2007. ISSN 0028-0836. doi: 10.1038/nature05934. URL http://www.nature.com/articles/nature05934. (Cited on page 17.)

[51] Sushrut Dakhore, Bhavana Nayer, and Kouichi Hasegawa. Human Pluripotent Stem Cell Culture: Current Status, Challenges, and Advancement. *Stem Cells International*, 2018:1–17, nov 2018. ISSN 1687-966X. doi: 10.1155/2018/7396905. URL https://www.hindawi.com/journals/sci/2018/7396905/. (Cited on page 17.)

[52] Ranjeet Singh Mahla. Stem Cells Applications in Regenerative Medicine and Disease Therapeutics. *International Journal of Cell Biology*, 2016:1–24, 2016. ISSN 1687-8876. doi: 10.1155/2016/6940283. URL http://www.hindawi.com/journals/ijcb/2016/6940283/. (Cited on page 17.)

[53] Sharif Moradi, Hamid Mahdizadeh, Tomo Šarić, Johnny Kim, Javad Harati, Hosein Shahsavarani, Boris Greber, and Joseph B. Moore. Research and therapy with induced pluripotent stem cells (iPSCs): social, legal, and ethical considerations. *Stem Cell Research & Therapy*, 10(1):341, dec 2019. ISSN 1757-6512. doi: 10.1186/s13287-019-1455-y. URL https://stemcellres.biomedcentral.com/articles/10.1186/s13287-019-1455-y. (Cited on page 17.)

[54] Atena Farkhondeh, Rong Li, Kirill Gorshkov, Kevin G. Chen, Matthew Might, Steven Rodems, Donald C. Lo, and Wei Zheng. Induced pluripotent stem cells for neural drug discovery. *Drug Discovery Today*, 24(4):992–999, apr 2019. ISSN 13596446. doi: 10.1016/j.drudis.2019.01.007. URL https://linkinghub.elsevier.com/retrieve/pii/S1359644618301405. (Cited on page 17.)

[55] Laura Pellegrini, Claudia Bonfio, Jessica Chadwick, Farida Begum, Mark Skehel, and Madeline A. Lancaster. Human CNS barrier-forming organoids with cerebrospinal fluid production. *Science*, 369(6500), jul 2020. ISSN 0036-8075. doi: 10.1126/science.aaz5626. URL https://www.science.org/doi/10.1126/science.aaz5626. (Cited on pages 18 and 21.)

[56] Keiko Muguruma, Ayaka Nishiyama, Hideshi Kawakami, Kouichi Hashimoto, and Yoshiki Sasai. Self-Organization of Polarized Cerebellar Tissue in 3D Culture of Human Pluripotent Stem Cells. *Cell Reports*, 10(4):537–550, feb 2015. ISSN 22111247. doi: 10.1016/j.celrep.2014.12.051. URL https://linkinghub.elsevier.com/retrieve/pii/S2211124714011048. (Cited on pages 18 and 21.)

[57] Mototsugu Eiraku, Nozomu Takata, Hiroki Ishibashi, Masako Kawada, Eriko Sakakura, Satoru Okuda, Kiyotoshi Sekiguchi, Taiji Adachi, and Yoshiki Sasai. Self-organizing optic-cup morphogenesis in three-dimensional culture. *Na-*

ture, 472(7341):51–56, apr 2011. ISSN 0028-0836. doi: 10.1038/nature09941. URL http://www.nature.com/articles/nature09941. (Cited on pages 18 and 21.)

[58] Midori Kato-Negishi, Yuya Morimoto, Hiroaki Onoe, and Shoji Takeuchi. Millimeter-Sized Neural Building Blocks for 3D Heterogeneous Neural Network Assembly. *Advanced Healthcare Materials*, 2(12):1564–1570, dec 2013. ISSN 21922640. doi: 10.1002/adhm.201300052. URL https://onlinelibrary.wiley.com/doi/10.1002/adhm.201300052. (Cited on pages 18, 22, 24 and 35.)

[59] G. M. Whitesides. Self-Assembly at All Scales. *Science*, 295(5564):2418–2421, mar 2002. ISSN 00368075. doi: 10.1126/science.1070821. URL https://www.sciencemag.org/lookup/doi/10.1126/science.1070821. (Cited on page 18.)

[60] Meenal Banerjee and Ramesh R. Bhonde. Application of hanging drop technique for stem cell differentiation and cytotoxicity studies. *Cytotechnology*, 51(1):1–5, may 2006. ISSN 0920-9069. doi: 10.1007/s10616-006-9001-z. URL http://link.springer.com/10.1007/s10616-006-9001-z. (Cited on page 18.)

[61] Sigrid A. Langhans. Three-Dimensional in Vitro Cell Culture Models in Drug Discovery and Drug Repositioning. *Frontiers in Pharmacology*, 9, jan 2018. ISSN 1663-9812. doi: 10.3389/fphar.2018.00006. URL http://journal.frontiersin.org/article/10.3389/fphar.2018.00006/full. (Cited on page 20.)

[62] D. Huh, B. D. Matthews, A. Mammoto, M. Montoya-Zavala, H. Y. Hsin, and D. E. Ingber. Reconstituting Organ-Level Lung Functions on a Chip. *Science*, 328(5986):1662–1668, jun 2010. ISSN 0036-8075. doi: 10.1126/

science.1188302. URL https://www.sciencemag.org/lookup/doi/10.1126/science.1188302. (Cited on page 20.)

[63] Fang Yu, Walter Hunziker, and Deepak Choudhury. Engineering microfluidic organoid-on-a-chip platforms. *Micromachines*, 10(3):1–12, 2019. ISSN 2072666X. doi: 10.3390/mi10030165. (Cited on page 20.)

[64] Eliah R. Shamir and Andrew J. Ewald. Three-dimensional organotypic culture: experimental models of mammalian biology and disease. *Nature Reviews Molecular Cell Biology*, 15(10):647–664, oct 2014. ISSN 1471-0072. doi: 10.1038/nrm3873. URL http://www.nature.com/articles/nrm3873. (Cited on page 20.)

[65] Hans Clevers. Modeling Development and Disease with Organoids. *Cell*, 165(7):1586–1597, jun 2016. ISSN 00928674. doi: 10.1016/j.cell.2016.05.082. URL https://linkinghub.elsevier.com/retrieve/pii/S0092867416307292. (Cited on pages 20 and 21.)

[66] Amy M. Hopkins, Elise DeSimone, Karolina Chwalek, and David L. Kaplan. 3D in vitro modeling of the central nervous system. *Progress in Neurobiology*, 125:1–25, feb 2015. ISSN 03010082. doi: 10.1016/j.pneurobio.2014.11.003. URL https://linkinghub.elsevier.com/retrieve/pii/S0301008214001233. (Cited on page 21.)

[67] Aliya Fatehullah, Si Hui Tan, and Nick Barker. Organoids as an in vitro model of human development and disease. *Nature Cell Biology*, 18(3):246–254, mar 2016. ISSN 1465-7392. doi: 10.1038/ncb3312. URL http://www.nature.com/articles/ncb3312. (Cited on page 21.)

[68] Chun-Ting Lee, Raphael M. Bendriem, Wells W. Wu, and Rong-Fong Shen. 3D brain Organoids derived from pluripotent stem cells: promising experimental models for brain development and neurodegenerative disorders.

Journal of Biomedical Science, 24(1):59, dec 2017. ISSN 1423-0127. doi: 10.1186/s12929-017-0362-8. URL http://jbiomedsci.biomedcentral.com/articles/10.1186/s12929-017-0362-8. (Cited on page 21.)

[69] Donald E. Ingber. Reverse Engineering Human Pathophysiology with Organs-on-Chips. *Cell*, 164(6):1105–1109, mar 2016. ISSN 00928674. doi: 10.1016/j.cell.2016.02.049. URL https://linkinghub.elsevier.com/retrieve/pii/S0092867416301994. (Cited on page 21.)

[70] Polyxeni Nikolakopoulou, Rossana Rauti, Dimitrios Voulgaris, Iftach Shlomy, Ben M Maoz, and Anna Herland. Recent progress in translational engineered in vitro models of the central nervous system. *Brain*, 143(11): 3181–3213, nov 2020. ISSN 0006-8950. doi: 10.1093/brain/awaa268. URL https://academic.oup.com/brain/article/143/11/3181/5918191. (Cited on page 21.)

[71] Anna P. Miller, Alok S. Shah, Brandy V. Aperi, Matthew D. Budde, Frank A. Pintar, Sergey Tarima, Shekar N. Kurpad, Brian D. Stemper, and Aleksandra Glavaski-Joksimovic. Effects of Blast Overpressure on Neurons and Glial Cells in Rat Organotypic Hippocampal Slice Cultures. *Frontiers in Neurology*, 6, feb 2015. ISSN 1664-2295. doi: 10.3389/fneur.2015.00020. URL http://journal.frontiersin.org/Article/10.3389/fneur.2015.00020/abstract. (Cited on page 22.)

[72] Rea Ravin, Paul S. Blank, Brad Busse, Nitay Ravin, Shaleen Vira, Ludmila Bezrukov, Hang Waters, Hugo Guerrero-Cazares, Alfredo Quinones-Hinojosa, Philip R. Lee, R. Douglas Fields, Sergey M. Bezrukov, and Joshua Zimmerberg. Blast shockwaves propagate Ca2+ activity via purinergic astrocyte networks in human central nervous system cells. *Scientific Reports*, 6(1):25713, sep 2016. ISSN 2045-2322. doi: 10.1038/srep25713. URL http://www.nature.com/articles/srep25713. (Cited on page 22.)

[73] Aoi Odawara, Masao Gotoh, and Ikuro Suzuki. A three-dimensional neuronal culture technique that controls the direction of neurite elongation and the position of soma to mimic the layered structure of the brain. *RSC Advances*, 3(45):23620, 2013. ISSN 2046-2069. doi: 10.1039/c3ra44757j. URL http://xlink.rsc.org/?DOI=c3ra44757j. (Cited on page 22.)

[74] Pei Zhuang, Alfred Xuyang Sun, Jia An, Chee Kai Chua, and Sing Yian Chew. 3D neural tissue models: From spheroids to bioprinting. *Biomaterials*, 154:113–133, feb 2018. ISSN 01429612. doi: 10.1016/j.biomaterials.2017.10.002. URL https://linkinghub.elsevier.com/retrieve/pii/S0142961217306361. (Cited on page 23.)

[75] Midori Kato-Negishi, Yukiko Tsuda, Hiroaki Onoe, and Shoji Takeuchi. A neurospheroid network-stamping method for neural transplantation to the brain. *Biomaterials*, 31(34):8939–8945, dec 2010. ISSN 01429612. doi: 10.1016/j.biomaterials.2010.08.008. URL https://linkinghub.elsevier.com/retrieve/pii/S0142961210010148. (Cited on pages 24 and 35.)

[76] Gi Seok Jeong, Joon Young Chang, Ji Soo Park, Seung A. Lee, Doyeun Park, Junsung Woo, Heeyoung An, C. Justin Lee, and Sang Hoon Lee. Networked neural spheroid by neuro-bundle mimicking nervous system created by topology effect. *Molecular Brain*, 8, 2015. ISSN 17566606. doi: 10.1186/s13041-015-0109-y. (Cited on pages 24 and 35.)

[77] A. Khademhosseini, R. Langer, J. Borenstein, and J. P. Vacanti. Microscale technologies for tissue engineering and biology. *Proceedings of the National Academy of Sciences*, 103(8):2480–2487, feb 2006. ISSN 0027-8424. doi: 10.1073/pnas.0507681102. URL http://www.pnas.org/cgi/doi/10.1073/pnas.0507681102. (Cited on page 24.)

[78] Stefan A. Kobel and Matthias P. Lutolf. Fabrication of PEG Hydrogel Microwell Arrays for High-Throughput Single Stem Cell Culture and Anal-

ysis. pages 101–112. 2012. doi: 10.1007/978-1-61779-388-2_7. URL http://link.springer.com/10.1007/978-1-61779-388-2{_}7. (Cited on pages 24 and 26.)

[79] Daniel E. Heath, Abdul Rahim Mohamed Sharif, Chee Ping Ng, Mary G. Rhoads, Linda G. Griffith, Paula T. Hammond, and Mary B. Chan-Park. Regenerating the cell resistance of micromolded PEG hydrogels. *Lab on a Chip*, 15(9):2073–2089, 2015. ISSN 1473-0197. doi: 10.1039/C4LC01416B. URL http://xlink.rsc.org/?DOI=C4LC01416B. (Cited on page 24.)

[80] H. Kim, R. E. Cohen, P. T. Hammond, and D. J. Irvine. Live Lymphocyte Arrays for Biosensing. *Advanced Functional Materials*, 16(10):1313–1323, jul 2006. ISSN 1616-301X. doi: 10.1002/adfm.200500888. URL https://onlinelibrary.wiley.com/doi/10.1002/adfm.200500888. (Cited on page 24.)

[81] Hannes-Christian Moeller, Matthew K. Mian, Shamit Shrivastava, Bong Geun Chung, and Ali Khademhosseini. A microwell array system for stem cell culture. *Biomaterials*, 29(6):752–763, feb 2008. ISSN 01429612. doi: 10.1016/j.biomaterials.2007.10.030. URL https://linkinghub.elsevier.com/retrieve/pii/S0142961207008320. (Cited on page 24.)

[82] Pilnam Kim, Hoon Eui Jeong, Ali Khademhosseini, and Kahp Y. Suh. Fabrication of non-biofouling polyethylene glycol micro- and nanochannels by ultraviolet-assisted irreversible sealing. *Lab on a Chip*, 6(11):1432, 2006. ISSN 1473-0197. doi: 10.1039/b610503c. URL http://xlink.rsc.org/?DOI=b610503c. (Cited on page 24.)

[83] Kahp Y. Suh, Jiehyun Seong, Ali Khademhosseini, Paul E. Laibinis, and Robert Langer. A simple soft lithographic route to fabrication of poly(ethylene glycol) microstructures for protein and cell patterning. *Biomaterials*, 25(3):557–563, feb 2004. ISSN 01429612. doi: 10.

1016/S0142-9612(03)00543-X. URL https://linkinghub.elsevier.com/retrieve/pii/S014296120300543X. (Cited on page 24.)

[84] Ping Zhang, Yan Xiao, Zhe Li, Jinsong Guo, and Lunhui Lu. Microalgae in Microwell Arrays Exhibit Differences with Those in Flasks: Evidence from Growth Rate, Cellular Carotenoid, and Oxygen Production. *Frontiers in Plant Science*, 8, jan 2018. ISSN 1664-462X. doi: 10.3389/fpls.2017.02251. URL http://journal.frontiersin.org/article/10.3389/fpls.2017.02251/full. (Cited on page 24.)

[85] Gi Seok Jeong, Ji Hoon Song, Ah Ran Kang, Yesl Jun, Jeong Hun Kim, Joon Young Chang, and Sang-Hoon Lee. Surface Tension-Mediated, Concave-Microwell Arrays for Large-Scale, Simultaneous Production of Homogeneously Sized Embryoid Bodies. *Advanced Healthcare Materials*, 2(1): 119–125, jan 2013. ISSN 21922640. doi: 10.1002/adhm.201200070. URL https://onlinelibrary.wiley.com/doi/10.1002/adhm.201200070. (Cited on page 24.)

[86] Myriam Cordey, Monika Limacher, Stefan Kobel, Verdon Taylor, and Matthias P. Lutolf. Enhancing the Reliability and Throughput of Neurosphere Culture on Hydrogel Microwell Arrays. *STEM CELLS*, 26(10):2586–2594, oct 2008. ISSN 10665099. doi: 10.1634/stemcells.2008-0498. URL http://doi.wiley.com/10.1634/stemcells.2008-0498. (Cited on page 24.)

[87] Nikolaos A Peppas, Kelley B Keys, Madeline Torres-Lugo, and Anthony M Lowman. Poly(ethylene glycol)-containing hydrogels in drug delivery. *Journal of Controlled Release*, 62(1-2):81–87, nov 1999. ISSN 01683659. doi: 10.1016/S0168-3659(99)00027-9. URL https://linkinghub.elsevier.com/retrieve/pii/S0168365999000279. (Cited on page 25.)

[88] Allan S. Hoffman, Daniel Cohn, Stephen R. Hanson, Laurence A. Harker, Thomas A. Horbett, Buddy D. Ratner, and Larry O. Reynolds. Application

of radiation-grafted hydrogels as blood-contacting biomaterials. *Radiation Physics and Chemistry (1977)*, 22(1-2):267–283, jan 1983. ISSN 01465724. doi: 10.1016/0146-5724(83)90211-X. URL https://linkinghub.elsevier.com/retrieve/pii/014657248390211X. (Cited on page 25.)

[89] Steven R Caliari and Jason A Burdick. A practical guide to hydrogels for cell culture. *Nature methods*, 13(5):405–14, 2016. ISSN 1548-7105. doi: 10.1038/nmeth.3839. URL http://www.ncbi.nlm.nih.gov/pubmed/27123816http://www.pubmedcentral.nih.gov/articlerender.fcgi?artid=PMC5800304. (Cited on pages 27 and 29.)

[90] Weikang Hu, Zijian Wang, Yu Xiao, Shengmin Zhang, and Jianglin Wang. Advances in crosslinking strategies of biomedical hydrogels. *Biomaterials Science*, 7(3):843–855, 2019. ISSN 2047-4830. doi: 10.1039/C8BM01246F. URL http://xlink.rsc.org/?DOI=C8BM01246F. (Cited on page 27.)

[91] Korsmeyer RW Nicholas A. Peppas. *Dynamically swelling hydro-gels in controlled release applications.* 1987. (Cited on page 27.)

[92] Nasim Annabi, Ali Tamayol, Jorge Alfredo Uquillas, Mohsen Akbari, Luiz E. Bertassoni, Chaenyung Cha, Gulden Camci-Unal, Mehmet R. Dokmeci, Nicholas A. Peppas, and Ali Khademhosseini. 25th Anniversary Article: Rational Design and Applications of Hydrogels in Regenerative Medicine. *Advanced Materials*, 26(1):85–124, jan 2014. ISSN 09359648. doi: 10.1002/adma.201303233. URL https://onlinelibrary.wiley.com/doi/10.1002/adma.201303233. (Cited on pages 27, 30 and 31.)

[93] Jane Ru Choi, Kar Wey Yong, Jean Yu Choi, and Alistair C Cowie. Recent advances in photo-crosslinkable hydrogels for biomedical applications. *BioTechniques*, 66(1):40–53, jan 2019. ISSN 0736-6205. doi: 10.2144/btn-2018-0083. URL https://www.future-science.com/doi/10.2144/btn-2018-0083. (Cited on pages 27, 31 and 32.)

[94] Kanika Vats, Graham Marsh, Kristen Harding, Ioannis Zampetakis, Richard E. Waugh, and Danielle S. W. Benoit. Nanoscale physicochemical properties of chain- and step-growth polymerized PEG hydrogels affect cell-material interactions. *Journal of Biomedical Materials Research Part A*, 105 (4):1112–1122, apr 2017. ISSN 1549-3296. doi: 10.1002/jbm.a.36007. URL https://onlinelibrary.wiley.com/doi/10.1002/jbm.a.36007. (Cited on pages 28 and 31.)

[95] N. A. Peppas, J. Z. Hilt, A. Khademhosseini, and R. Langer. Hydrogels in Biology and Medicine: From Molecular Principles to Bionanotechnology. *Advanced Materials*, 18(11):1345–1360, jun 2006. ISSN 0935-9648. doi: 10.1002/adma.200501612. URL https://onlinelibrary.wiley.com/doi/10.1002/adma.200501612. (Cited on page 28.)

[96] N Peppas. Hydrogels in pharmaceutical formulations. *European Journal of Pharmaceutics and Biopharmaceutics*, 50(1):27–46, jul 2000. ISSN 09396411. doi: 10.1016/S0939-6411(00)00090-4. URL https://linkinghub.elsevier.com/retrieve/pii/S0939641100000904. (Cited on page 28.)

[97] J. Milton Harris. Introduction to Biotechnical and Biomedical Applications of Poly(Ethylene Glycol). In *Poly(Ethylene Glycol) Chemistry*, pages 1–14. Springer US, Boston, MA, 1992. doi: 10.1007/978-1-4899-0703-5_1. URL http://link.springer.com/10.1007/978-1-4899-0703-5{_}1. (Cited on page 28.)

[98] Qinyuan Chai, Yang Jiao, and Xinjun Yu. Hydrogels for Biomedical Applications: Their Characteristics and the Mechanisms behind Them. *Gels*, 3(1):6, jan 2017. ISSN 2310-2861. doi: 10.3390/gels3010006. URL http://www.mdpi.com/2310-2861/3/1/6. (Cited on page 29.)

[99] Amy H. Van Hove, Brandon D. Wilson, and Danielle S. W. Benoit. Microwave-assisted Functionalization of Poly(ethylene glycol) and On-

resin Peptides for Use in Chain Polymerizations and Hydrogel Formation. *Journal of Visualized Experiments*, (80), oct 2013. ISSN 1940-087X. doi: 10.3791/50890. URL http://www.jove.com/video/50890/microwave-assisted-functionalization-poly-ethylene-glycol-on-resin. (Cited on pages 29 and 30.)

[100] Chien-Chi Lin, Chang Seok Ki, and Han Shih. Thiol-norbornene photoclick hydrogels for tissue engineering applications. *Journal of Applied Polymer Science*, 132(8):n/a–n/a, feb 2015. ISSN 00218995. doi: 10.1002/app.41563. URL https://onlinelibrary.wiley.com/doi/10.1002/app.41563. (Cited on page 29.)

[101] Mark W. Tibbitt, April M. Kloxin, Lisa A. Sawicki, and Kristi S. Anseth. Mechanical Properties and Degradation of Chain and Step-Polymerized Photodegradable Hydrogels. *Macromolecules*, 46(7):2785–2792, apr 2013. ISSN 0024-9297. doi: 10.1021/ma302522x. URL https://pubs.acs.org/doi/10.1021/ma302522x. (Cited on page 31.)

[102] Yasuyuki Sanai, Shinobu Kagami, and Kouzou Kubota. Cross-linking photopolymerization of monoacrylate initiated by benzophenone. *Journal of Polymer Science Part A: Polymer Chemistry*, 56(14):1545–1553, jul 2018. ISSN 0887624X. doi: 10.1002/pola.29038. URL https://onlinelibrary.wiley.com/doi/10.1002/pola.29038. (Cited on page 31.)

[103] Rúben F. Pereira and Paulo J. Bártolo. 3D Photo-Fabrication for Tissue Engineering and Drug Delivery. *Engineering*, 1(1):090–112, mar 2015. ISSN 20958099. doi: 10.15302/J-ENG-2015015. URL https://linkinghub.elsevier.com/retrieve/pii/S2095809916300509. (Cited on pages 31, 32 and 34.)

[104] Yanjiao Jiang, Jing Chen, Chao Deng, Erik J. Suuronen, and Zhiyuan Zhong. Click hydrogels, microgels and nanogels: Emerging platforms for

drug delivery and tissue engineering. *Biomaterials*, 35(18):4969–4985, jun 2014. ISSN 01429612. doi: 10.1016/j.biomaterials.2014.03.001. URL https://linkinghub.elsevier.com/retrieve/pii/S014296121400221X. (Cited on page 31.)

[105] Chien-Chi Lin, Asad Raza, and Han Shih. PEG hydrogels formed by thiol-ene photo-click chemistry and their effect on the formation and recovery of insulin-secreting cell spheroids. *Biomaterials*, 32(36):9685–9695, dec 2011. ISSN 01429612. doi: 10.1016/j.biomaterials.2011.08.083. URL https://linkinghub.elsevier.com/retrieve/pii/S0142961211010313. (Cited on page 31.)

[106] Rok Simič and Nicholas D. Spencer. Controlling the Friction of Gels by Regulating Interfacial Oxygen During Polymerization. *Tribology Letters*, 69(3):86, sep 2021. ISSN 1023-8883. doi: 10.1007/s11249-021-01459-1. URL https://link.springer.com/10.1007/s11249-021-01459-1. (Cited on page 33.)

[107] Aurélien Pasturel, Pierre-Olivier Strale, and Vincent Studer. Tailoring Common Hydrogels into 3D Cell Culture Templates. *Advanced Healthcare Materials*, 9(18):2000519, sep 2020. ISSN 2192-2640. doi: 10.1002/adhm.202000519. URL https://onlinelibrary.wiley.com/doi/10.1002/adhm.202000519. (Cited on pages 33, 35, 42 and 45.)

[108] Han Shih and Chien-Chi Lin. Visible-Light-Mediated Thiol-Ene Hydrogelation Using Eosin-Y as the Only Photoinitiator. *Macromolecular Rapid Communications*, 34(3):269–273, feb 2013. ISSN 10221336. doi: 10.1002/marc.201200605. URL https://onlinelibrary.wiley.com/doi/10.1002/marc.201200605. (Cited on page 34.)

[109] Iris Mironi-Harpaz, Dennis Yingquan Wang, Subbu Venkatraman, and Dror Seliktar. Photopolymerization of cell-encapsulating hydrogels: Crosslinking efficiency versus cytotoxicity. *Acta Biomaterialia*, 8(5):1838–1848, may

2012. ISSN 17427061. doi: 10.1016/j.actbio.2011.12.034. URL https://linkinghub.elsevier.com/retrieve/pii/S1742706112000050. (Cited on page 34.)

[110] A N Yaroslavsky, P C Schulze, I V Yaroslavsky, R Schober, F Ulrich, and H-J Schwarzmaier. Optical properties of selected native and coagulated human brain tissues in vitro in the visible and near infrared spectral range. *Physics in Medicine and Biology*, 47(12):305, jun 2002. ISSN 00319155. doi: 10.1088/0031-9155/47/12/305. URL https://iopscience.iop.org/article/10.1088/0031-9155/47/12/305. (Cited on page 35.)

[111] Martin Oheim, Emmanuel Beaurepaire, Emmanuelle Chaigneau, Jerome Mertz, and Serge Charpak. Two-photon microscopy in brain tissue: parameters influencing the imaging depth. *Journal of Neuroscience Methods*, 111(1):29–37, oct 2001. ISSN 01650270. doi: 10.1016/S0165-0270(01)00438-1. URL https://linkinghub.elsevier.com/retrieve/pii/S0165027001004381. (Cited on page 35.)

[112] D. Kleinfeld, P. P. Mitra, F. Helmchen, and W. Denk. Fluctuations and stimulus-induced changes in blood flow observed in individual capillaries in layers 2 through 4 of rat neocortex. *Proceedings of the National Academy of Sciences*, 95(26):15741–15746, dec 1998. ISSN 0027-8424. doi: 10.1073/pnas.95.26.15741. URL http://www.pnas.org/cgi/doi/10.1073/pnas.95.26.15741. (Cited on page 35.)

[113] Giuseppe Pani, Nada Samari, Roel Quintens, Louis de Saint-Georges, MariAntonia Meloni, Sarah Baatout, Patrick Van Oostveldt, and Mohammed Abderrafi Benotmane. Morphological and Physiological Changes in Mature In Vitro Neuronal Networks towards Exposure to Short-, Middle- or Long-Term Simulated Microgravity. *PLoS ONE*, 8(9):e73857, sep 2013. ISSN

1932-6203. doi: 10.1371/journal.pone.0073857. URL https://dx.plos.org/10.1371/journal.pone.0073857. (Cited on page 49.)

[114] Marija Markicevic, Iurii Savvateev, Christina Grimm, and Valerio Zerbi. Emerging imaging methods to study whole-brain function in rodent models. *Translational Psychiatry*, 11(1):457, dec 2021. ISSN 2158-3188. doi: 10.1038/s41398-021-01575-5. URL https://www.nature.com/articles/s41398-021-01575-5. (Cited on page 54.)

[115] M Chalfie, Y Tu, G Euskirchen, W. Ward, and D. Prasher. Green fluorescent protein as a marker for gene expression. *Science*, 263(5148):802–805, feb 1994. ISSN 0036-8075. doi: 10.1126/science.8303295. URL https://www.sciencemag.org/lookup/doi/10.1126/science.8303295. (Cited on page 55.)

[116] Karin E. Sorra and Kristen M. Harris. Overview on the structure, composition, function, development, and plasticity of hippocampal dendritic spines. *Hippocampus*, 10(5):501–511, 2000. ISSN 1050-9631. doi: 10.1002/1098-1063(2000)10:5<501::AID-HIPO1>3.0.CO;2-T. URL https://onlinelibrary.wiley.com/doi/10.1002/1098-1063(2000)10:5{%}3C501::AID-HIPO1{%}3E3.0.CO;2-T. (Cited on page 55.)

[117] Shigeo Okabe. Fluorescence imaging of synapse formation and remodeling. *Microscopy*, 62(1):51–62, feb 2013. ISSN 2050-5698. doi: 10.1093/jmicro/dfs083. URL https://academic.oup.com/jmicro/article-lookup/doi/10.1093/jmicro/dfs083. (Cited on page 55.)

[118] Aurélie Jost and Rainer Heintzmann. Superresolution Multidimensional Imaging with Structured Illumination Microscopy. *Annual Review of Materials Research*, 43(1):261–282, jul 2013. ISSN 1531-7331. doi: 10.1146/annurev-matsci-071312-121648. URL https://www.annualreviews.

org/doi/10.1146/annurev-matsci-071312-121648. (Cited on pages 56, 82 and 85.)

[119] Stefan W Hell, Marcus Dyba, and Stefan Jakobs. Concepts for nanoscale resolution in fluorescence microscopy. *Current Opinion in Neurobiology*, 14(5):599–609, oct 2004. ISSN 09594388. doi: 10.1016/j.conb.2004.08.015. URL https://linkinghub.elsevier.com/retrieve/pii/S0959438804001291. (Cited on page 56.)

[120] Crystal G. Pontrello and Iryna M. Ethell. Accelerators, Brakes, and Gears of Actin Dynamics in Dendritic Spines. *The Open Neuroscience Journal*, 3(2):67–86, dec 2009. ISSN 18740820. doi: 10.2174/1874082000903020067. URL http://www.bentham-open.org/pages/content.php?TONEURJ/2009/00000003/00000002/67TONEURJ.SGM. (Cited on page 58.)

[121] Joseph M. Schmitt and Gitesh Kumar. Optical scattering properties of soft tissue: a discrete particle model. *Applied Optics*, 37(13):2788, may 1998. ISSN 0003-6935. doi: 10.1364/AO.37.002788. URL https://www.osapublishing.org/abstract.cfm?URI=ao-37-13-2788. (Cited on page 59.)

[122] Fritjof Helmchen and Winfried Denk. Deep tissue two-photon microscopy. *Nature Methods*, 2(12):932–940, dec 2005. ISSN 1548-7091. doi: 10.1038/nmeth818. URL http://www.nature.com/articles/nmeth818. (Cited on pages 62, 74 and 76.)

[123] T. WILSON. Optical sectioning in fluorescence microscopy. *Journal of Microscopy*, 242(2):111–116, may 2011. ISSN 00222720. doi: 10.1111/j.1365-2818.2010.03457.x. URL https://onlinelibrary.wiley.com/doi/10.1111/j.1365-2818.2010.03457.x. (Cited on pages 63 and 87.)

[124] Maria Göppert-Mayer. Über Elementarakte mit zwei Quantensprüngen. *An-*

nalen der Physik, 401(3):273–294, 1931. ISSN 00033804. doi: 10.1002/andp.19314010303. URL https://onlinelibrary.wiley.com/doi/10.1002/andp.19314010303. (Cited on page 63.)

[125] Winifried Denk, James H. Strickler, and Watt W. Webb. Two-Photon Laser Scanning Fluorescence Microscopy. *Science*, 248(4951):73–76, apr 1990. ISSN 0036-8075. doi: 10.1126/science.2321027. URL https://www.science.org/doi/10.1126/science.2321027. (Cited on page 63.)

[126] Jean Livet, Tamily A. Weissman, Hyuno Kang, Ryan W. Draft, Ju Lu, Robyn A. Bennis, Joshua R. Sanes, and Jeff W. Lichtman. Transgenic strategies for combinatorial expression of fluorescent proteins in the nervous system. *Nature*, 450(7166):56–62, nov 2007. ISSN 0028-0836. doi: 10.1038/nature06293. URL http://www.nature.com/articles/nature06293. (Cited on page 67.)

[127] Tamily A Weissman and Y Albert Pan. Brainbow: New Resources and Emerging Biological Applications for Multicolor Genetic Labeling and Analysis. *Genetics*, 199(2):293–306, feb 2015. ISSN 1943-2631. doi: 10.1534/genetics.114.172510. URL https://academic.oup.com/genetics/article/199/2/293/5935802. (Cited on page 68.)

[128] James B. Pawley, editor. *Handbook Of Biological Confocal Microscopy*. Springer US, Boston, MA, 2006. ISBN 978-0-387-25921-5. doi: 10.1007/978-0-387-45524-2. URL http://link.springer.com/10.1007/978-0-387-45524-2. (Cited on page 73.)

[129] Shu Tao, Hong Chan, and Harry van der Graaf. Secondary Electron Emission Materials for Transmission Dynodes in Novel Photomultipliers: A Review. *Materials*, 9(12):1017, dec 2016. ISSN 1996-1944. doi: 10.3390/ma9121017. URL http://www.mdpi.com/1996-1944/9/12/1017. (Cited on page 73.)

[130] José-Angel Conchello and Jeff W Lichtman. Optical sectioning microscopy. *Nature Methods*, 2(12):920–931, dec 2005. ISSN 1548-7091. doi: 10.1038/nmeth815. URL http://www.nature.com/articles/nmeth815. (Cited on pages 73 and 78.)

[131] Karel Svoboda and Ryohei Yasuda. Principles of Two-Photon Excitation Microscopy and Its Applications to Neuroscience. *Neuron*, 50(6):823–839, jun 2006. ISSN 08966273. doi: 10.1016/j.neuron.2006.05.019. URL http://linkinghub.elsevier.com/retrieve/pii/S0896627306004119. (Cited on page 74.)

[132] Graham C. R. Ellis-Davies. Two-Photon Microscopy for Chemical Neuroscience. *ACS Chemical Neuroscience*, 2(4):185–197, apr 2011. ISSN 1948-7193. doi: 10.1021/cn100111a. URL https://pubs.acs.org/doi/10.1021/cn100111a. (Cited on pages 74 and 75.)

[133] Jaime Grutzendler, Narayanan Kasthuri, and Wen-Biao Gan. Long-term dendritic spine stability in the adult cortex. *Nature*, 420(6917):812–816, dec 2002. ISSN 0028-0836. doi: 10.1038/nature01276. URL http://www.nature.com/articles/nature01276. (Cited on page 75.)

[134] Joshua T. Trachtenberg, Brian E. Chen, Graham W. Knott, Guoping Feng, Joshua R. Sanes, Egbert Welker, and Karel Svoboda. Long-term in vivo imaging of experience-dependent synaptic plasticity in adult cortex. *Nature*, 420(6917):788–794, dec 2002. ISSN 0028-0836. doi: 10.1038/nature01273. URL http://www.nature.com/articles/nature01273. (Cited on page 75.)

[135] Kyle R. Jenks, Katya Tsimring, Jacque Pak Kan Ip, Jose C. Zepeda, and Mriganka Sur. Heterosynaptic Plasticity and the Experience-Dependent Refinement of Developing Neuronal Circuits. *Frontiers in Neural Circuits*, 15, dec 2021. ISSN 1662-5110. doi: 10.3389/fncir.2021.803401. URL https://www.

frontiersin.org/articles/10.3389/fncir.2021.803401/full. (Cited on page 75.)

[136] Eirini Papagiakoumou, Emiliano Ronzitti, and Valentina Emiliani. Scanless two-photon excitation with temporal focusing. *Nature Methods*, 17(6):571–581, jun 2020. ISSN 1548-7091. doi: 10.1038/s41592-020-0795-y. URL http://www.nature.com/articles/s41592-020-0795-y. (Cited on pages 75 and 76.)

[137] Andrew G York, Panagiotis Chandris, Damian Dalle Nogare, Jeffrey Head, Peter Wawrzusin, Robert S Fischer, Ajay Chitnis, and Hari Shroff. Instant super-resolution imaging in live cells and embryos via analog image processing. *Nature Methods*, 10(11):1122–1126, nov 2013. ISSN 1548-7091. doi: 10.1038/nmeth.2687. URL http://www.nature.com/articles/nmeth.2687. (Cited on page 77.)

[138] Michael Weber, Michaela Mickoleit, and Jan Huisken. Light sheet microscopy. pages 193–215. 2014. doi: 10.1016/B978-0-12-420138-5.00011-2. URL https://linkinghub.elsevier.com/retrieve/pii/B9780124201385000112. (Cited on page 78.)

[139] Matthew Jemielita, Michael J. Taormina, April DeLaurier, Charles B. Kimmel, and Raghuveer Parthasarathy. Comparing phototoxicity during the development of a zebrafish craniofacial bone using confocal and light sheet fluorescence microscopy techniques. *Journal of Biophotonics*, 6(11-12):920–928, dec 2013. ISSN 1864063X. doi: 10.1002/jbio.201200144. URL https://onlinelibrary.wiley.com/doi/10.1002/jbio.201200144. (Cited on page 79.)

[140] Jaroslav Icha, Michael Weber, Jennifer C. Waters, and Caren Norden. Phototoxicity in live fluorescence microscopy, and how to avoid it. *BioEssays*, 39(8):1–15, 2017. ISSN 15211878. doi: 10.1002/bies.201700003. (Cited on page 79.)

[141] Gianpiero Lazzari, Daniele Vinciguerra, Anna Balasso, Valerie Nicolas, Nicolas Goudin, Meriem Garfa-Traore, Anita Fehér, Andras Dinnyés, Julien Nicolas, Patrick Couvreur, and Simona Mura. Light sheet fluorescence microscopy versus confocal microscopy: in quest of a suitable tool to assess drug and nanomedicine penetration into multicellular tumor spheroids. *European Journal of Pharmaceutics and Biopharmaceutics*, 142:195–203, sep 2019. ISSN 09396411. doi: 10.1016/j.ejpb.2019.06.019. URL https://linkinghub.elsevier.com/retrieve/pii/S0939641119303017. (Cited on page 79.)

[142] Emmanuel G. Reynaud, Uroš Kržič, Klaus Greger, and Ernst H. K. Stelzer. Light sheet-based fluorescence microscopy: More dimensions, more photons, and less photodamage. *HFSP Journal*, 2(5):266–275, oct 2008. ISSN 1955-2068. doi: 10.2976/1.2974980. URL https://www.tandfonline.com/doi/full/10.2976/1.2974980. (Cited on page 79.)

[143] Louis Leung, Abigail V. Klopper, Stephan W. Grill, William A. Harris, and Caren Norden. Apical migration of nuclei during G2 is a prerequisite for all nuclear motion in zebrafish neuroepithelia. *Development*, 138(22):5003–5013, nov 2011. ISSN 1477-9129. doi: 10.1242/dev.071522. URL https://journals.biologists.com/dev/article/138/22/5003/44775/Apical-migration-of-nuclei-during-G2-is-a. (Cited on page 79.)

[144] Elizabeth M.C. Hillman, Venkatakaushik Voleti, Wenze Li, and Hang Yu. Light-Sheet Microscopy in Neuroscience. *Annual Review of Neuroscience*, 42(1):295–313, jul 2019. ISSN 0147-006X. doi: 10.1146/annurev-neuro-070918-050357. URL https://www.annualreviews.org/doi/10.1146/annurev-neuro-070918-050357. (Cited on page 80.)

[145] Thomas A Planchon, Liang Gao, Daniel E Milkie, Michael W Davidson, James A Galbraith, Catherine G Galbraith, and Eric Betzig. Rapid three-

dimensional isotropic imaging of living cells using Bessel beam plane illumination. *Nature Methods*, 8(5):417–423, may 2011. ISSN 1548-7091. doi: 10.1038/nmeth.1586. URL http://www.nature.com/articles/nmeth.1586. (Cited on page 80.)

[146] Terrence F. Holekamp, Diwakar Turaga, and Timothy E. Holy. Fast Three-Dimensional Fluorescence Imaging of Activity in Neural Populations by Objective-Coupled Planar Illumination Microscopy. *Neuron*, 57(5):661–672, mar 2008. ISSN 08966273. doi: 10.1016/j.neuron.2008.01.011. URL https://linkinghub.elsevier.com/retrieve/pii/S0896627308000445. (Cited on page 80.)

[147] C. Dunsby. Optically sectioned imaging by oblique plane microscopy. *Optics Express*, 16(25):20306, dec 2008. ISSN 1094-4087. doi: 10.1364/OE.16.020306. URL https://www.osapublishing.org/oe/abstract.cfm?uri=oe-16-25-20306. (Cited on page 80.)

[148] Matthew B. Bouchard, Venkatakaushik Voleti, César S. Mendes, Clay Lacefield, Wesley B. Grueber, Richard S. Mann, Randy M. Bruno, and Elizabeth M. C. Hillman. Swept confocally-aligned planar excitation (SCAPE) microscopy for high-speed volumetric imaging of behaving organisms. *Nature Photonics*, 9(2):113–119, feb 2015. ISSN 1749-4885. doi: 10.1038/nphoton.2014.323. URL http://www.nature.com/articles/nphoton.2014.323. (Cited on page 80.)

[149] Hans-Ulrich Dodt, Ulrich Leischner, Anja Schierloh, Nina Jährling, Christoph Peter Mauch, Katrin Deininger, Jan Michael Deussing, Matthias Eder, Walter Zieglgänsberger, and Klaus Becker. Ultramicroscopy: three-dimensional visualization of neuronal networks in the whole mouse brain. *Nature Methods*, 4(4):331–336, apr 2007. ISSN 1548-7091. doi: 10.1038/

nmeth1036. URL http://www.nature.com/articles/nmeth1036. (Cited on page 80.)

[150] Marzena Stefaniuk, Emilio J. Gualda, Monika Pawlowska, Diana Legutko, Paweł Matryba, Paulina Koza, Witold Konopka, Dorota Owczarek, Marcin Wawrzyniak, Pablo Loza-Alvarez, and Leszek Kaczmarek. Light-sheet microscopy imaging of a whole cleared rat brain with Thy1-GFP transgene. *Scientific Reports*, 6(1):28209, sep 2016. ISSN 2045-2322. doi: 10.1038/srep28209. URL http://www.nature.com/articles/srep28209. (Cited on page 80.)

[151] Nicholas B Bèchet, Tekla M Kylkilahti, Bengt Mattsson, Martina Petrasova, Nagesh C Shanbhag, and Iben Lundgaard. Light sheet fluorescence microscopy of optically cleared brains for studying the glymphatic system. *Journal of Cerebral Blood Flow & Metabolism*, 40(10):1975–1986, oct 2020. ISSN 0271-678X. doi: 10.1177/0271678X20924954. URL http://journals.sagepub.com/doi/10.1177/0271678X20924954. (Cited on page 80.)

[152] Hiroki R. Ueda, Hans-Ulrich Dodt, Pavel Osten, Michael N. Economo, Jayaram Chandrashekar, and Philipp J. Keller. Whole-Brain Profiling of Cells and Circuits in Mammals by Tissue Clearing and Light-Sheet Microscopy. *Neuron*, 106(3):369–387, may 2020. ISSN 08966273. doi: 10.1016/j.neuron.2020.03.004. URL https://linkinghub.elsevier.com/retrieve/pii/S0896627320301902. (Cited on page 80.)

[153] Jerome Mertz and Jinhyun Kim. Scanning light-sheet microscopy in the whole mouse brain with HiLo background rejection. *Journal of Biomedical Optics*, 15(1):016027, 2010. ISSN 10833668. doi: 10.1117/1.3324890. URL http://biomedicaloptics.spiedigitallibrary.org/article.aspx?doi=10.1117/1.3324890. (Cited on page 80.)

[154] Zhouzhou Zhang, Xiao Yao, Xinxin Yin, Zhangcan Ding, Tianyi Huang, Yan Huo, Runan Ji, Hanchuan Peng, and Zengcai V. Guo. Multi-Scale Light-

Sheet Fluorescence Microscopy for Fast Whole Brain Imaging. *Frontiers in Neuroanatomy*, 15, sep 2021. ISSN 1662-5129. doi: 10.3389/fnana.2021.732464. URL https://www.frontiersin.org/articles/10.3389/fnana.2021.732464/full. (Cited on page 80.)

[155] Chieh-Han Lu, Wei-Chun Tang, Yen-Ting Liu, Shu-Wei Chang, Frances Camille M. Wu, Chin-Yi Chen, Yun-Chi Tsai, Shun-Min Yang, Chiung-Wen Kuo, Yasushi Okada, Yeu-Kuang Hwu, Peilin Chen, and Bi-Chang Chen. Lightsheet localization microscopy enables fast, large-scale, and three-dimensional super-resolution imaging. *Communications Biology*, 2(1):177, dec 2019. ISSN 2399-3642. doi: 10.1038/s42003-019-0403-9. URL http://www.nature.com/articles/s42003-019-0403-9. (Cited on page 81.)

[156] Felix Wäldchen, Jan Schlegel, Ralph Götz, Michael Luciano, Martin Schnermann, Sören Doose, and Markus Sauer. Whole-cell imaging of plasma membrane receptors by 3D lattice light-sheet dSTORM. *Nature Communications*, 11(1):887, dec 2020. ISSN 2041-1723. doi: 10.1038/s41467-020-14731-0. URL http://www.nature.com/articles/s41467-020-14731-0. (Cited on page 81.)

[157] Elizabeth MC Hillman, Venkatakaushik Voleti, Kripa Patel, Wenze Li, Hang Yu, Citlali Perez-Campos, Sam E Benezra, Randy M Bruno, and Pubudu T Galwaduge. High-speed 3D imaging of cellular activity in the brain using axially-extended beams and light sheets. *Current Opinion in Neurobiology*, 50:190–200, jun 2018. ISSN 09594388. doi: 10.1016/j.conb.2018.03.007. URL https://linkinghub.elsevier.com/retrieve/pii/S0959438817301927. (Cited on page 81.)

[158] Thai V Truong, Willy Supatto, David S Koos, John M Choi, and Scott E Fraser. Deep and fast live imaging with two-photon scanned light-sheet microscopy. *Nature Methods*, 8(9):757–760, sep 2011. ISSN 1548-7091. doi:

10.1038/nmeth.1652. URL http://www.nature.com/articles/nmeth.1652. (Cited on page 81.)

[159] Tonmoy Chakraborty, Meghan K. Driscoll, Elise Jeffery, Malea M. Murphy, Philippe Roudot, Bo-Jui Chang, Saumya Vora, Wen Mai Wong, Cara D. Nielson, Hua Zhang, Vladimir Zhemkov, Chitkale Hiremath, Estanislao Daniel De La Cruz, Yating Yi, Ilya Bezprozvanny, Hu Zhao, Raju Tomer, Rainer Heintzmann, Julian P. Meeks, Denise K. Marciano, Sean J. Morrison, Gaudenz Danuser, Kevin M. Dean, and Reto Fiolka. Light-sheet microscopy of cleared tissues with isotropic, subcellular resolution. *Nature Methods*, 16(11): 1109–1113, nov 2019. ISSN 1548-7091. doi: 10.1038/s41592-019-0615-4. URL http://www.nature.com/articles/s41592-019-0615-4. (Cited on page 81.)

[160] Yan Xiao, Adèle Faucherre, Laura Pola-Morell, John M. Heddleston, Tsung-Li Liu, Teng-Leong Chew, Fuminori Sato, Atsuko Sehara-Fujisawa, Koichi Kawakami, and Hernán López-Schier. High-resolution live imaging reveals axon-glia interactions during peripheral nerve injury and repair in zebrafish. *Disease Models & Mechanisms*, 8 (6):553–564, jun 2015. ISSN 1754-8411. doi: 10.1242/dmm.018184. URL https://journals.biologists.com/dmm/article/8/6/553/3730/High-resolution-live-imaging-reveals-axon-glia. (Cited on page 81.)

[161] Loïc A Royer, William C Lemon, Raghav K Chhetri, Yinan Wan, Michael Coleman, Eugene W Myers, and Philipp J Keller. Adaptive light-sheet microscopy for long-term, high-resolution imaging in living organisms. *Nature Biotechnology*, 34(12):1267–1278, dec 2016. ISSN 1087-0156. doi: 10.1038/nbt.3708. URL http://www.nature.com/articles/nbt.3708. (Cited on page 81.)

[162] Raju Tomer, Khaled Khairy, Fernando Amat, and Philipp J Keller. Quantitative high-speed imaging of entire developing embryos with simultaneous multiview light-sheet microscopy. *Nature Methods*, 9(7):755–763, jul 2012. ISSN 1548-7091. doi: 10.1038/nmeth.2062. URL https://www.nature.com/articles/nmeth.2062. (Cited on page 81.)

[163] Anna Kaufmann, Michaela Mickoleit, Michael Weber, and Jan Huisken. Multilayer mounting enables long-term imaging of zebrafish development in a light sheet microscope. *Development*, 139(17):3242–3247, sep 2012. ISSN 1477-9129. doi: 10.1242/dev.082586. URL https://journals.biologists.com/dev/article/139/17/3242/45291/Multilayer-mounting-enables-long-term-imaging-of. (Cited on page 81.)

[164] Misha B Ahrens, Michael B Orger, Drew N Robson, Jennifer M Li, and Philipp J Keller. Whole-brain functional imaging at cellular resolution using light-sheet microscopy. *Nature Methods*, 10(5):413–420, may 2013. ISSN 1548-7091. doi: 10.1038/nmeth.2434. URL https://www.nature.com/articles/nmeth.2434. (Cited on page 81.)

[165] J. VAN KRUGTEN, K.-K.H. TARIS, and ERWIN J.G. PETERMAN. Imaging adult C. elegans live using light-sheet microscopy. *Journal of Microscopy*, 281(3):214–223, mar 2021. ISSN 0022-2720. doi: 10.1111/jmi.12964. URL https://onlinelibrary.wiley.com/doi/10.1111/jmi.12964. (Cited on page 81.)

[166] Zhengyi Yang, Peter Haslehurst, Suzanne Scott, Nigel Emptage, and Kishan Dholakia. A compact light-sheet microscope for the study of the mammalian central nervous system. *Scientific Reports*, 6(1):26317, may 2016. ISSN 2045-2322. doi: 10.1038/srep26317. URL http://www.nature.com/articles/srep26317. (Cited on page 81.)

[167] Bi-Chang Chen, Wesley R. Legant, Kai Wang, Lin Shao, Daniel E. Milkie, Michael W. Davidson, Chris Janetopoulos, Xufeng S. Wu, John A. Hammer, Zhe Liu, Brian P. English, Yuko Mimori-Kiyosue, Daniel P. Romero, Alex T. Ritter, Jennifer Lippincott-Schwartz, Lillian Fritz-Laylin, R. Dyche Mullins, Diana M. Mitchell, Joshua N. Bembenek, Anne-Cecile Reymann, Ralph Böhme, Stephan W. Grill, Jennifer T. Wang, Geraldine Seydoux, U. Serdar Tulu, Daniel P. Kiehart, and Eric Betzig. Lattice light-sheet microscopy: Imaging molecules to embryos at high spatiotemporal resolution. *Science*, 346(6208), oct 2014. ISSN 0036-8075. doi: 10.1126/science.1257998. URL https://www.science.org/doi/10.1126/science.1257998. (Cited on page 81.)

[168] Ruixuan Gao, Shoh M. Asano, Srigokul Upadhyayula, Igor Pisarev, Daniel E. Milkie, Tsung-Li Liu, Ved Singh, Austin Graves, Grace H. Huynh, Yongxin Zhao, John Bogovic, Jennifer Colonell, Carolyn M. Ott, Christopher Zugates, Susan Tappan, Alfredo Rodriguez, Kishore R. Mosaliganti, Shu-Hsien Sheu, H. Amalia Pasolli, Song Pang, C. Shan Xu, Sean G. Megason, Harald Hess, Jennifer Lippincott-Schwartz, Adam Hantman, Gerald M. Rubin, Tom Kirchhausen, Stephan Saalfeld, Yoshinori Aso, Edward S. Boyden, and Eric Betzig. Cortical column and whole-brain imaging with molecular contrast and nanoscale resolution. *Science*, 363(6424), jan 2019. ISSN 0036-8075. doi: 10.1126/science.aau8302. URL https://www.science.org/doi/10.1126/science.aau8302. (Cited on page 81.)

[169] Anne Stockhausen, Jana Bürgers, Juan Eduardo Rodriguez-Gatica, Jens Schweihoff, Rudolf Merkel, Jens Markus Prigge, Martin Karl Schwarz, and Ulrich Kubitscheck. Hard-wired lattice light-sheet microscopy for imaging of expanded samples. *Optics Express*, 28(10):15587, may 2020. ISSN 1094-4087. doi: 10.1364/OE.393728. URL https://www.osapublishing.org/abstract.cfm?URI=oe-28-10-15587. (Cited on page 81.)

[170] Jana Bürgers, Irina Pavlova, Juan E. Rodriguez-Gatica, Christian Henneberger, Marc Oeller, Jan A. Ruland, Jan P. Siebrasse, Ulrich Kubitscheck, and Martin K. Schwarz. Light-sheet fluorescence expansion microscopy: fast mapping of neural circuits at super resolution. *Neurophotonics*, 6(01):1, feb 2019. ISSN 2329-423X. doi: 10.1117/1.NPh.6.1.015005. URL https://www.spiedigitallibrary.org/journals/neurophotonics/volume-6/issue-01/015005/Light-sheet-fluorescence-expansion-microscopy--fast-mapping-of-neural/10.1117/1.NPh.6.1.015005.full. (Cited on page 81.)

[171] James G. Fujimoto, Daniel L. Farkas, and Barry R. Masters. *Biomedical Optical Imaging*, volume 15. 2010. ISBN 9780195150445. doi: 10.1117/1.3490919. (Cited on page 82.)

[172] Mats G. L. Gustafsson, David A. Agard, and John W. Sedat. <title>Sevenfold improvement of axial resolution in 3D wide-field microscopy using two objective lenses</title>. pages 147–156, mar 1995. doi: 10.1117/12.205334. URL http://proceedings.spiedigitallibrary.org/proceeding.aspx?articleid=991163. (Cited on page 83.)

[173] Colin J.R. Sheppard. Super-resolution in confocal imaging. *Optik - International Journal for Light and Electron Optics*, 80(2): 53–54, 1988. URL https://www.researchgate.net/publication/235994020{_}Super-resolution{_}in{_}confocal{_}imaging. (Cited on page 83.)

[174] Claus B. Müller and Jörg Enderlein. Image scanning microscopy. *Physical Review Letters*, 104(19):1–4, 2010. ISSN 00319007. doi: 10.1103/PhysRevLett.104.198101. (Cited on pages 83 and 105.)

[175] Andrew G. York, Sapun H. Parekh, Damian Dalle Nogare, Robert S. Fischer, Kelsey Temprine, Marina Mione, Ajay B. Chitnis, Christian A. Combs, and

Hari Shroff. Resolution doubling in live, multicellular organisms via multifocal structured illumination microscopy. *Nature Methods*, 9(7):749–754, 2012. ISSN 15487091. doi: 10.1038/nmeth.2025. (Cited on page 83.)

[176] M. A. A. Neil, R. Juškaitis, and T. Wilson. Method of obtaining optical sectioning by using structured light in a conventional microscope. *Optics Letters*, 22(24):1905, dec 1997. ISSN 0146-9592. doi: 10.1364/OL.22.001905. URL https://opg.optica.org/abstract.cfm?URI=ol-22-24-1905. (Cited on page 84.)

[177] Per A. Stokseth. Properties of a Defocused Optical System*. *Journal of the Optical Society of America*, 59(10):1314, oct 1969. ISSN 0030-3941. doi: 10.1364/JOSA.59.001314. URL https://opg.optica.org/abstract.cfm?URI=josa-59-10-1314. (Cited on page 88.)

[178] Yixuan Ming, Md Fayad Hasan, Svetlana Tatic-Lucic, and Yevgeny Berdichevsky. Micro Three-Dimensional Neuronal Cultures Generate Developing Cortex-Like Activity Patterns. *Frontiers in Neuroscience*, 14, oct 2020. ISSN 1662-453X. doi: 10.3389/fnins.2020.563905. URL https://www.frontiersin.org/article/10.3389/fnins.2020.563905/full. (Cited on page 104.)

[179] Stefanie Kaech and Gary Banker. Culturing hippocampal neurons. *Nature Protocols*, 1(5):2406–2415, dec 2006. ISSN 1754-2189. doi: 10.1038/nprot.2006.356. URL http://www.nature.com/articles/nprot.2006.356. (Cited on page 109.)